THE DESIGN, ANALYSIS AND EVALUATION OF A BIOMIMETIC HUMANOID ROBOTIC HEAD

Stephen Barker

Ph.D. 2016

THE DESIGN, ANALYSIS AND EVALUATION OF A BIOMIMETIC HUMANOID ROBOTIC HEAD

by

Stephen Barker

Faculty of Technology, Design & Environment
Department of Computing and Communication Technologies

A thesis submitted in partial fulfilment of the requirements of
Oxford Brookes University for the degree of

Doctor of Philosophy

August 2016

OXFORD
BROOKES
UNIVERSITY

Acknowledgments

Firstly, I have to acknowledge my great debt of gratitude to my Director of Studies, Professor Nigel Crook, and my Supervisors, Professor Khaled Hayatleh and Dr Neil Fellows, without whose kind help, assistance, and continual motivation this thesis would not have been possible. It never ceases to amaze me that my 'pipe dream' turned into a reality, thanks to their kind and unceasing help.

Also worthy of mention are my colleagues, and in particular Philip Hughes and Dr Mohamed Ben-Esmael. Philip's practical skills were extremely helpful in the actual building of the robot. Mohamed provided great moral support. In my darker PhD moments, he was always there with his positive comments and encouragement.

My Managers at Oxford Brookes, Professor Gareth Neighbour and Mr Douglas Higgison have to be acknowledged too, for giving me continual encouragement, and the time to complete my PhD.

Finally, my greatest debt is to my fantastic wife, Helen. She would never admit it, but I'm sure that I've driven her mad at times with my PhD, and she has uncomplainingly suffered the woes of a 'PhD Widow'. She has also always shown great belief in me, even when I didn't have it myself, and has been my constant rock and motivator.

Stephen Barker
Oxford Brookes University, August 2016

Abstract

Where robots interact directly with humans on a 'one-to-one' basis, it is often quite important for them to be emotionally acceptable, hence the growing interesting in humanoid robots. In some applications it is important that these robots do not just resemble a human being in appearance, but also move like a human being too, to make them emotionally acceptable – hence the interest in biomimetic humanoid robotics. The research described in this thesis is concerned with the design, analysis and evaluation of a biomimetic humanoid robotic head. It is biomimetic in terms of physical design - which is based around a simulated cervical spine, and actuation, which is achieved using pneumatic air muscles (PAMS). The primary purpose of the research, however, and the main original contribution, was to create a humanoid robotic head capable of mimicking complex non-purely rotational human head movements. These include a sliding front-to-back, lateral movement, and a sliding, side-to-side lateral movement. A number of different approaches were considered and evaluated, before finalising the design.

As there are no generally accepted metrics in the literature regarding the full range of human head movements, the best benchmarks for comparison are the angular ranges and speeds of humans in terms on pitch (nod), roll (tilt) and yaw (rotate) were used for comparison, and these they were considered desired ranges for the robot. These measured up well in comparison in terms of angular speed and some aspects of range of human necks. Additionally, the lateral movements were measured during the nod, tilt and rotate movements, and established the ability of the robot to perform the complex lateral movements seen in humans, thus proving the benefits of the cervical spine approach.

Finally, the emotional acceptance of the robot movements was evaluated against another (commercially made) robot and a human. This was a blind test, in that the (human) evaluators had no way of knowing whether they were evaluation a human or a robot. The tests demonstrated that on scales of Fake/Natural, Machinelike/Humanlike and Unconcsious/Conscious the robot the robot scored similarly to the human.

List of principal terms and abbreviations

Accelerometer	A sensor that measures acceleration
Actuator	A device that provides movement
ADC	Analog to digital converter
Agonist/antagonist	Muscle pairs that work in opposite to enable active and restorative movements
Analogue signal	An electrical signal that can have any level between two pre-defined voltage limits
Arduino board	A microcontroller development board, based on an ARM processor chip
Band stop filter	An electronic circuit that only allows signals in a pre-defined frequency range to pass through
bar	Unit of air pressure. Defined as 100 kilopascals. Approximately equal to air pressure at sea level
Biomechanics	Mechanical laws relating to the structure and movement of biological organisms
Biomimetic	Resembling biology
Cervical spine	The seven vertebrae that make up the human neck
DAC	Digital to analogue converter
DC	Direct current
Degrees of freedom.	The number of ranges of motion. Sometimes abbreviated to DOF
Digital signal	An electrical signal that has only two voltage levels
DMP	Digital motion processor
Duty cycle	On-off time ratio of a digital signal
EEPROM	Electrically erasable programmable read only memory
FPGA	Field programmable gate array
Gain	The increasing of the amplitude and an electrical signal
Gyroscope	A sensor that measures angular rotation
HRI	Human-robot interaction
Humanoid robots	Robots designed to resemble human beings in some way
Hz	Cycles per second
I2C	A 2 wire serial interface protocol
IDE	Integrated development environment
IR	Infra-red
Lateral translation	Movement without rotation
Low-pass filter	An electronic circuit that attenuates signals above a certain cut-off frequency
MEMS	Micro electromechanical systems
Operational amplifier	An amplifier with (theoretically) infinite open loop gain
PAM	Pneumatic air muscle
Proportional valve	A valve that allows for continuous variations in fluid flow to be made
PWM	Pulse width modulation
Servomotors	Actuators where the rotational position of a shaft is set by the pulse width of the controlling signal
Sonar	Distance measurement based on ultrasonic sound echo time
SRAM	Static random access memory

Transducer	A device that converts one form of energy into another
Voltage amplifier	An electronic circuit that increases the amplitude of signals

List of figures and diagrams

List of tables

Table of Contents

CHAPTER 1
INTRODUCTION

1.1 Introduction to biomimetically designed robotic heads and necks

1.2 Angular ranges and speeds of human heads

1.3 Aims and objectives

1.4 Structure of the thesis

1.1 Introduction to biomimetic humanoid robotic heads

Robots are becoming increasingly pervasive within everyday life. They can be found in our homes, vacuuming our carpets, or as far away as Mars, exploring an environment that is toxic to humans. Rather than being confined to precise, repetitive actions in mass production, or used in situations or environments too unpleasant or dangerous for human involvement, robots do and will continue to appear in many situations where they will be expected to interact directly with people on a 'human' level. Such instances occur in applications such as assisting the elderly and disabled, and assisting co-workers in hazardous environments (Deniz *et al.,* 2002). Additionally, humanoid robots can be used in research areas such as multi-sensory/multi-motor control systems, developmental structure, and social interaction (Miwa *et al.,* 2002).

In the field of human-robot interaction (HRI), head robots are being actively researched because the human head carries all the five senses; touch, vision, hearing, smell, and taste (Brooks *et al.,* 1999). Moreover, all human verbal communication, and an element of non-verbal communication is enabled by the head through the use of head gestures (nodding and shaking), eye movements and facial expressions, all which add information to the verbal exchanges, thus making the head the most important part of the body when communicating (Brooks *et al.,* 1999). One possible way of maximising human-robot interaction is to make them more emotionally acceptable. This can be done by making them more human-like in behaviour and/or appearance. When doing this, care is to be taken if one to avoid Mori's (2012) 'Uncanny Valley' where the resemblance to real humans is close enough to make them 'creepy', yet not close enough to gain emotional acceptance. Mori also adds that the movement of a human-like representation has a stronger impact than the appearance. He also predicted that as robots become more life-like, they become more familiar, or as Dautenhahn (2002) states, instead of 'familiar', we would today use the word 'believable'. It is important, however, not to generalise, as studies by Shibata, Wada, and Tanie (2002; 2003; 2004 respectively) have found that perceptions of believability can vary with subject gender and nationally. Another consideration is what can be considered a concrete notion of believability? Rose *et al.,* (2010) state that in this context, it is the naturalness that is being evaluated; that is, how natural does it appear to those who interact with it. They continue that it may also mean that the subject clearly recognises the action in which the robot is engaged. In the context of this research, it could be (for instance) is a nod of the robot head perceived as a nod?

One approach to measuring this has been to get subjects to interact with a robot, and then survey them afterwards as to how believable they found the interaction (Bates, 1994; Hayes-Roth, 1995; Lester and Stone, 1997). An alternative to this is to use physical body

measurements of the subjects to measure their arousal (Picard and Daily, 2005), such as skin resistance, facial expressions, gestures, and posture

Movies such as 'I Robot' and 'The Terminator' have done much to fashion the popular conception of humanoid robots. However, the reality is something far more primitive. As yet, attempts to produce a humanoid robot (or even just a robotic head) that can mimic human movement ranges and velocities in a humanlike fashion – including human head gestures, and interact with humans as well as the movies would have us believe, have not met with great success. This is important, as the emotional acceptability of robot appearance, and maybe even more importantly, behaviour, is a critical consideration in robot-human interaction (Özgen, 2007), as humans are able to attribute drives and intentions based purely on motion *(*Ishiguro, 2006). Motion has an impact on acceptability too. Ishiguru (*ibid*) showed participants two photo-realistic images of an android. The first image was static, and in the second image the android performed very small movements. When questioned regarding their perceptions of the images, the participants said that the moving image made them less aware of the fact that they were dealing with a machine. This shows that in this case, after appearance, motion is a very important factor in emotional acceptability and believability. Other researchers posit that motion is in fact more important than appearance (Maddock *et al.,* 2005), which poses a problem for robot designers, as appearance is a simpler issue to address than motion. Again, as with believability, when considering emotional acceptance, one must first provide a viable definition. A useful definition has been stated as the willingness within a group of users to interact with a technology for the uses for which it was intended (Dillon, 2001). Ibanez (*et al.,* 2014) has a perhaps more accurate definition, in that they state that believable robots are more likely to evoke a more social response from a human. As can be gathered from the previous paragraphs, emotional acceptance and believability are interdependent. Without believability, that is, that an action by a robot actually invokes a social response in a human, the emotional acceptance, or the willingness to interact with the robot will be severely limited.

1.2 Angular ranges and speeds of human heads

In the literature, the active neck range of motions is determined by the number of degrees through which people can move their heads in various directions (LoPresti *et al*., 2003). There are just three factors considered in the literature when measuring the range of head movements, these are: (1) turning the head left to right (axial rotation), (2) bending the head left and right (lateral bending), and (3) bending the head forward and backward (flexion-extension) (Openshaw and Taylor, 2006). These ranges are shown below in table 1.1, and are the datum ranges and angular velocities for the robot. The literature, however, does not

consider lateral, non-rotational movements. One can only surmise from this that the non-rotational movements were perhaps not considered important in diagnosing medical ailments, or perhaps no definite way of measuring them in humans has yet been developed. For this reason, the main benchmark for this work will be based on the rotational metrics, although the non-rotational movements will be recorded too.

Table 1.1 Average ranges of movement for and adult male (Fitzpatrick, 2010)

Total Pitch Range	107°	<430°/Sec
Total Roll Range	90°	<360°/Sec
Total Yaw Range	140°	<467°/Sec

Neurological studies by Leigh and Zee (2015) show that under normal conditions angular head velocities do not exceed 100°/sec, so this figure will be used as the comparison figure for the angular velocity for the various degrees of freedom for the neck.

1.3 Hypothesis and Research Questions

This research evaluates the following hypothesis:

It is possible to make a biomimetic, cervical spine based machine with pneumatic air muscle actuation that is capable of non-rotational lateral translations.

In order to test the hypothesis, it was necessary to find answers to the following research questions:

1. What angular speeds and ranges of head movements in three dimensions can be achieved with such a design?
2. Does the performance of these result in non-rotational translations?
3. What is the extent of these non-rotational translations?
4. What is the emotional reaction of humans to the movements produced?

1.4 Aims and Objectives

In this research, the aim was to design and build a robotic head with the capability to reproduce realistic human head movements. The pneumatic air muscles (PAMs) are placed in biologically accurate positions on a full size replica skull, closely mimicking those of humans, as does the cervical spine of the robot. Such an arrangement allows the non-rotational, lateral movements that is normally lacking in humanoid robotic heads. To date, this particular way of doing it has only been simulated, and has not been explored in a physical robot, and thus would constitute an original contribution to knowledge in the area of humanoid robotics. This is necessary, as to date no one has developed and evaluated truly

accurate 'hardware' models' of the human head and neck. They have merely speculated on improvements of the original design, based upon software modelling. To achieve this accurate modelling, a simplified representation of a human cervical spine was used as a framework for the robot. This resulted in the closest biological and kinetic robotic representation of a human head to date, and thus, this forms an original contribution to the field of humanoid robotics. The major contribution, however, has come from the demonstrating the hypothesis that it is possible to achieve non-rotational lateral translations with a cervical spine based robotic neck that is actuated by pneumatic air muscles.

The Objectives of the investigation are:

1. Analyse the existing methods for the locomotion of the head, and the control and coordination of the mechanics involved in achieving head movements.
2. Analyse why the current methods do not allow for realistic head gestures to be produced.
3. Produce an original design for a humanoid robotic head that has the capability to reproduce these gestures.
4. Build the robot based on this design, and evaluate the effectiveness of it, in terms of objective measurements (ranges and velocities), and subjective measurements (emotional acceptance).

1.5 Structure of the thesis

This thesis comprises five chapters. Following this chapter, the other chapters comprise:

Chapter 2 is a literature review of all the disciplines involved in the project. It reviews the literature on the whole system design, and the sub-units that make up the complete unit. It also outlines the problems of current methods of defining and reproducing human-like head movements in robots. The challenges involved with each sub-unit will also be outlined, and how these challenges are being currently being met, or in some cases, not met. These challenges include; electronic, mechanical and design issues, that is, the integration of the components. The biomechanics of the human neck will also be explored.

Chapter 3 is the product design specification of the robot, and sets out the desired angular ranges and velocities. It also includes the desired lateral translations. It also shows the approach taken to the design of the robot, a discussion of the final design produced, and its practical implementation.

Chapter 4 explains and justifies the experimental approach taken when evaluating the robot's performance, and presents the results.

Chapter 5 discusses what has been learned from the research and the original contribution to knowledge that this forms. Additionally, opportunities for future work will be discussed.

CHAPTER 2

LITERATURE REVIEW OF PREVIOUS WORK ON BIOMIMEMTIC HEAD AND NECK ROBOTS

2.1 Introduction

This chapter forms a review of the literature on the whole system design, and the sub-units that make up the complete unit. It will also discuss the challenges involved with each sub-unit, and how these challenges are being met. These challenges include; electronic, mechanical and integration issues as these components form the entirety of the robot, which is a purely electro-mechanical device. There were no software or control challenges involved, as the device was actuated by the use of very basic programming commands. The design issues were concerned with maximising the likelihood of the achievement of non-rotational lateral translations, whilst at the same time maintaining a biomimetic design.

2.2 Overall system design

Much work has been done on the development of humanoid robot heads, sometimes with the addition of torsos and arms. The research aims behind these designs differ widely. For instance, MAVERic (Vijakumar *et al.,* 2016) is a fairly simple robotic head with a fixed mannequin-like face, where the neck has multiple degrees of freedom, with eyes that can move. This model has been designed for research purely into oculo-motor operation. Similarly, Vijakumar *et al.* (2001) developed a 30 degrees of freedom humanoid robot to study the system linking oculo-motor control, visual processing and limb control in humans. A significant amount of research, has been done on developing robotic heads and torsos, sometimes mobile, for investigation into robot-human interaction, where a more significant degree of emotional acceptability and believability is desirable. This interaction is an important consideration in, for instance, service robots, which are designed to assist the elderly and disabled as caretakers, and will become increasingly useful as the average age and life expectancy of the population continues to increase (Materic, 2000).

Research into human-robot interaction (HRI) contains a diverse field of disciplines Hill, 2000), such as robotics, cognitive science, artificial intelligence and social science, each presenting its own challenges (Baxter *et al.*, 2016). One particularly fundamental challenge for true HRI to occur is the need to collect human interaction data (Lui *et al.,* 2016) which is one of the drivers of the development of sensor heads. Ullman and Malle (2016) suggest that as well as social acceptability and believability, trust is also an issue, and this can only be gained through repeated successful interactions. They define trust itself is where one (human) agent has a belief that another (robotic) agent will act in a certain way. For the purposes of the research in this thesis, this really equates to repeatability, that is, will the robot act/react in ways which are expected. This itself is related to the hardware and software dependability of the system. One definition of HRI is that it is the interaction of humans and robots through communication (Murphy *et al.,* 2010). For this communication to take place, we need to firstly consider the elements of emotional acceptance and believability

(Ibanez *et al.,* 2004), which must also be dependent on the physical appearance of the robot. Within an HRI dialogue situation, posture and gestures are a very important consideration (Stiefelhagen *et al.,* 2004). Yang (*et al.*., 2007) goes further, and states that gestures can fall into one of two groups; communicative gestures, these are motions the convey an explicit meaning to communicate goals, and non-communicative gestures, these are also called transition gestures, and they connect subconscious goals to communicative gestures. Braezeal (*et al.,* 2004) argue that gestures also make the robot's 'internal state' transparent, that is, they make the robot more understandable and predictable.

An attempt at making the physical appearance emotionally acceptable can be seen in PEARL (Personal Robotic Assistant for the Elderly) (figure 2.1) project (Pollack *et al.,* 2002) which is an attempt to develop a mobile personal service robot for the elderly with chronic disorders, that is, problems with no (current) prospect of a cure, that require some kind of interaction with a helper. These conditions include things such as dementia, arthritis, and symptoms arising from diabetes. Such robotic helpers could, amongst other things, remind patients when it is time to take their medication etc. They could also function as a communications link between the patients and the carers, and can collect and provide data on the patients' progress.

Figure 2.1 PEARL (Pollack *et al.,* 2002).

According to Lutkenbohle (*et al.,* 2010) in order for high levels of interaction/ communication to take place two things are necessary on a robot; powerful active sensing capabilities, and the ability to produce social (facial or body) gestures, as human communication is multimodal (Bischoff and Graefe, 2002). This has led to the development of robotic heads that attempt to have a social expressiveness that can be understood

intuitively by humans (Lutkebohle *et al.,* 2010). Such designs attempt to be non-frightening in appearance, and able to demonstrate their capabilities to the non-technical eye (*ibid*). This non-frightening design approach is evident in models such as Kismet (Breazeal, 2003), iCub (Beira *et al.,* 2006) (figure 2.2) Infanoid (Kozima *et al.,* 2005) and iCat (Van Breemen and Yan, 2005), which is one of the smallest, fastest, and best documented heads. As stated earlier, for robots to truly interact with humans and their environment they will need quite a sophisticated array of sensors. This has initially led to a general diversification in research in this area, with the focus often being either on social heads, or sensor heads, as their requirements partially contradict each other (Lutkebohle *et al.,* 2010) due to non-human appearance of the sensor systems, and also to the physical space that they occupy which makes the humanlike design of the head more difficult.

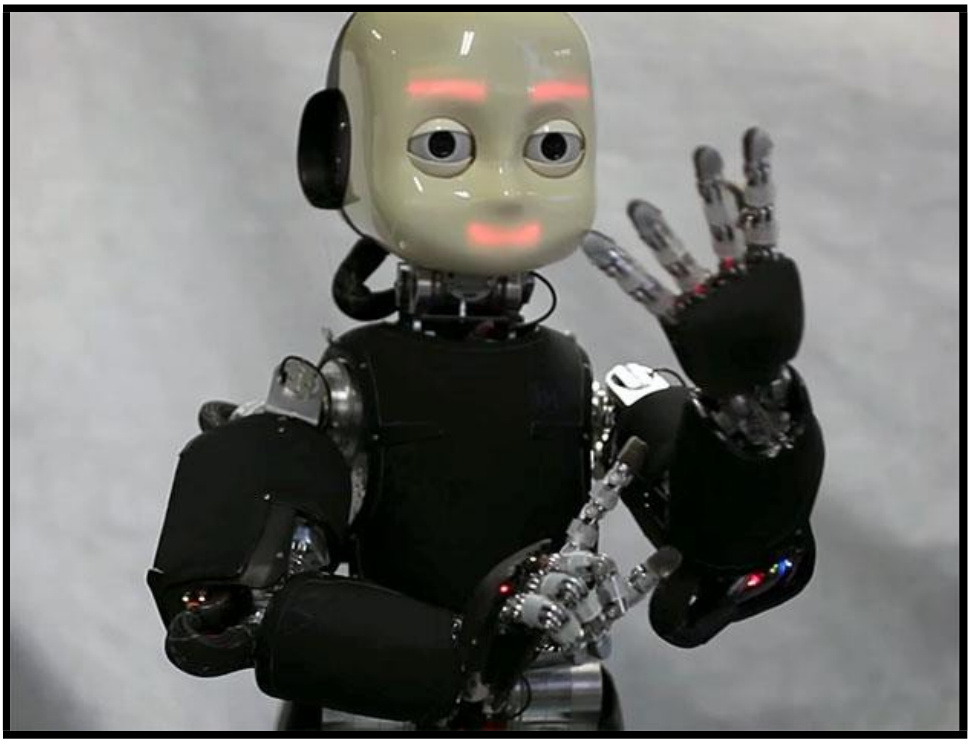

Figure 2.2 iCub (Beira *et al.,* 2006).

However, with advances in robotic technologies, and following on from recent research, robotics has now reached the point where robotic heads can be both sensor and social heads (*ibid*). When designing and building humanoid heads for social interaction, a consideration is to avoid what Mori *et al*. (2012) called 'The uncanny valley.' This is where the head appears so human-like that it can cause humans interacting with it to become uncomfortable, yet is not human-like enough to be fully emotionally acceptable. This means that robot heads used for human interaction need to; a) Look like robots in appearance, or b) Be highly convincing in their head gestures. If route b) is pursued, they need to be able to closely mimic the velocities and ranges of the human anatomy that is being replicated, if they are to reproduce the gestures accurately. This has been attempted, and 'Flobi' (Lutkebohle

et al., 2010) is a good example of this. In this model, although an attempt has been made at mimicking human eye movements, the head/neck movements are not considered so closely. This is an important factor, as head movements perform an important function within human interaction, and therefore need to be considered when designing robots to interact with humans (Kuno *et al.,* 2007). What is common in the robots discussed here is the lack of consideration given to the non-rotational, lateral translations that human heads can make, thus preventing the accurate replication of human head gestures.

2.3 Mechanical techniques

In robotics, and in mechanical engineering generally, there are a wide choice of actuators available for providing linear and/or rotational movement. Historically, humanoid robots have in some way attempted to mimic the human form, but the mechanisms employed within have been very different to their biological counterparts (Marques *et al.,* 2010). Actuators have often been placed at the joints to enable just one axis of rotation by the motor (*ibid*). ASIMO (Figure 2.3) is an example of this design approach (hondaworld.com, 2015).

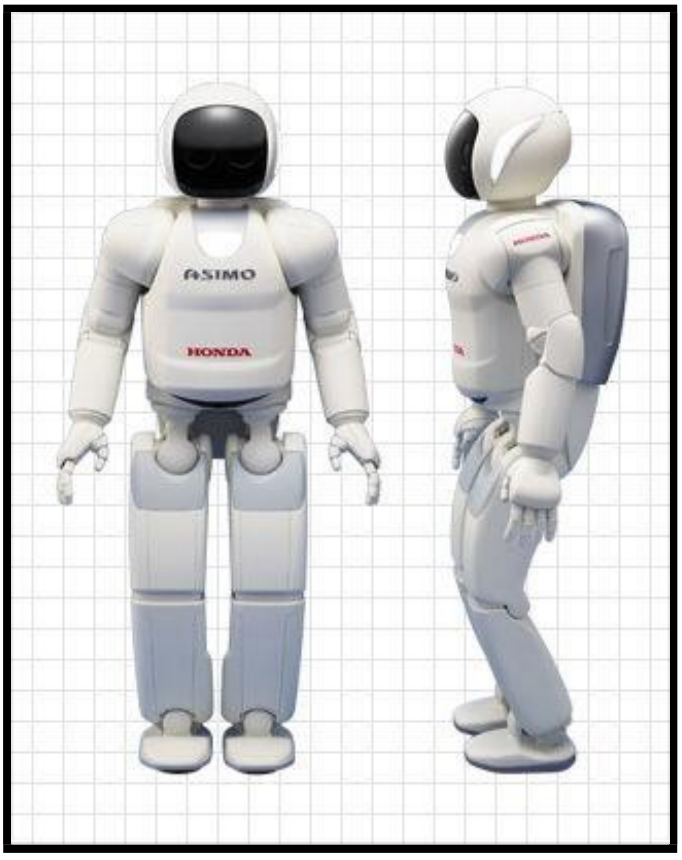

Figure 2.3 ASIMO (hondaworld.com, 2015).

However, for some time now, robotics researchers have been focusing on biomimetic robots (eg. Tondu *et al*., 1994; Yamaguchi *et al*., 1995), intent on not just replicating biological form and movements, but are also aiming to mimic the actuation mechanisms of biological organisms (Cocaud and Jnifene, 2003). An example of this is the focus on tendon

driven systems which are continuing to be of increasing interest today, not just due to their biomimetic characteristics, but also because they can be used where it is necessary to have a complicated actuation routing in order to reduce weight and inertia within the systems (Jamone *et al*., 2010). The iCub (Metta *et al*., 2011) is somewhat of a compromise of the two systems of actuation in that it uses directly coupled motors to provide rotation, in addition to tendon based actuation.

When working with robotic representations of the human head and neck it is desirable to simplify the model of the neck due to the complexity of the actual biology, that is, with more than twenty muscles and ten bones, the neck is formed by seven vertebrae and the atlas that supports the skull. (Netter, 2010) as shown in Figure 2.4.

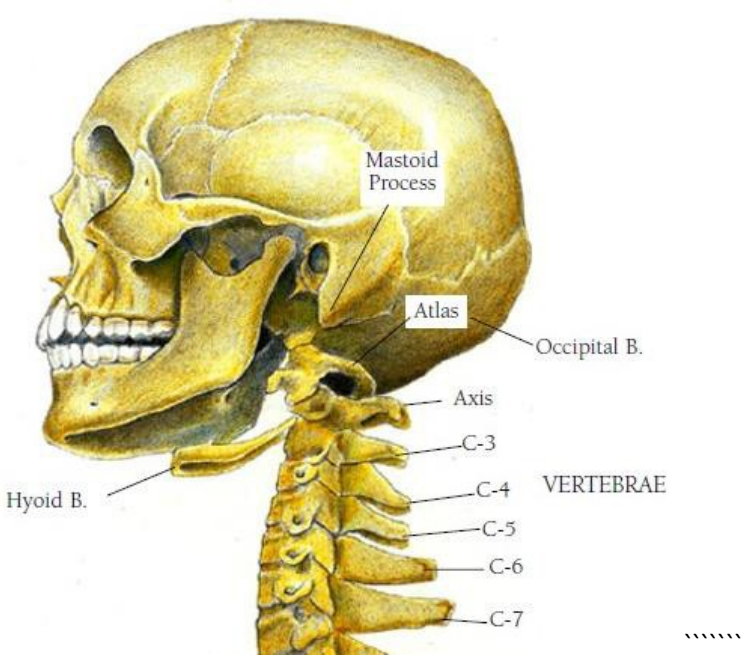

Figure 2.4 The human cervical spine, showing the biological arrangement that was used as a basis for this work (keywordteam.net, 2017).

The vertebrae could be seen as a flexible spring providing flexion/extension and adduction/abduction motion. Rotation and an upper flexion/extension is provided by the atlas bone. Looking at the need for simplification of biomimetic modelling, Jamone (*et al.,* 2010) proposed a design where a spring is used as the cervical vertebra, and steel tendons to represent the muscles. This is essentially a modified Stewart Platform (Stewart, 1965), and is shown in figure 2.5. A Stewart platform itself is a device with two parallel platforms connect by six prismatic actuators. The six actuators are attached in pairs at three locations on the baseplate. Such an arrangement is commonly used in applications such as flight simulators, as it allows the top plate six degrees of freedom. In such cases, the actuators are often hydraulic.

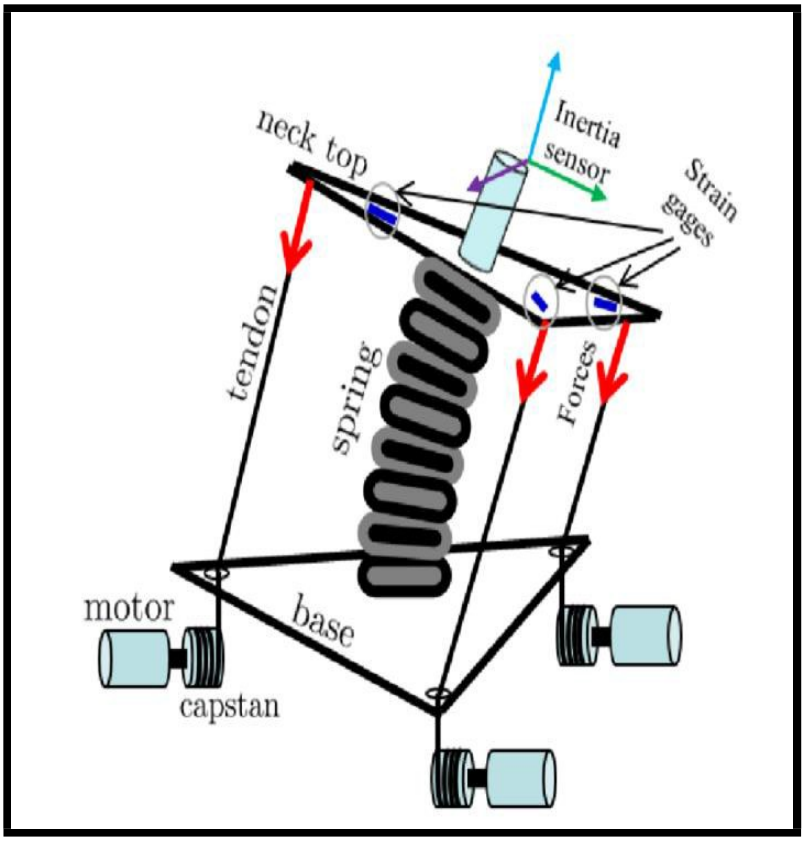

Figure 2.5 Tendon-driven neck (Nori *et al.,* 2007).

Whilst this design does provide roll and pitch movements, additional actuation would be needed to provide yaw (rotation left to right). This is due to the fact that normally, open-ended tendon based systems require more tendons than there are degrees of freedom (DOFs), as the tendons can only exert tension and not compression (*ibid*). As can be seen, in this case, the system has 3 tendons, thereby limiting the DOFs to 2 (pitch and roll). An additional problem of the approach taken with this design is that the spring is compressed by the weight of the head sitting on it, therefore altering the dynamics of the system. Also, as with the previous systems, it also lacks the ability to perform purely non-rotational lateral translations. As the figure 2.5 shows, it can perform lateral translations, but they will always be accompanied by rotational movements.

Due to the inherent problems with the schemata above, it is more convenient (and biologically accurate) to employ agonist-antagonist pairs in tendon driven systems. Marques (*et al.,* 2010) proposed a design using such agonist/antagonist pairs with the ECCE1 upper torso humanoid robot (*ibid*). They say that '… its joints and musculo-tendon-skeletal structure were inspired by its anthropological counterpart…' (*ibid*, p.393). As can be seen from the photo of ECC1 (figure 2.6), the biological accuracy of this representation is open to conjecture, for instance in the lengths of the muscles driving the neck. This design used DC motors as the primary actuators, with kite line and marine grade shock (elastic) cord as the tendons.

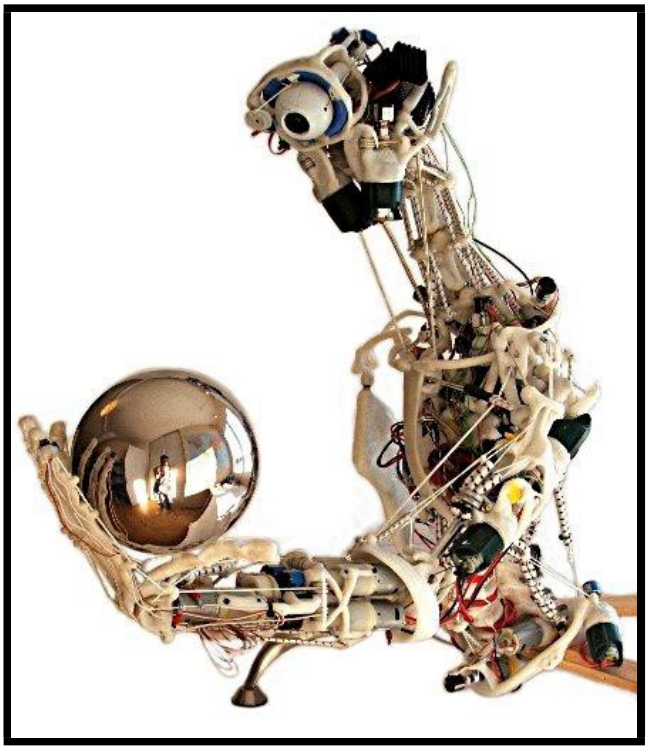

Figure 2.6 ECCE1 (Marques *et al.,* 2010).

As can be seen, the system uses some very long, unsupported cables. This along with the elasticity of the marine grade shock cord has led to a great amount of wobble (instability) and overshoot within the system, as can be seen in videos of its operation, which in turn has led to poor performance in mimicking the kind of biological movements that this research is aimed at achieving.

2.4 Pneumatic air muscles (PAMs)

The actuators used for this robot are pneumatic air muscles (PAMS). They were chosen for their resemblance to skeletal muscle (Daerden and Lefeber, 2002) and also because of their high power to weight ration of 10KW/Kg (Hannaford and Winters, 1990). The desire to achieve biomimetic operation, that is, to use actuators that like biological muscle, bulge as they contract, precluded the use of other actuators, such as hydraulic or electromagnetic.

PAMs were first developed by Morin (1953), but came to wider attention after McKibben used them as actuators in artificial limbs after his daughter contracted polio, due to the fact that they demonstrated similar load-length curves to skeletal muscle (Hannaford and Winters, 1990). Daerden and Lefeber (2002) define PAMs as inverse bellows, that is, they contract on inflation. They are gas pressure operated, contractile linear motion actuators (*ibid*). Two examples of these that were built by the author are shown in figure 2.7.

Figure 2.7 PAMs (constructed at Oxford Brookes University, 2014).

The muscle is composed of a braided tube surrounding an inner air bladder. Figure 2.8 shows a basic view of their construction and operation. The braided tube chosen was made from polyethylene terepthalate monofilament yarns. This was an ideal material as it has great tensile strength and is resistant to abrasion. Originally, the material chosen for the inner air bladder was rubber. This however perished very quickly, and silicon tubing proved to be a much better alternative.

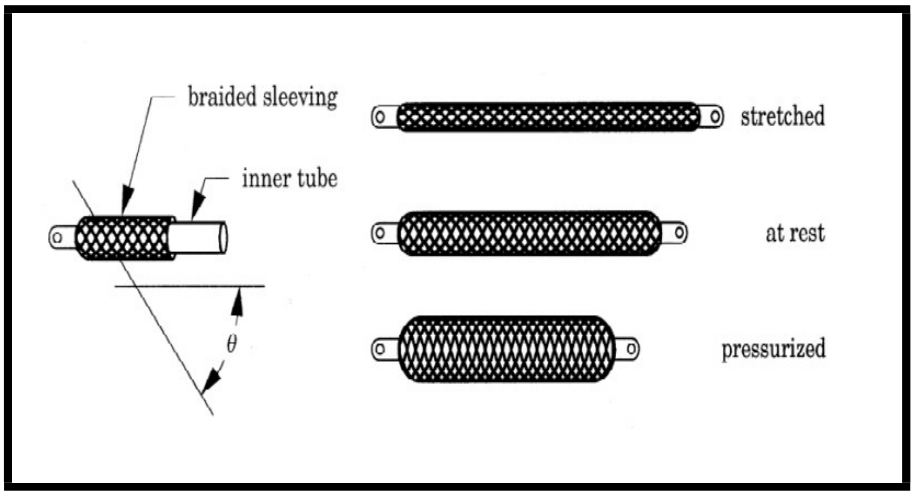

Figure 2.8 Construction of PAM (From Daerden and Lefeber, 2002).

As can be seen, the outside of the PAM consists of a braided sleeve, which is responsible for providing the tensile force. The braids run in a helical fashion along the muscle's length at angles of + ϕ and – ϕ. Inside this braid is an inflatable tube, which when pressurised with air attempts to inflate like a balloon, that is, to expand (in this diagram) in a vertical direction, causing it to press against the braid. As can be seen, this causes the braid to also expand vertically, thus increasing the angle Ø, causing the braid to contract in the horizontal direction. The effect of the change in muscle volume on the braid can be seen in figure 2.9.

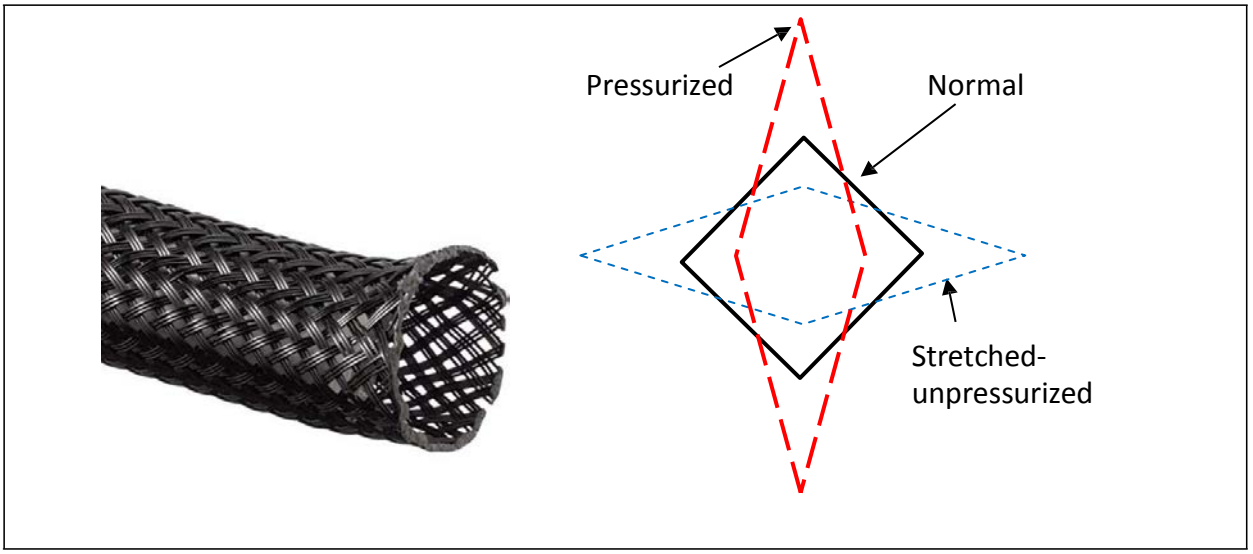

Figure 2.9 Mesh behaviour at differing air pressures

Drawing the diagonals of the diamond, it can be seen that the angles of the strands within the mesh change with pressure. It is known that the length and pressure have an inverse relationship, and this is shown in figure 2.10.

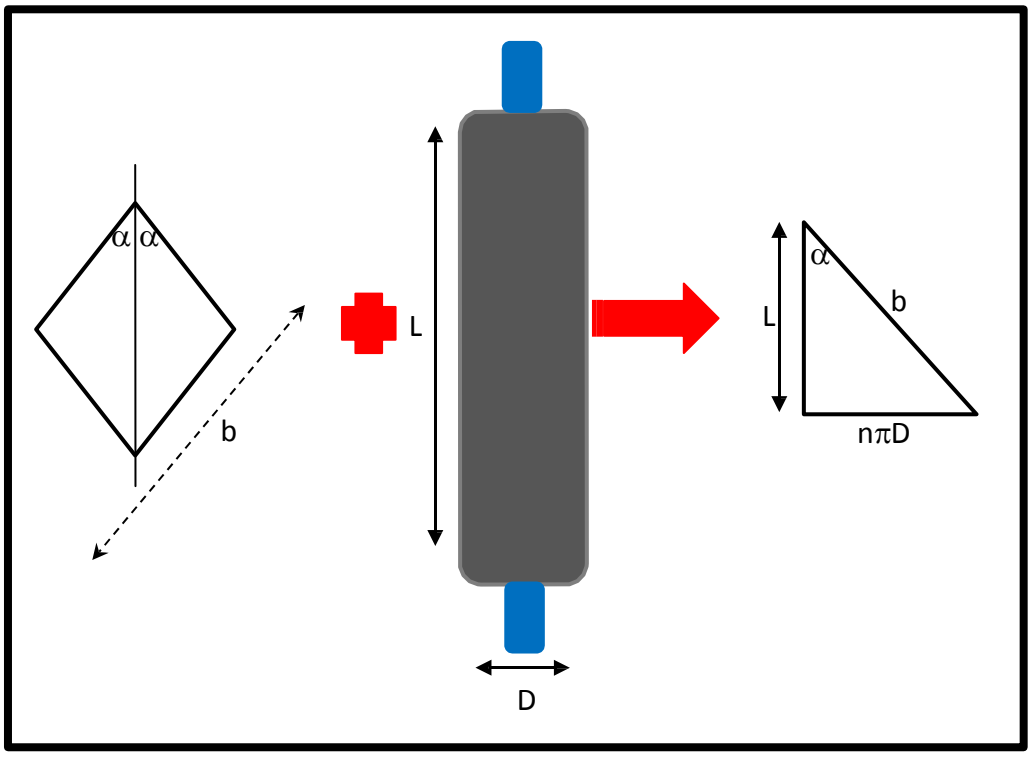

Figure 2.10 Relationship of muscle length (L), muscle diameter (D), and the angle between the mesh strands and cylinder (α) (Rodriguez and Valenezuela, 2011).

Where L is the muscle length, n is the number of strands, D is the muscle diameter, and α is the angle between the mesh strand and the cylinder main axis. The line b represents the fixed braid length. Because the muscle volume is considered to be a cylinder, that is, without the curved ends, the model has to be considered somewhat idealised, so some correction is needed for use of this model.

As can be seen in figure 2.11, at zero length the muscle has zero volume. As the model is based on a cylinder, this means that the cylinder is reduced to a disk, with the mesh fibres forming a zero volume cylinder. Conversely, at maximum length, the fibres form a straight line, again without volume. This means that theoretically, no contraction occurs at these extremes. Although in reality this could not occur, it does show that contraction is minimised when the muscle is stretched.

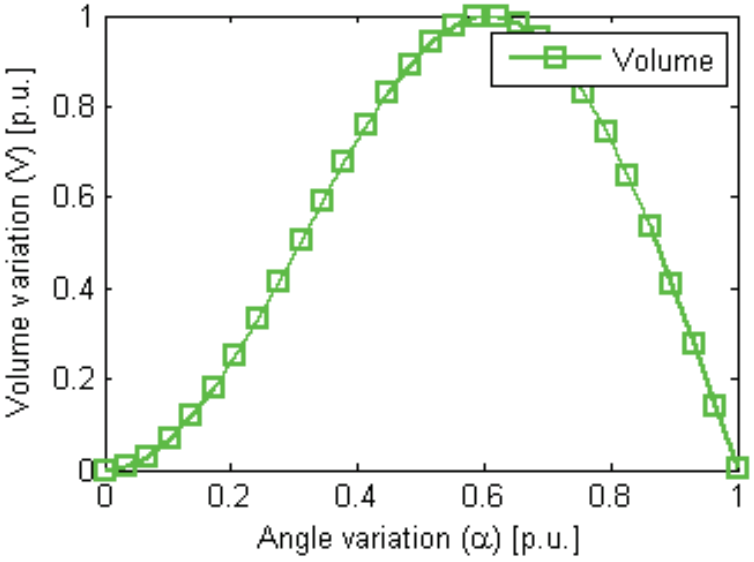

Figure 2.11 Correlation between volume and length with change in angle (Rodriguez and Valenezuela, 2011).

Rodrigues and Valenezuela (2011) also developed a model of the muscle characteristics for constant air pressure supplies, and this is shown in figure 2.12. The contraction ratios in this model must not be considered universal (as far as PAMs are concerned) however, as it does depend upon the individual characteristics of the air muscle under test. It does, however demonstrate a universal principle

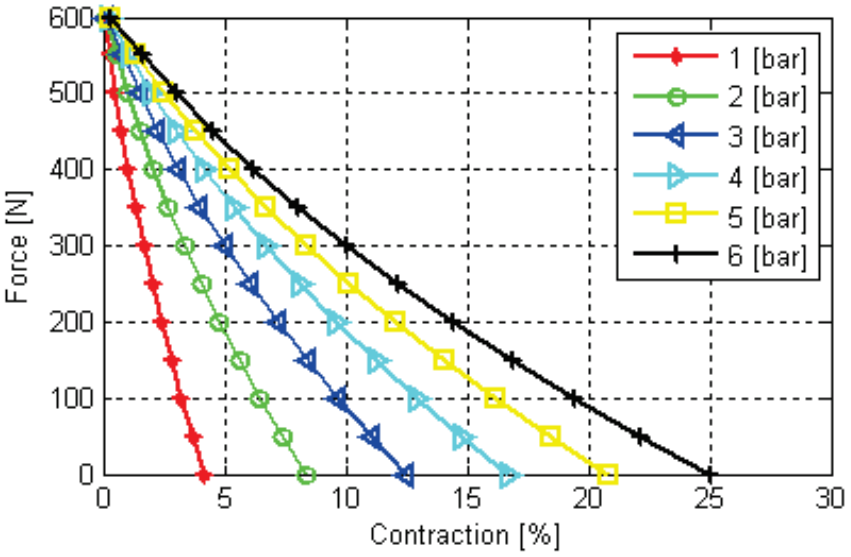

Figure 2.12 Muscle characteristics with a constant air pressure (Rodriguez and Valenezuela, 2011).

As can be seen in figure 2.12, the forces reduce in a near linear fashion with contraction. The greatest force occurs at the start of the contraction. This means that the initial muscle acceleration is greater.

This model does not include considerations such as the friction of movement within the braid fibre. Models with greater accuracy can be found in Chou and Hannaford, 1996; Tondu and Lopez, 2000; Colbrunn *et al.,* 2001, and Davis *et al.,* 2003). Tondu (2007) discusses the static analogies between PAMs and biological muscle, which can be summarised as:

1. The static tension is proportional to the pressure, which is analogous to neural activity setting the stiffness or (conversely) compliance.
2. The static tension is proportional to the initial muscle cross section.
3. The static tension decreases with increases in contraction ratio.

Regarding the compliance issue in (1) above, Van Ham (*et al.,* 2009) define compliance as the ability to minimise large forces due to shocks – such as when robots and humans operate in the same physical environment. Industrial robots tend to be operated in human-free environments, as they are normally 'stiff'' systems due to the (normally) conflicting need for high positional precision (*ibid*). It is sometimes necessary, however, for humans and robots to perform tasks together (Zinn *et al.,* 2004), and this is where the inherent compliance of PAMs can prove useful. This compliance is also useful when performing non-rotational movements, where it is almost inevitable that some stretching of the muscles will occur.

2.5 Control techniques

Now the mechanical/skeletal issues have been covered, this section will discuss the control issues. As was seen in the preceding section, to control PAMs, it is necessary to control the air pressure being fed to them. There are two main approaches to this, namely, on-off valves (Vanderborght *et al.,* 2004), and proportional valves (festo.com, 2015). As their names imply, the on-off valves could be considered a 'digital' approach to pressure control, whilst proportional valves provide a true analogue control, that is, the allow any pressure to be set between zero and the maximum limit.

When using on-off valves in PAM based actuator systems, it is important that they are able to operate 'dynamically, that is, at high speed (Vanderborght *et al.,* 2004). The mechanical constraints of the valve can be an issue here. They do however have the advantage of easier interfacing to (mainly digital) electronic controllers, as they only need on-off commands, rather than analogue signals. Proportional valves however, do have the big advantage of being able to provide infinitely adjustable pressures (festo.com, 2015). One of the most well-known suppliers of proportional valves is FESTO. Indeed, their brand name

has become synonymous with proportional valves, that is, they are often referred to as 'FESTO valves.'

FESTO proportional pressure regulators are closed-circuit devices that continuously compare the pressure input with the output pressure as set by an analogue input control voltage. If a deviation occurs, the proportional regulator adjusts to correct this (*ibid*). A FESTO proportional pressure regulator is shown in figure 2.13. The dimensions are 110.4mm x 41.5mm x 65.4mm, and the weight is 400g.

Figure 2.13 FESTO VPPM proportional regulator valve (*ibid*).

Pressure regulators typically require a DC power supply (24V, in this case), and a set point signal which can be either voltage (typically 0-5V or 0-10V), or current (typically 4-20 mA) (equlilibar.com, 2015). Models with digital circuits can accept serial communication, such as RS232 or DeviceNet. Figure 2.14 shows the typical configuration of a proportional pressure regulator valve.

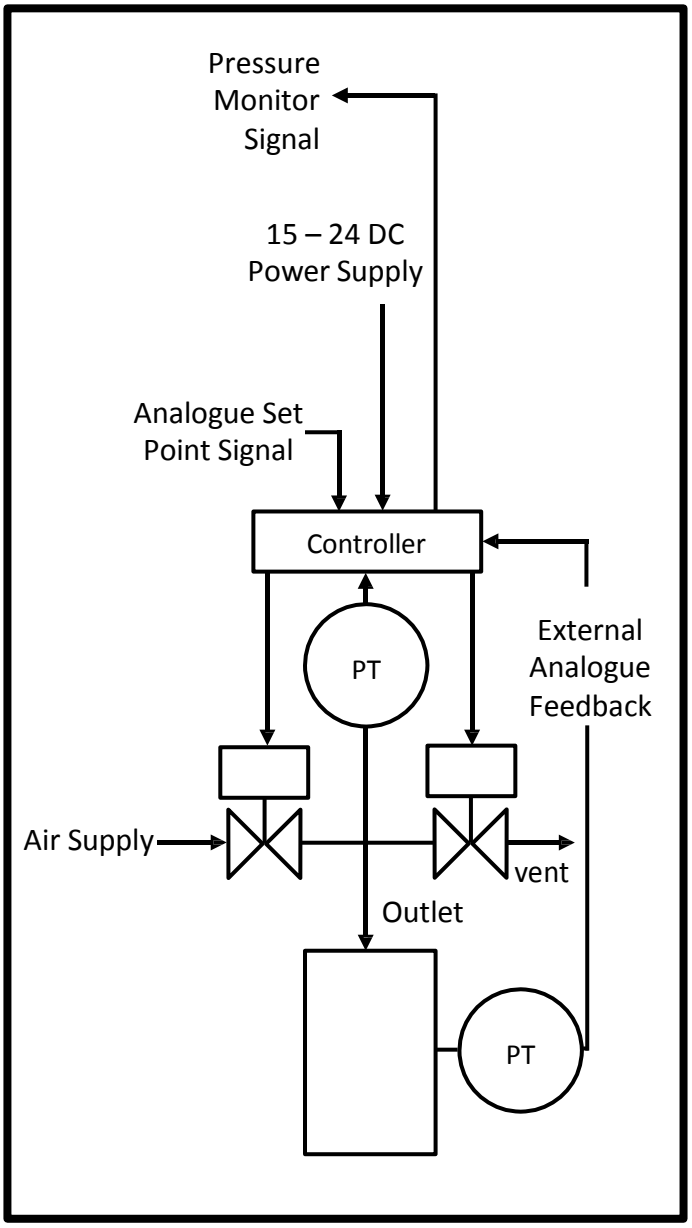

Figure 2.14 Proportional pressure regulator valve schematic showing the arrangement of the pressure regulation system (*ibid*).

As can be seen, the system is powered by a DC voltage. The analogue set point signal is the one that carries the desired system pressure to the controller. This is in the range 0 V-+10 V, for a pressure range of 0 – 10bar. Air is fed at a higher pressure than is required by the system via the valve on the left of the diagram. Two pressure transducers (labelled PT) monitor the system and process pressure to the controller, which in turn operates the outlet and vent valves to maintain the desired pressure in the process. The FESTO VPPM valves have three modes of operation, as shown in figure 2.15. The system default is “Normal” mode. This was the mode chosen for this application, as the air volume was considered medium.

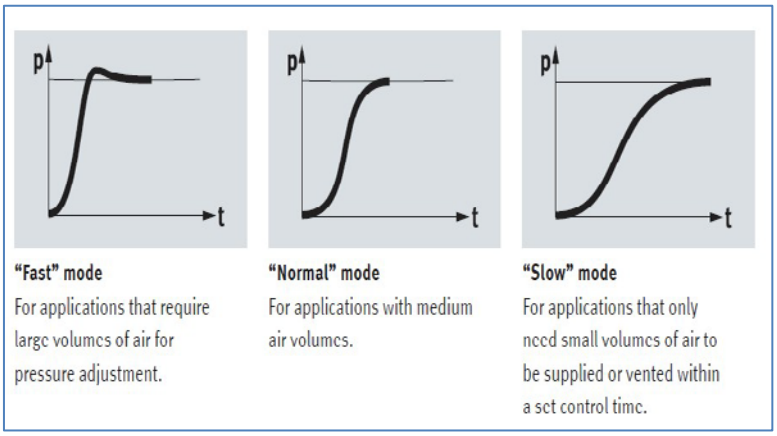

Figure 2.15 The three modes of operation of FESTO VPPM valves (festo.com, 2015).

2.6 Electronic Approaches

As was seen in the previous section, most proportional pressure regulator valves need an analogue set point voltage to control them. It is usual for control systems to use digital microcontrollers, and these often lack an integrated digital to analogue converter (DAC) (Wang *et al*., 2012) to generate the analogue voltage required to drive the proportional valve. The use of external DACs would add to the cost, and also occupy the digital I/O ports of the microcontrollers (*ibid*). Some microcontroller manufacturers, such as Atmel and Texas Instruments have designed a compromise around this problem, by using their inner counter timers and software to produce a pulse width modulation (PWM) output (atmel.com, 2015), which can be used (for instance) to control the speed of conventional DC motors. If required, this PWM signal can be further processed to provide a true analogue signal (Wang *et al*., 2012). Thus, PWM has been described as '…a technique for getting analogue results with digital means…' (arduino.cc, 2015(a)). It consists of using a square wave signal to represent different analogue values by varying its duty cycle. This is shown in figure 2.16.

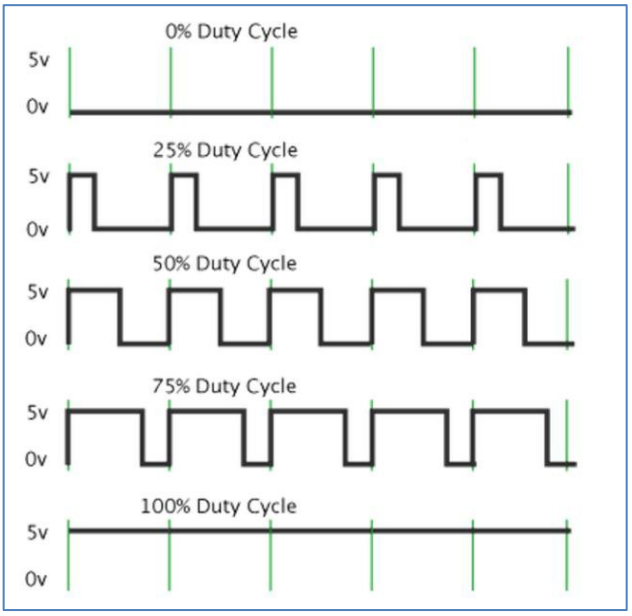

Figure 2.16 Pulse Width Modulation (ibid).

In the above diagram we take the analogue output voltage range these signals represent to be in the range 0V – 5V (for instance), and the green lines to represent regular time periods. In this example, based on the Arduino (*ibid*), these time periods are 2ms apart as the PWM frequency is 500 Hz. When the PWM is representing 0V, this is reflected as a 0% duty cycle (always off). At the other end of the spectrum, 5V would give 100% duty cycle (always on). Also shown in the diagram above are representations of 1.25V (25% duty cycle), 2.5V (50% duty cycle) and 3.75V (75% duty cycle). All other values between 0V and 5V can be represented by varying duty cycles anywhere between 0% and 100%, although it must be borne in mind that the Arduino only outputs 256 discrete levels.

Regarding the generation of these PWM signals, the data sheet for the ATMega2560 (atmel.com, 2015) shows a simplified representation of the 8 bit counter/timer, which is used for PWM code generation. This is shown in figure 2.17.

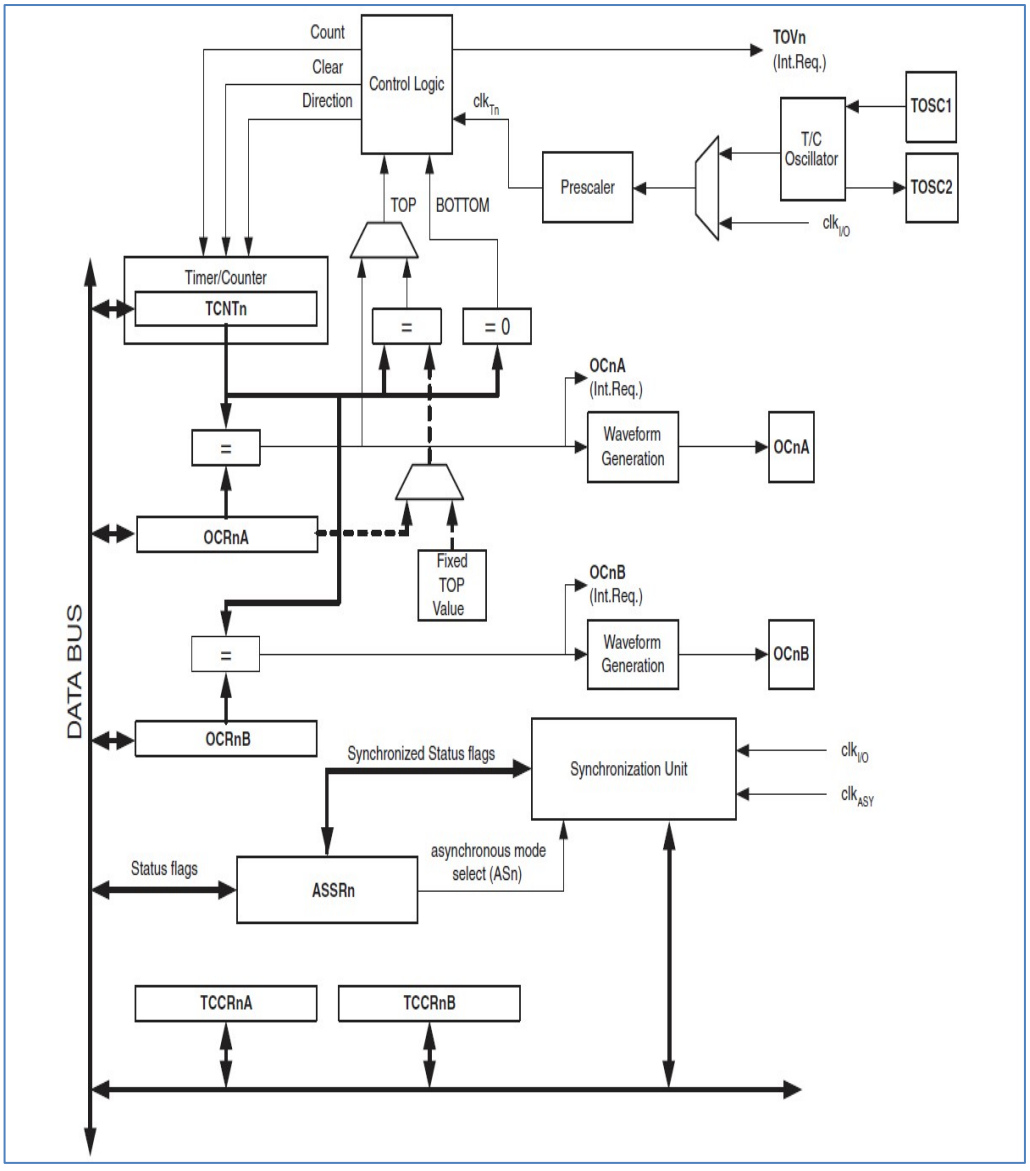

Figure 2.17 Timer/Counter 2 of Atmel ATMega 2560 (atmel.com, 2015).

The Timer/Counter (TCNTn) and the Output Compare Registers (OCR0A and OCR0B) are both 8 bit devices. A comparison is continuously made between the Timer/Counter value and the double buffered Output Compare Registers (OCRnA and OCRnB) as shown in figure 2.18. The results of this comparison are used to produce the PWM output on the Output Compare pins (OCnA and OCnB) by the waveform generator. The timer is incremented by 1 from 0x0000 to 0x00FF, after which point is rolls over back to zero. During this period, when the counter value equals the comparative value from OCRnA and OCRnB the output is forced low. When the top value is reached by the counter, the output is set high. In this way the PWM is generated (*ibid*).

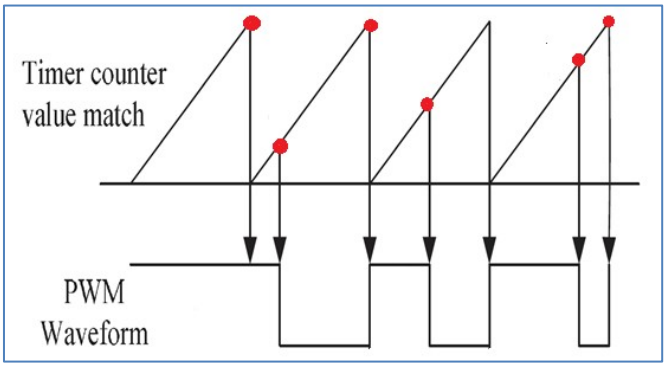

Figure 2.18 Generation of a PWM signal (Wang et al. et al.., 2012).

As can be seen in figure 2.18, although the circuitry provides a digital representation of an analogue signal, some processing is needed to make the signal truly analogue. Wang (*et al.,* 2012) discuss the use of a low-pass filter to achieve this, with the basis for their design topology being a double-T band-stop filter, as shown in figure 2.19.

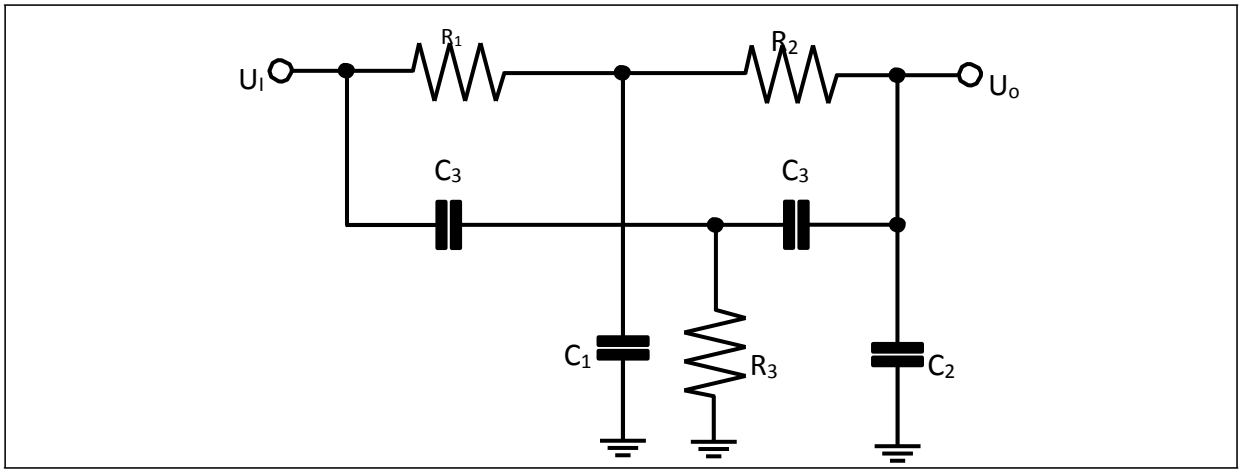

Figure 2.19 Double-T filter circuit (*ibid*).

The double filter is composed of a two passive (RC) filter circuits connected in parallel, thus creating a two pole stop-band filter circuit. The two C3s and R3 form the high-pass filter, and R1, R2, C1 and C2 form the low-pass filter. When the input frequency fed into U1 is too low, the impedance of C3 is high, and the signal is transferred to U0 via R1 and R2. However, should the frequency be too high, C1 and C2 become low-impedance, thus shorting the signal to ground. It can therefore be seen that with the correct values for the

resistors and capacitors, this circuit could be used to filter out the 500Hz component of the PWM signal from the microcontroller. As the desired analogue voltage varies comparatively slowly over time, it was demonstrated (*ibid*) that a simplified version of the double-T circuit, that is, as simple low-pass filter was sufficient for the purpose. They also added gain to the circuit by use of an operational amplifier as shown in figure 2.20.

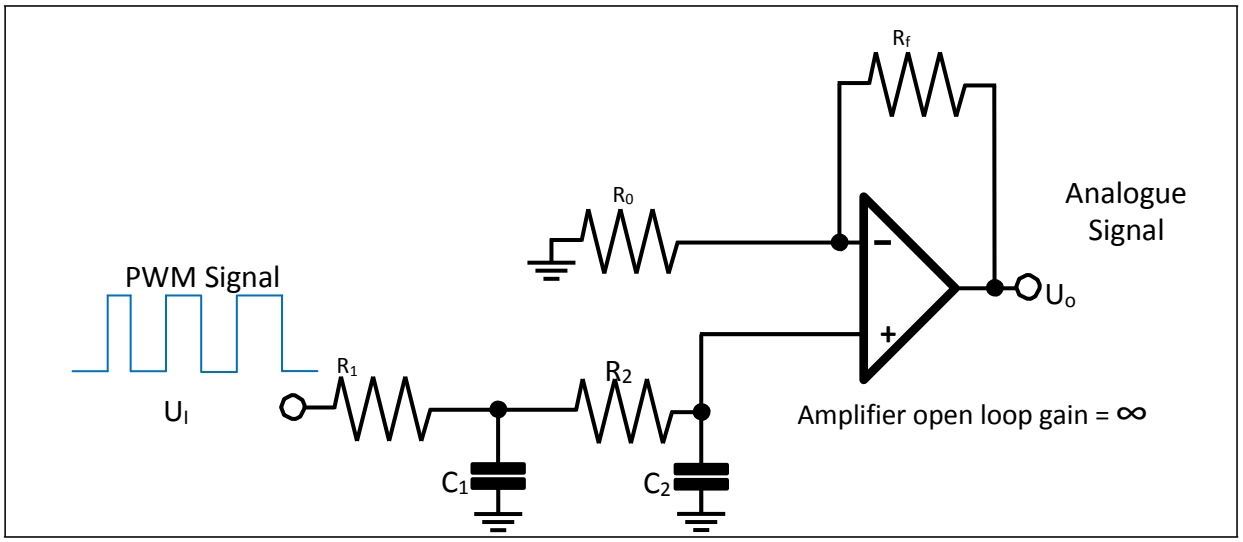

Figure 2.20 Low pass filter (*ibid*).

Here, as can be seen, the circuit consist of a low-pass filter, comprising R1, R2, C1 and C2, followed by a non-inverting amplification circuit, with a gain of 1+Rf/R0.

This concept was tested in a MATLAB simulation (*ibid*) with a PWM input of 15.625 kHz, as is commonly used in motor control. This is shown in figure 2.21, with the resultant analogue voltage shown in figure 2.22.

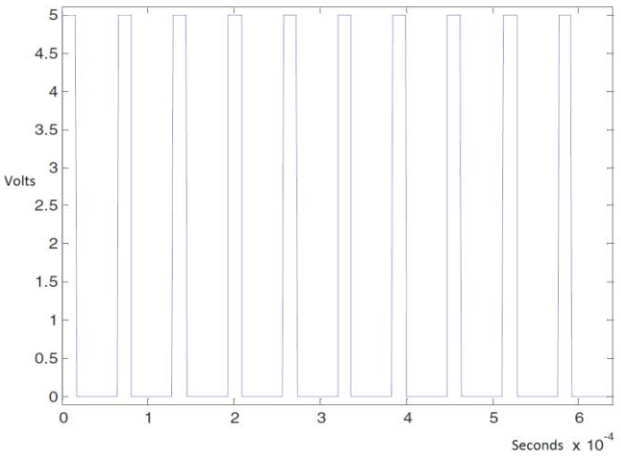

Figure 2.21 Input PWM (*ibid*).

As can be seen from figure 2.22, following an initial period of 2ms, the voltage settled down to a constant analogue value representative of the duty cycle of the PWM signal, with the high frequency element removed.

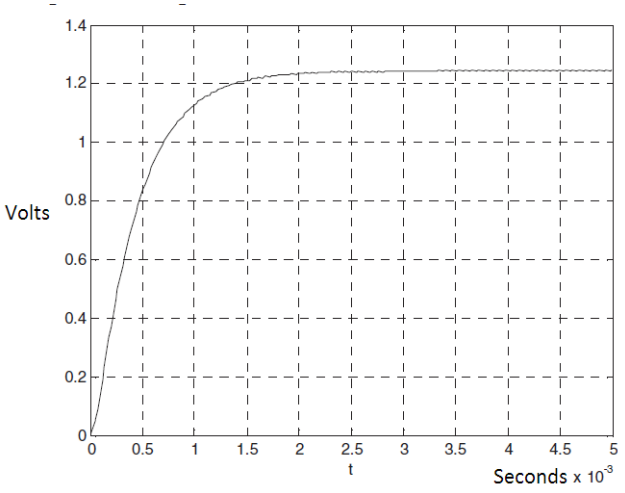

Figure 2.22 Resultant analogue signal (*ibid*).

2.7 The biomechanics of human head movement

This section discusses the biomechanics of human head movement, showing the mechanisms involved in moving the head in three dimensions. Also discussed is the unsuitability to represent head movements in terms of only the three rotational dimensions, as the head is also capable of non-rotational lateral movements, as is shown later in figure 2.27. Together, these dimensional capabilities provide the capacity for the head to move in extremely complicated and (sometimes) subtle ways – as is the case of head gestures during interpersonal communication.

2.7.1 The human cervical spine

The structure of the human cervical spine consists of 7 cervical vertebrae (referred as C1 to C7), the actual controllable kinematic units from the skull to the thoracic spine being the atlas, the axis, the C2-3 joint and lower cervical spine (Bogduk and Mercer, 2000). The vertebrae in the cervical spine cannot be controlled independently of each other. Figure 2.23 shows the cervical spine.

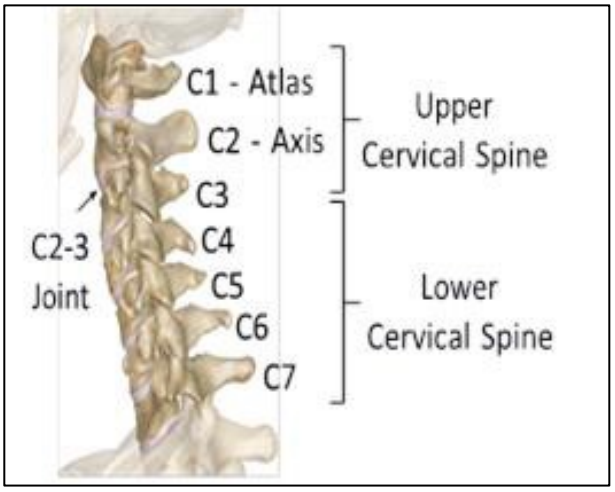

Figure 2.23 Anatomical representation of a human neck illustrating its four major kinematic units: Atlas (C1), Axis (C2), C3 vertebra and its C2-3 joint and the Lower Cervical Spine (C4-C7) (Taylor, 2012).

The atlas (C1) is the most superior vertebra of the cervical spine and supports the skull. The union between the skull and atlas only permits flexion and extension movements (i.e. nodding - pitch) relative to the atlas, otherwise the skull and the atlas move and function essentially as one unit. The axis (C2) is the second cervical vertebra. Its principal function is to provide the pivot upon which the atlas (and therefore the head) rotates side-to-side (yaw) relative to C2. Vertebrae C1 and C2 constitute the upper cervical spine and are responsible for most of the rotation of the neck. The C2-3 joint is a transitional joint linking the upper cervical spine with the lower cervical spine and therefore must accommodate the varying demands of the neck above and below it (Liebenson (1996). The lower cervical spine groups C3-C7 vertebrae. These have common morphological and kinematic features, and are stacked on one another, thus are very different to the classical 3 axis representation of robotic heads. Each one of these C3-C7 vertebrae has three axes of rotation, two active and one passive. The active axes permit flexion/extension and lateral flexion, and the passive axis (yaw) does not move unless lateral flexion takes place.

2.7.2 Motion of the cervical spine

This research considers four different pairs of muscles in the design of the robotic neck (see Figures 2.24 and 2.25) as biological studies have shown that these pairs of muscles are the primary drivers of head motion (Dutia, 1991; Tilley, 1993), and they should therefore be sufficient to replicate the complexity of the human neck and emulate its normal range of motions. Neck muscles operate in antagonistic pairs located at opposite sides of the cervical vertebrae. These muscles are:

The Splenius Capitis muscles which are located at the back of the neck (see Figure 2.24). They connect the base of the scull with the upper thorax causing the head to rotate and bend towards either side. These muscles are antagonist to Sternocleidomostoid muscles in the rotation of the head.

The Longissimus Capitis muscles which are at both back sides of the neck (see Figures 2.24 and 2.25). They originate from the superior thoracic vertebrae and are attached to the mastoid process bone. This extends the head (nod) and laterally flexes and rotates (tilt and rotate) by the same amount. This pair of muscles is antagonist to Longus Colli muscles in the flexion of the head.

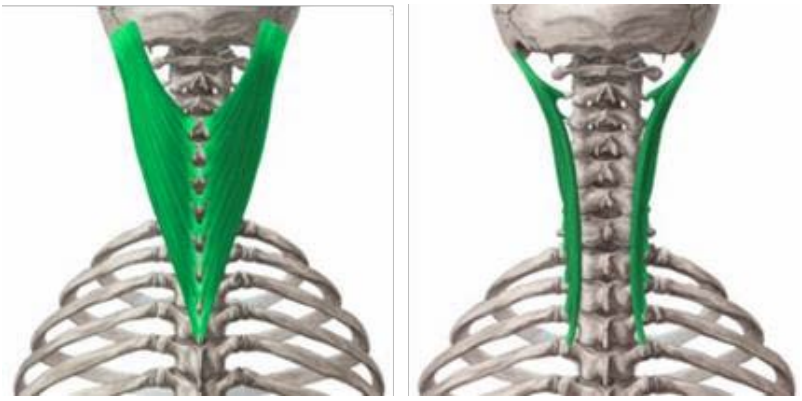

Figure 2.24 Splenius Captis (left) and Longissimus Captis (right) (kenhub.com, 2016).

The Sternocleidomostoid muscles which are located at the front side of the neck and connect the mastoid bone with the sternum and clavicle (see Figure 2.25). They are responsible for the rotation of the head and neck.

The Longus Colli muscles which are situated in the frontal side of the neck, between the Atlas and the upper-most thoracic vertebrae (see Figure 2.25). They are responsible for the cervical flexion (nodding), ipsilateral side flexion (tilt) and cervical rotation (rotate. These muscles also have a postural function.

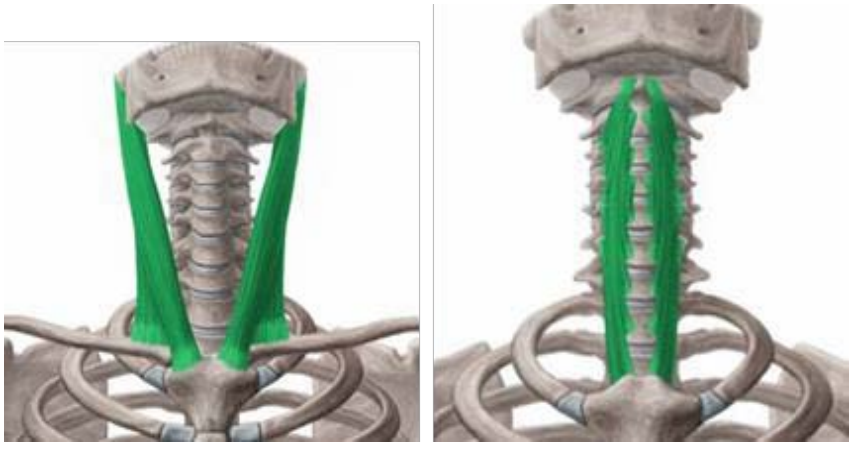

Figure 2.25 Sternocleidomastoid (left) and Longus Colli (right) (*ibid*).

In robotics, human head movement is normally considered in terms of Pitch, Roll and Yaw, using rotating vectors for the description as shown in figure 2.26. However, there is a problem with this model, as it gives the impression that head movements are purely rotational, in this case around an original centred at the intersection of the Pitch, Roll and Yaw axes.

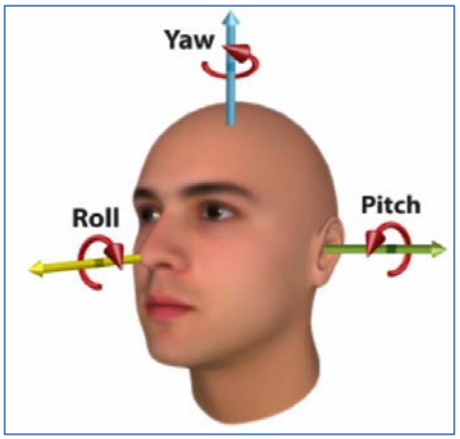

Figure 2.26 Human head roll, pitch and yaw (Arcoverde *et al.,* 2014. P.281).

This model is misleading, however, as there is also a lateral displacement due to the fact that the multi-joint neck is also involved in these movements. Such a description does allow the orientation of the axis of the head and the angle of rotation to be defined, but it cannot define the location of the rotation in 3D space (Mendendorp *et al.,* 1998). A more realistic view of these movements is depicted in figure 2.27.

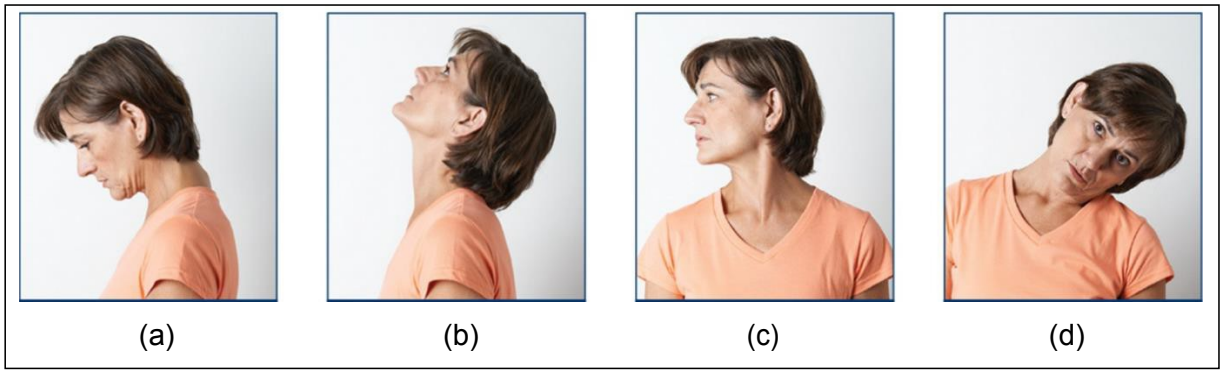

Figure 2.27 Lateral displacements during head rotation (xeomin.com, 2017).

As can be seen, human head movement is never purely rotational, due to the multi-jointed neck also being involved in the movements, which gives rise to a lateral displacement. At first glance, in figure 2.27(c), the displacement during rotation may not be so apparent, but it must be remembered that the cervical spine joins the back of the head and not the centre, thereby causing lateral displacement during this movement too.

In addition to the movement thus far mentioned, human heads are also capable of voluntary non-rotational lateral movement. For instance, these include a front-back sliding manoeuvre, such as may typically indicate surprise (slide back) or interest (slide forward). The head is also capable of a shoulder-shoulder sliding manoeuvre, as is seen in Indian traditional dancing. The literature does not consider these lateral movements when defining head movement ranges, and instead considers the whole head-neck mechanism only in terms of Nod, Tilt and Rotate angles. One can only surmise the reason for this is that they are not considered important in diagnosis, or that no accurate way of measuring them has yet been found. This has led many robots to be designed with only these considerations in

mind, and no consideration for the lateral displacements, hence the pan-and-tilt type designs that are so often seen, which can only offer non-biomimetic movements, hence making them seem very robotic.

Using the figures that are available in the literature for purely rotational movements, the average maximum ranges of movement and velocities for an adult male are shown in table 2.1. These figures show the total ranges given the movement of both the neck and head, whereas in humanoid robotics the rotations are often performed purely by the head. Neurological studies by Leigh and Zee (2015) show that under normal conditions, voluntary angular head velocities do not exceed 100 deg/sec for the various degrees of freedom for the neck.

Table 2.1 Average ranges of movement for and adult male (Fitzpatrick, 2010).

Total Nod	107°	<430°/Sec absolute maximum (involuntary) <100°/Sec (voluntary)
Total Tilt	90°	<360°/Sec absolute maximum (involuntary) <100°/Sec (voluntary)
Total Rotate	140°	<467°/Sec absolute maximum (involuntary) <100°/Sec (voluntary)

2.8 Summary

This chapter reviewed the literature that forms the foundation of the research. It covered contemporary approaches to humanoid robotic design, and the benefits and problems of each approach. In addition, the review also covered various the disciplines involved approached to the design of the component parts of the robot, *viz*, mechanical, control, actuation and electronic components. The chapter outlined the challenges in each of these areas, and a range of potential solutions to these challenges. Finally, it discussed the biomechanics of human head/neck movement, along with the problem of defining and measuring head movements purely in terms of rotational angular ranges and velocities, as is often used as the foundation for robot design, hence leading to non-biomimetic movement.

CHAPTER 3

PRODUCT DESIGN SPECIFICATION AND IMPLEMENATION

3.1 Introduction

This chapter records the explorative design process and the refinement and building of the complete system. The biomimetic neck design mimics the skeletal structure of the neck, and the main muscles within the neck responsible for head movement, and their attachment to the skull, in that they are attached to the skeleton and skull and the same points as in humans. This was aided by using a full sized (replica) skull as shown in Figure 3.1.

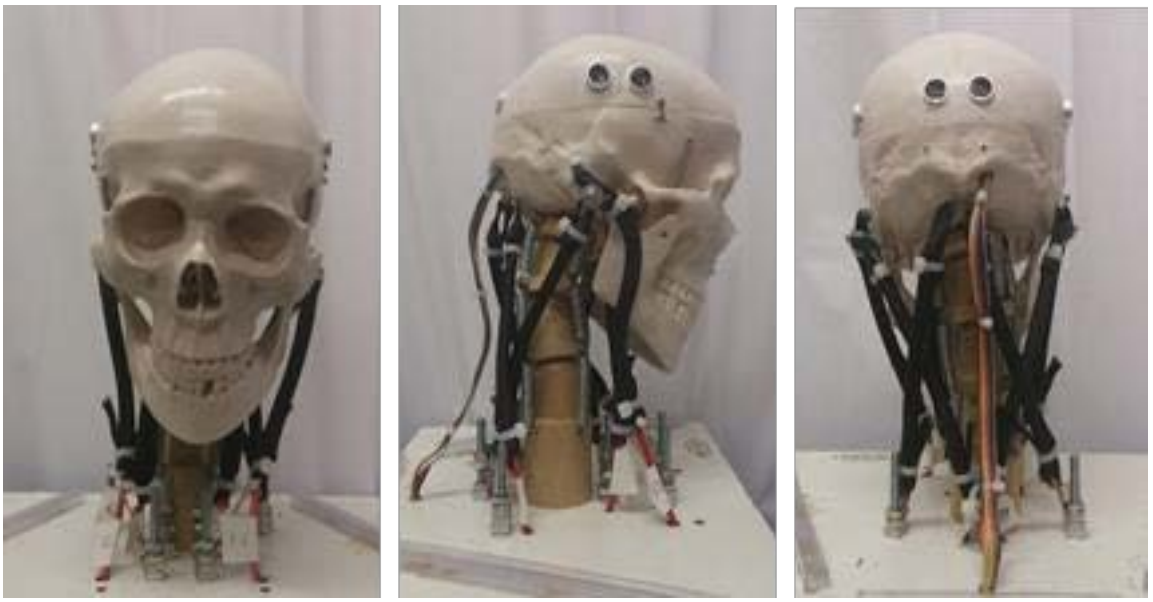

Figure 3.1 Front, side and rear views of the robot.

The robot neck was designed to have 8-DOFs arranged in four interconnected wooden vertebrae using ball and-socket joints that anatomically simulate and simplify the structure of the kinematic segments found in the human neck. The actuation was developed to closely mimic the arrangement the major muscles governing the motion of necks in humans, and meets this aim through the use of custom-made pneumatic air muscles. The goal of the proposed design is the replication of human-like movement and actuation.

As discussed in chapter 2, specifications for human head ranges and velocities refer to pure vector rotations, that is, without any mention of any linear translation that takes place. This has led to the development of robots that rely on these purely rotational specifications in their design, which in turn has led to an inability in them to provide this linear translation. This means that these robots will be incapable of realistically mimicking human head gestures. This issue will be addressed in the design specification of this robot, and forms the main original contribution.

3.2 Human head translations

To achieve the realistic replication of human head gestures, the robot should be designed to be able to perform the non-rotational, linear translations discussed earlier. These were the sliding shoulder-to-shoulder movement, and the sliding front to back movement, as shown in figure 3.1. In the diagram, they have purposely been exaggerated for the sake of clarity, although, as stated earlier, there are no measurements for these movements in the literature.

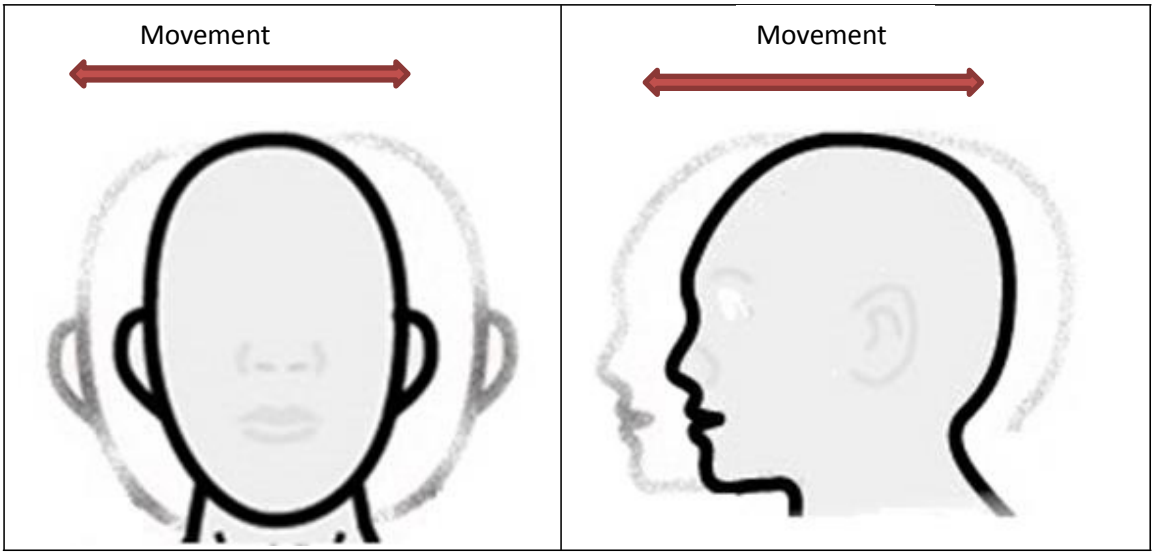

Figure 3.2 Non-rotational, linear translation.

In addition to having the ability to perform these non-rotational linear translations, the robot must perform movements that are purely rotational, as human head gestures often use both of these types of movement together. The desirable ranges and velocities for this rotational movement are shown in table 3.1, which were also discussed in the literature review. The absolute maximum figures for angular velocity are based on non-voluntary movements, such as those experienced in rapid accelerations and decelerations (Fitzpatrick, 2010), such as in car crash scenarios, and as such will not be used for evaluation purposes. The speeds for normal voluntary movement were used instead.

Table 3.1 Average ranges of movement for and adult male (Fitzpatrick, 2010).

Total Nod	107.5°	<430°/Sec absolute maximum (involuntary) <100°/Sec (voluntary)
Total Tilt	90°	<360°/Sec absolute maximum (involuntary) <100°/Sec (voluntary)
Total Rotate	140°	<467°/Sec absolute maximum (involuntary) <100°/Sec (voluntary)

As there are no figures in the literature for lateral movement, in table 3.1 only the angular ranges and speeds were considered for comparison when evaluating the performance of the robotic head. The lateral movements were measured, but without datum figures available in the literature, it was not possible to make any comparisons with human head capabilities.

In addition to the rotational and translational capabilities mentioned above, the following considerations were taken into account in the design of the robot:

- Simplified kinematic structure to reduce complexity whilst maintaining biological plausibility.
- Reliability and robustness. This robot will be used a lot in future work, and needs to be able to work for long periods without failure.
- Where possible, use of standard mechanical components to facilitate the easy modification and improvement of the humanoid neck.
- Modularity to ease the future redesign of the various systems involved.

During testing, the robot was programmed to perform the rotational movements, as they were comparatively simple to do. The more sophisticated translational/non-rotational movements as shown in figures 3.3 and 3.4 would require the development of more sophisticated control software, which is beyond the scope of this thesis. They will, however, be addressed in future work. However, to confirm that the robot could perform these non-rotational movements, they were measured during the Nod and Tilt experiments. They were not measured during the rotate manoeuvre as the gyroscope/accelerometer was fitted directly above the rotational axis for this movement, hence no lateral translation would occur.

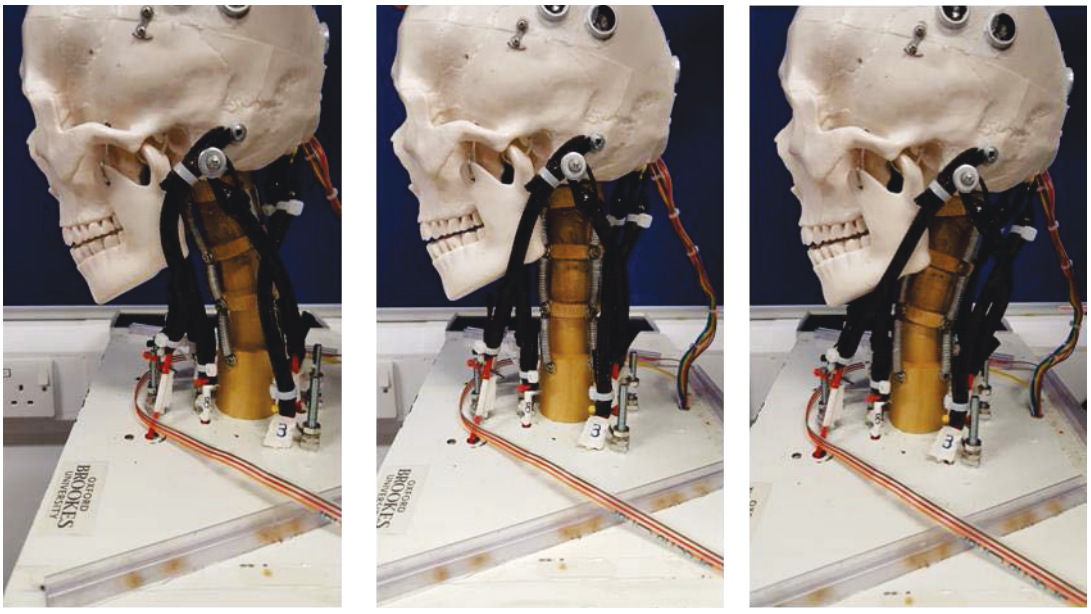

Figure 3.3 Front to back non-rotational linear translations.

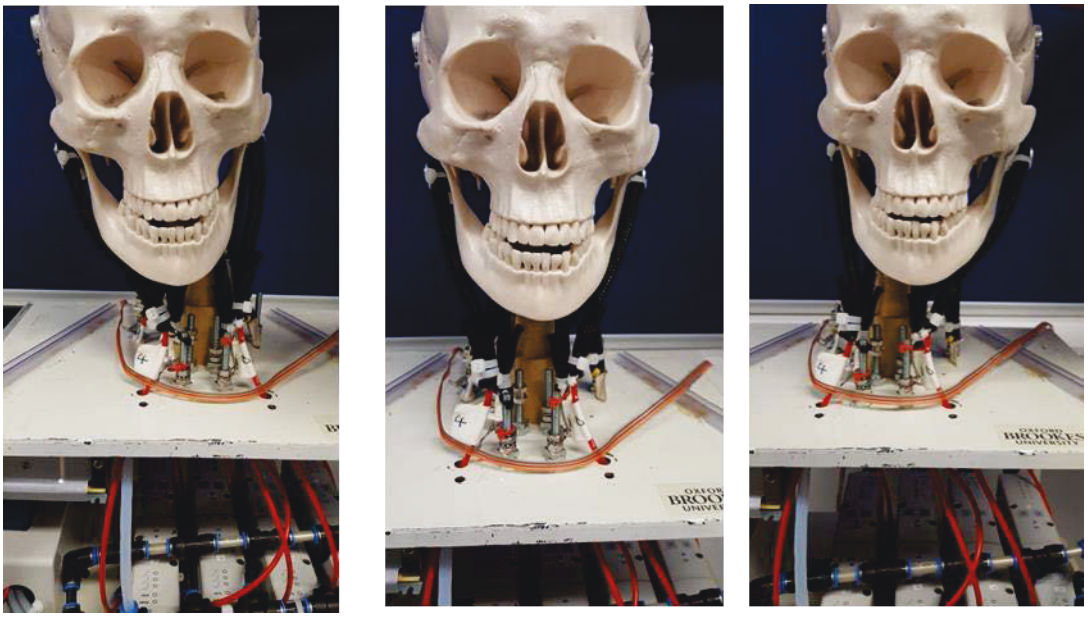

Figure 3.4 Side to side non-rotational linear translations.

3.3 The design approach

The design of the robot went through a number of variations and experiments, before a decision was made on the final design. The first design was developed purely to explore the limitations of a purely rotational approach in terms of pitch, roll and yaw when attempting to replicate human head movements. During the design process, simulation was not used, as the complexities of the cervical spine based approach used made simulation unfeasible in this research. Additionally, some of the parameters of the simulation would not have been known without actually building the neck and measuring them, thus negating the need for simulation.

3.3.1 A servomotor actuated neck

This was a simple head and neck robot based upon a pan and tilt mechanism which was actuated by servomotors. It also had 'eyes' consisting of USB cameras mounted on pan and tilt platforms that were actuated by servomotors. It was developed to understand the limitations of a pure pitch, roll and yaw approach to replications human head gestures, and also as a way of evaluating various items of control hardware that could be used in the final robot. The robot itself is shown below in figure 3.5.

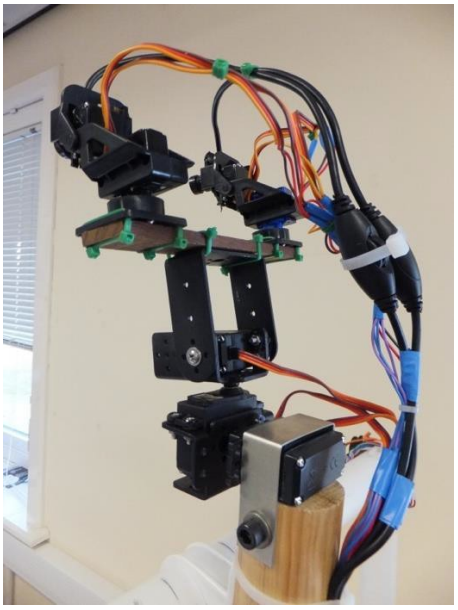

Figure 3.5 The servomotor actuated robot.

The servomotors are devices that have their rotational position set by supplying them with pulses of varying widths. They normally have a rotational range of 180°, with the controlling pulses ranging from 1ms (0°) to 2ms (180°) in period. These motors proved to be unsuitable for meeting the aim of the thesis in producing realist head gestures, due to their non-biomimetic mode of operation. That is, they offer rotation about an axis, rather than being by use of agonist and antagonist pairs.

3.3.2 First experiment with biological structure and actuation

The initial design with biomimetic actuation was based on using both PAMs and servomotors for actuation, and a full size plastic replica human skeleton was used as the framework, as shown in figure 3.6.

Figure 3.6 First experiment with biological structure and actuation

In this figure it can be seen that this robot used pneumatic air muscles (PAMs) in agonist/antagonist pairs as the major actuators for moving the head. The red cables in the diagram are steel wires within a red plastic sheath, which were sprung and connected to the arms of servomotors within the torso, as shown in figure 3.7.

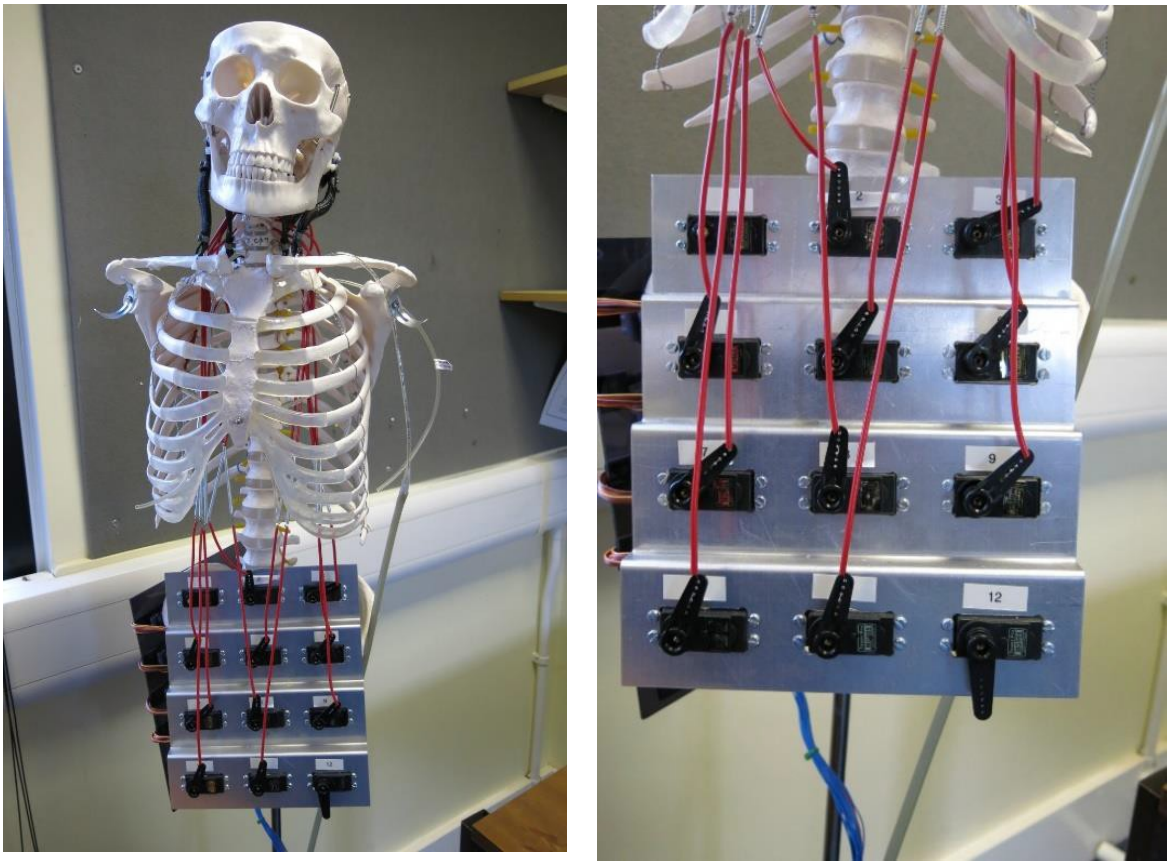

Figure 3.7 Servomotors on robot.

These wires were connected to the individual vertebrae of the cervical spine, and were designed to simulate the actions of the small muscles that support the neck in the human body. Much as the design of this robot was more biomimetic in principle and action than the previous one. It was found though that the system was far too complex to control efficiently, and was very prone to lock-up. This was due to the fact that all seven vertebrae were involved, and control of them needed more complex coordination. Additionally, the operation of the servomotors and the red control wires added negligible movement to the robot. Finally, there was a structural problem in supporting the weight of the head. For these reasons, it was decided to refine the design approach.

3.4 The final design

Following the experiences with the earlier versions it was decided to use air muscles for actuation due to their biomimetic operation, and also to simplify the neck into just 3 vertebrae, which were not individually controlled, yet still allowed non-rotational, lateral

translations to be made. It also solved the problem of supporting the weight of the head on the structure.

This ultimately led to the development of 'Eddie', a novel musculoskeletal humanoid neck (Figure 3.8). Its topology consists of four interconnected wooden vertebrae using ball-and-socket joints which anatomically simulate the structure of the principal kinematic segments in the human neck. Its actuation is biologically inspired by the activity of the four main pair of muscles governing the motion of human necks, and relies on eight custom-made pneumatic artificial muscles (PAMs) whose arrangement closely models the human neck muscular system. Thus far, this has not (to the author's knowledge) been done, even in state of the art applications of PAMs.

Figure 3.8 Eddie.

3.4.1 Mechanical design

The design of the robotic neck consists of four major parts: spine mechanism, muscular arrangement, sensory system, and electronic control system. The following sections describe the different mechanical units of the head.

3.4.2 Cervical Spine

Eddie's cervical spine consists of four stacked and interconnected wooden vertebrae as shown in figure 3.9. As explained earlier, this approach was taken as it simplifies the control problems, whilst still allowing for non-rotational, linear translations, in addition to the usual yaw, pitch and roll movements.

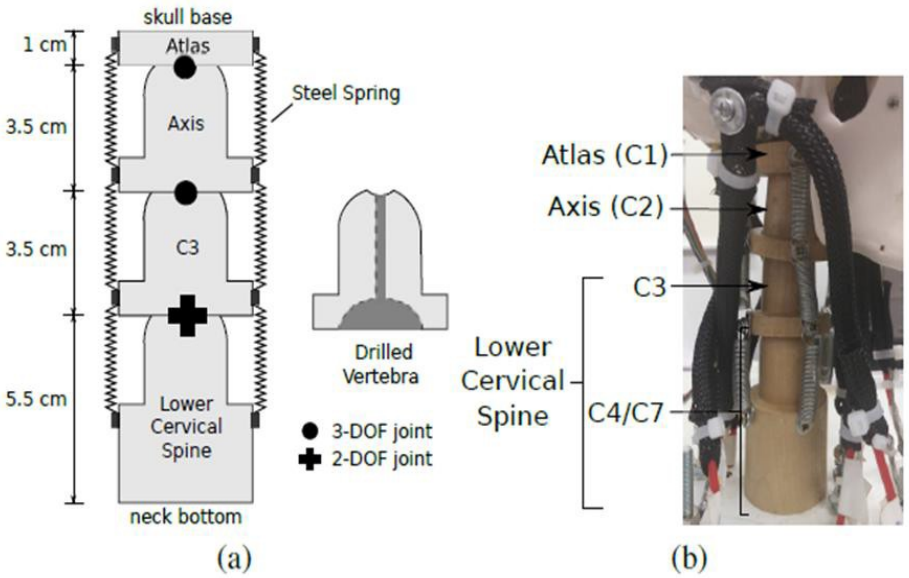

Figure 3.9 Eddie's Cervical Spine

They are connected using ball-and-socket joints (a compact 3-DOF joint). The uppermost vertebrae imitates the Atlas bone. It has a disk shape and is firmly attached to the plastic skull. Its base has a concave socket which cradles the second vertebra. The second and third vertebra have a similar cylindrical design with a superior convex surface and a larger cylindrical base with a concave surface. These vertebrae represent the Axis and C3 vertebra respectively. The last wooden vertebrae represents the C4-7 vertebrae. It has a longer shape, its superior end has a convex upper surface that cradles the wooden C3, and its bottom end is attached to a rectangular- shaped surface which acts as the upper thorax. The wooden vertebrae C3 and C4/7 constitute the lower cervical spine in the design. The length of the designed cervical spine is 13.5 cm which approximately matches the average length of the cervical part of the spine in a male.

All vertebrae have a central hole for an extensible support to pass through them and link them together, whist allowing movement, and each pair of vertebrae is also connected by four steel springs separated 90° apart. These springs mimic the action of the intertrasverse and interspinous ligaments, which in biology limit the flexion of the neck but allows its flexibility. This skeletal neck architecture enables the skull to be bent forward (pitch), tilted (roll), and rotated (yaw), whilst also allowing non-rotational linear translations to be performed.

3.4.3 Motion of the Cervical Spine

This work only considers four different pairs of muscles in the design of the robotic neck (see Figure 3.10), as biological studies have shown that these are the primary drivers of head motion (Dutia, 1991) and should there be sufficient to emulate its normal range of motions. To reiterate from the literature review, neck muscles normally operate in antagonistic pairs located at opposite sides of the cervical vertebrae. These muscles are:

- The Splenius Capitis muscles which are located at the back of the neck (Figure 3.10(a)). They connect the base of the skull with the upper thorax causing the head to rotate and bend towards either side. These muscles are antagonist to the Sternocleidomostoid muscles in the rotation of the head.
- The Longissimus Capitis muscles which are both at the back side of the neck (Figure 3.10(b)). They originate from the superior thoracic vertebrae and are attached to the mastoid process bone. These extend the head, and laterally flexes and rotates by the same amount. This pair of muscles are antagonist to Longus Colli muscles in the flexion of the head.
- The Sternocleidomastoid muscles which are located at the front side of the neck and connect the mastoid bone with the sternum and clavicle (Figure 3.10(c)). They are responsible for the rotation of the head and neck.
- The Longus Colli muscles which are situated in the frontal side of the neck, between the Atlas and the upper-most thoracic vertebrae (Figure 3.10(d)). They are responsible for the cervical flexion, ipsilateral side flexion and cervical rotation. These muscles also have a postural function.

(a) Splenius Capitis

(b) Longissimus Capitis

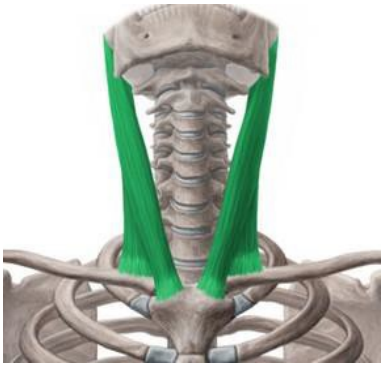

(c) Sternocleidomastoid

(d) Longus Colli

Figure 3.10 Neck muscles inspiring the design of Eddie (Kenhub.com, 2016).

3.5 Bio-inspired actuation of the neck

The muscular system of the humanoid neck is powered using eight custom-made standard PAMs (Figure 3.11). Each consists of an internal bladder surrounded by a braided mesh with nylon fibre that is flexible and non-extensive. One end of the bladder is closed and a tube for the air supply is attached to the other end. The lower-end of each actuator is connected to a wing-nut-based extensor mechanism located on the surface of the rectangular-shaped upper thorax, while the upper-end is connected to the plastic skull using brackets. Both the wing-nuts and brackets hold the PAMs in position within the neck and were designed to be the anchor points against which PAMs could exert a contractile force. The position of each of the PAMs corresponds closely to the arrangement of the human muscles described earlier. This was done by using measurements from the literature regarding the anchor points of the muscles in humans and replicating these on the robot. The actuators pull the plastic skull in an antagonistic manner in order to produce the desired head movement. The length of the PAMs and neutral position of the head can be tailored by manually adjusting the extensor mechanism.

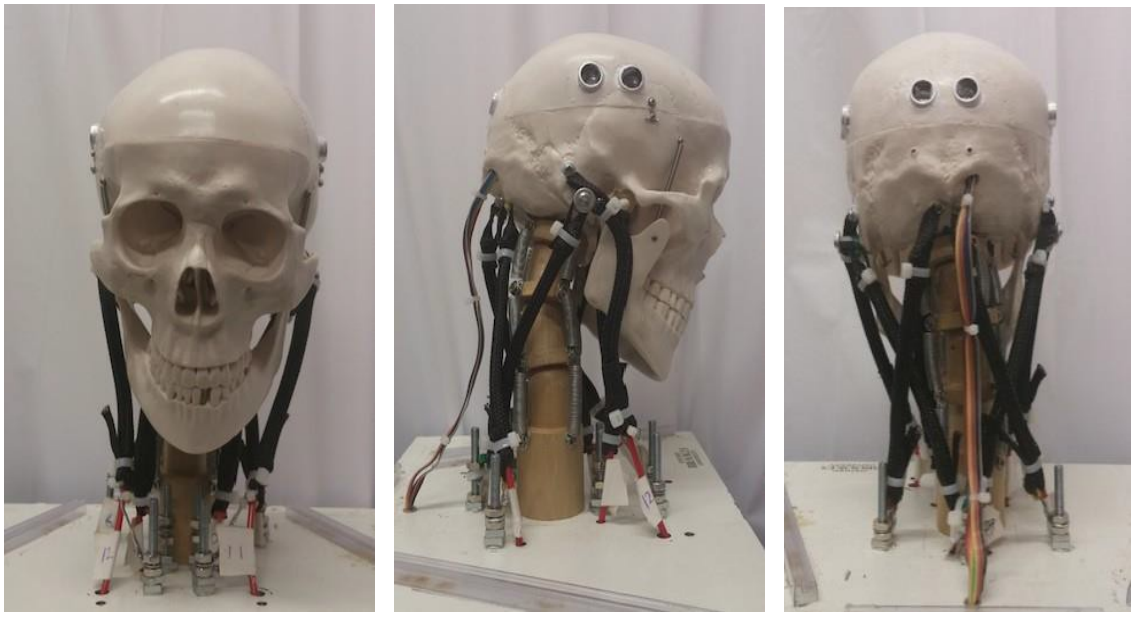

(a) (b) (c)

Figure 3.11 Frontal (a), Lateral (b) and Anterior (c) perspectives of Eddie.

The supply of air to the air muscles is controlled using proportional Festo VPPM proportional valves. Unlike traditional two-state switching regulators which only provide an on/off control, proportional air regulators allow the continuous variation of the air flow according to the level of an analogue control voltage. This reduces lunge and undesired shock movements, and also allows for precise positional control. Festo air regulators are compact and provide a maximum pressure of 10bar, that is comfortably beyond the

requirements for this platform. The PAMs were operated at a pressure of 4bar to prevent possible structural damage to the hardware whilst still providing enough pressure to produce the patterns of motion found in natural human necks, as was established later in experimentation. This is also within the normal operating pressures of 1 to 5 bar (Daerden and Lefeber (2002) for these devices. The PAMs being contractile actuators (as is biological muscle) could therefore be used in almost any biomimetic robotic application where the movement is based on the cooperative operation of agonistic/antagonist pairs.

The technical specifications of the proposed humanoid neck are summarised in Table 3.2. The design choices leading to these specifications will be described in the following sections.

Table 3.2 Hardware specifications of Eddie

Neck Height	13.5 cm
Neck/Head Weight	3.5 kg
DOF	8
Muscles(Actuators)	Total 8: 2 X Splenius Capitis PAMs (~170 mm) 2 X Longissimus Capitis PAMs (≈ 170 mm) 2 X Sternocleidomastoid PAMs (≈ 170 mm) 2 X Longus Colli PAMS (~ 150 mm)
Controller	Arduino Mega2650 16Mhz
Air Valve	8 Proportional Festo VPPM
Air Source	External Air Compressor
Operation Range	4bar max
Sensors	3 Ultrasonic sensors HC-SR04 1 Gyro + Acceleration sensor 6-DOF MPU6050 8 pressure transmitters (one per Festo valve)

3.6 Agonist/antagonist muscle pairs

PAMs are contractile devices operated by pressurised air (Daerden and Lefeber, 2002). When inflated, they bulge and shorten, as do biological muscles, and therefore generate a one-directional extensional force. PAMs are usually paired following an agonist/antagonist setup in order to generate a restoring movement. Although this kind of coupling is normally avoided by conventional actuators, it presents several benefits in the design of

anthropomorphic robots (Davis and Caldwell, 2001), such as flexibility, coordination in the mechanical linkage of joints and compliant behaviour. The design of this robot takes advantage of these factors, along with a biomimetic arrangement to generate full-neck simple movements comparable to the human neck, which are the aim of this thesis.

3.7 Control

The neck is controlled by the commercially available Arudino Mega2650 16MHz microcontroller, which is able to drive up to 16 actuators by generating independent PWM signals. These PWM signals are then passed through a low pass filter, which converts them to true analogue signals in the range 0V to 5V. These signals are then passed to a non-inverting voltage amplifier with a gain of 2, thus bringing the signal amplitude up to the 0V to 10V range. This voltage is then used to control the Festo proportional valves over their full pressure range. The accelerometer/gyroscope is connected to the Arduino using an I2C data bus, whilst the ultrasonic sensors are connected directly to the digital input/output pins of the Arduino board. Figure 3.12 provides a block diagram illustrating the overall electronics system of the humanoid neck.

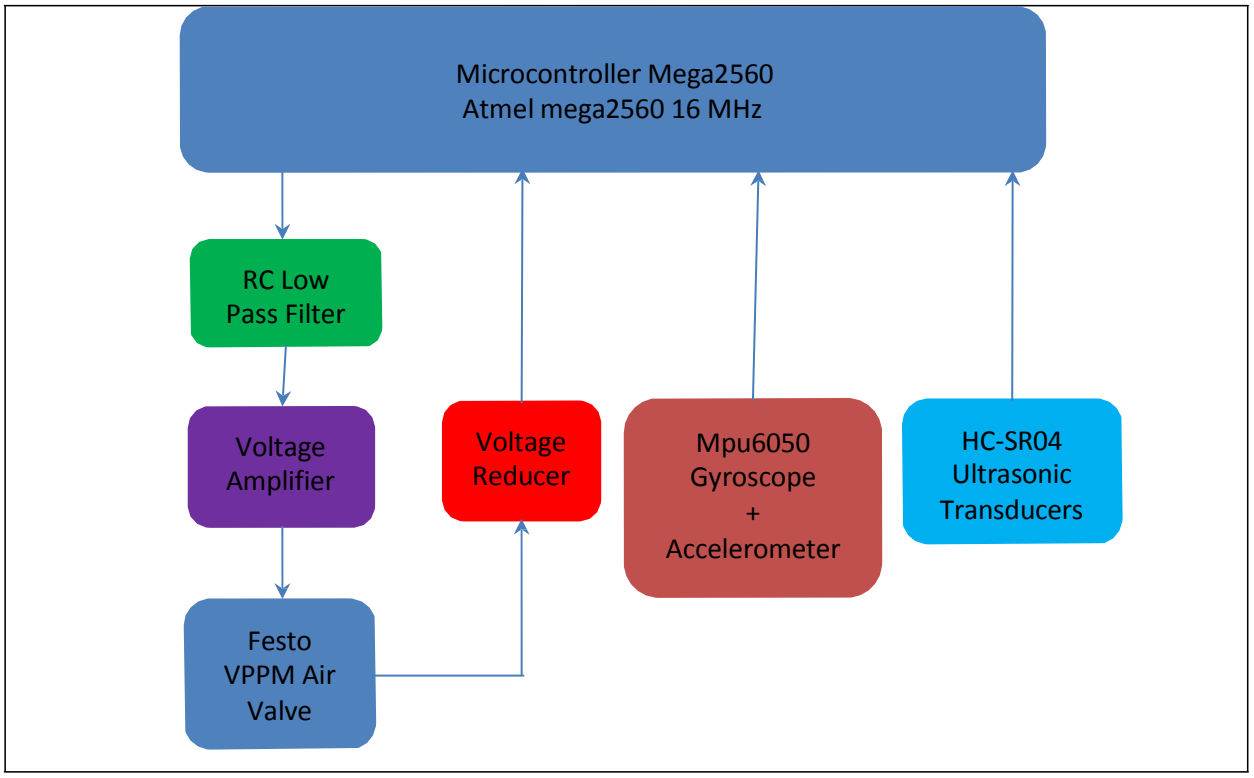

Figure 3.12 The electronic and air control system with the associated sensors

3.8 Sensors

The proposed neck is endowed with three standard ultrasonic sensors HC-SR04, which reflect from a plastic surround, one 6-DOF gyroscope and accelerometer MPU6050 (Figure 3.13), and 8 pressure transmitters, one for each air muscle. The ultrasonic sensors are located at the back and on each side of the plastic skull as shown if figure 3.13. The

gyroscope/accelerometer is placed at the centre of the head inside the skull. The pressure transmitters form part of the FESTO proportional valves. They provide real-time information of the flow pressure and regulate it to compensate for any fluctuations, for instance, due to the antagonist 'stretching' due to the contraction of an opposing air muscle.

A plastic surround encloses the plastic skull laterally and from behind and is designed to reflect the ultrasonic signals. It is composed of three flat plastic surfaces, each sloped 20° vertically and 10° horizontally to enable the detection of the orientation of the head (Hitchin, 2000). The sloped are sufficient to detect the accurate positioning of the robotic head. The plastic surround is separated 10 cm laterally and 15 cm from behind the skull.

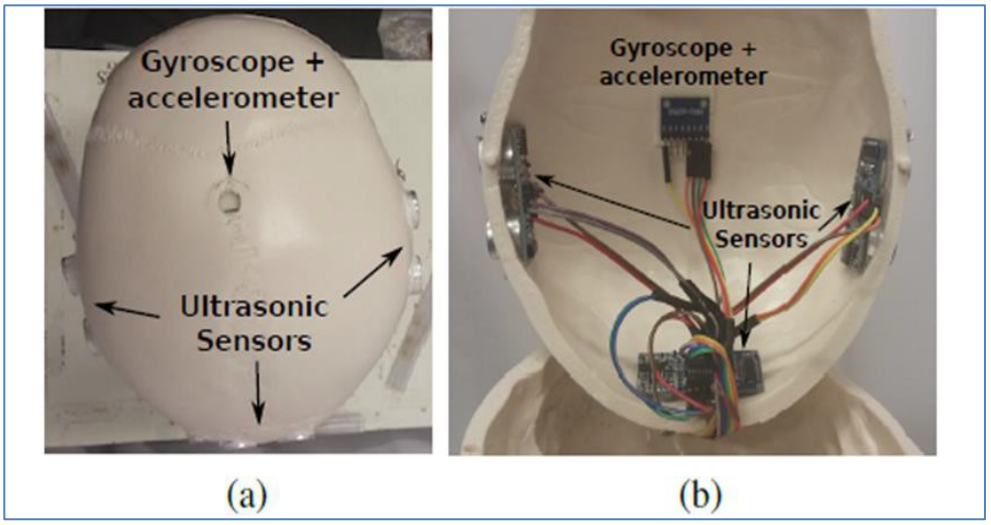

Figure 3.13 Superior (a) and inferior (b) views of the sensors in Eddie's plastic skull.

3.8.1 Ultrasonic sensors reflector shield

The ultrasonic sensors (HC-SR04) use sonar to determine distance between the surface of the skull and the plastic enclosure that surrounds the head as shown in figure 3.14. The major use of these is to determine a 'home' or datum/absolute position of the head on system startup, but in this design they were also used to establish the validity of the data from the accelerometers and gyroscopes, as unlike accelerometers, they are not susceptible to drift. As the ultrasonic sensors are essentially echo location devices, they do need a reflective surface with which to bounce of the sound. As they will be used to establish the datum position of the head, and also be used as a comparison for the accelerometer/gyroscope data, it was essential to enclose them within a fixed and rigid reflective enclosure.

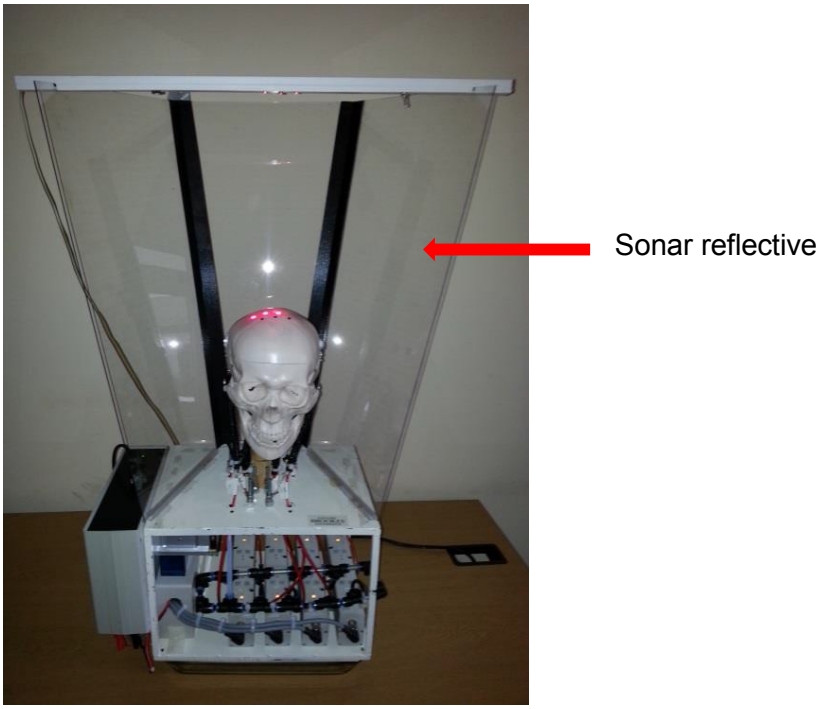

Figure 3.14 Sonar reflective enclosure.

The enclosure was originally designed with perpendicular sides, as shown in figure 3.15.

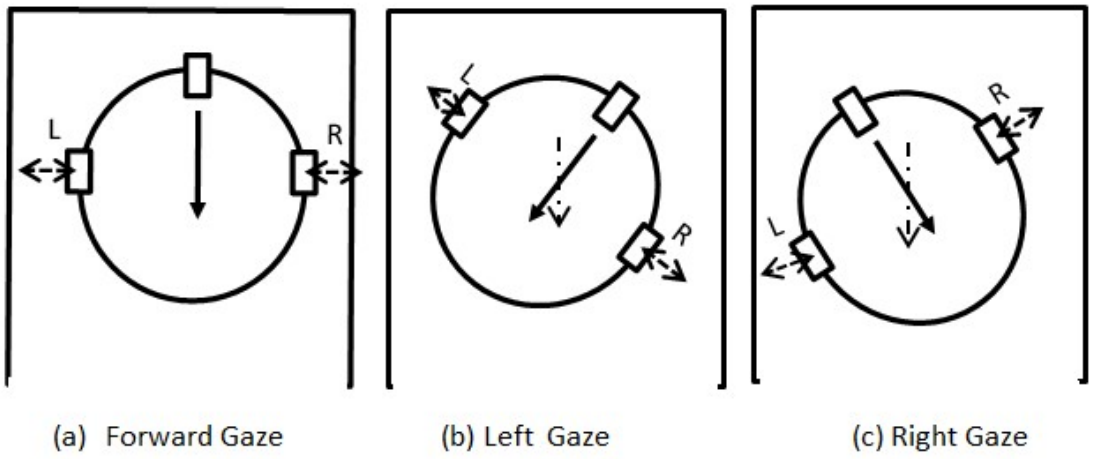

Figure 3.15 Plan views of the original sonar location system.

As can be seen, the figure shows a plan view of the head and reflective surfaces. When noting the path length for the left (L) and right (R) sensors, it can be seen that when considering head rotations in a left-right gaze directions, the left and right path lengths are always equal. As the diagram illustrates, this is true whether the head is gazing forward (a), left (b) or right (c). This means that it is impossible to measure the rotational angle using this arrangement, although the forward gaze (a) position could be sensed by establishing the shortest possible paths. Similarly, for the same reasons it is impossible to measure left/right roll, as shown below in figure 3.16.

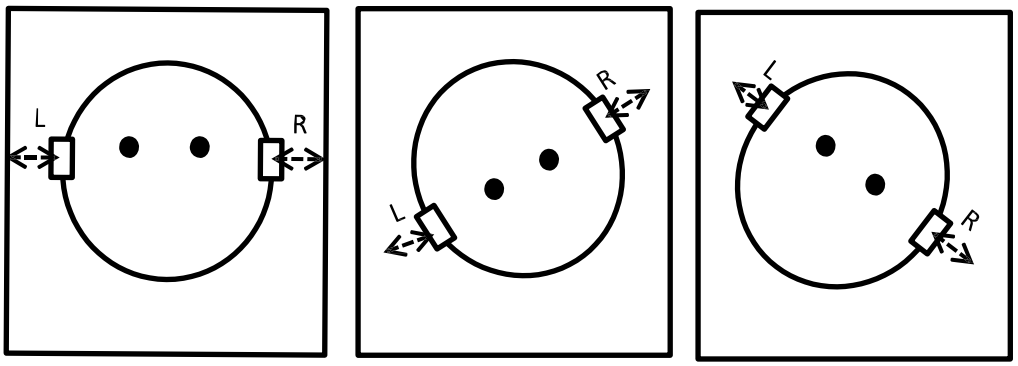

(a) Level (b) Roll Left (c) Roll Right

Figure 3.16 Front views of the original sonar location system

Looking at figure 3.17 which shows a side view of the head, as in the previous situation, the level (a) position could be sensed by establishing the shortest possible paths. It is, however, impossible to detect whether the head is gazing upwards or downwards using perpendicular reflectors and the sonar unit fitted to the back of the head, as again, the paths could be the same length.

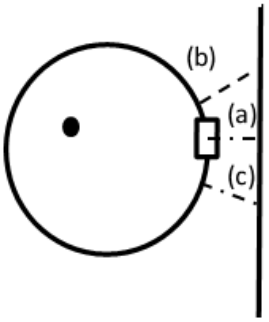

(a) Gaze Forward
(b) Gaze Down
(a) Gaze Up

Figure 3.17 Side view of the original sonar location system

To eliminate these issues, the sonar reflector was built with sloping sides. This is shown is figure 3.18. The reflectors are sloped 20° vertically and 10° horizontally to enable the detection of unambiguous head positions (Hitchin, 2000). These slope values have been determined as sufficient to accurately detect the position of the robotic head.

Figure 3.18 Sloping sonar reflectors

Figure 3.19 shows plan views of the final arrangement of the sonar reflectors.

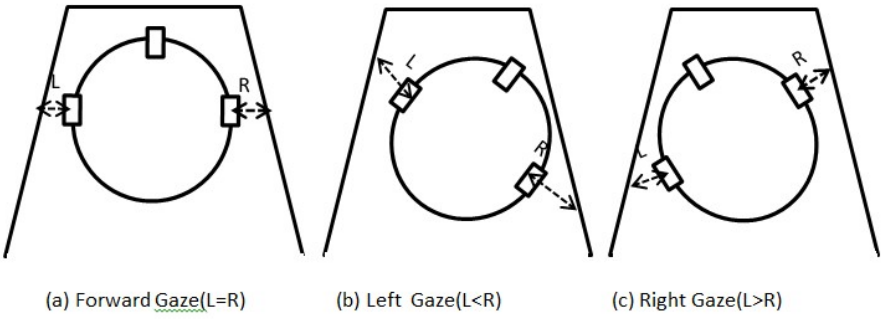

Figure 3.19 Plan views of the final sonar arrangement.

As in the previous case, when the head gazes forward (a) paths L and R are of equal length. However, with the new arrangement of sloping reflectors, it can be seen that when the head gazes left (b), path L will always be shorter than path R. Conversely, when the head gazes right (c), path L will always be longer than path R. Thus, this arrangement thus allows for an unequivocal detection of whether that head is gazing forwards, left or right.

Figure 3.20 shows the front view of the sonar arrangement.

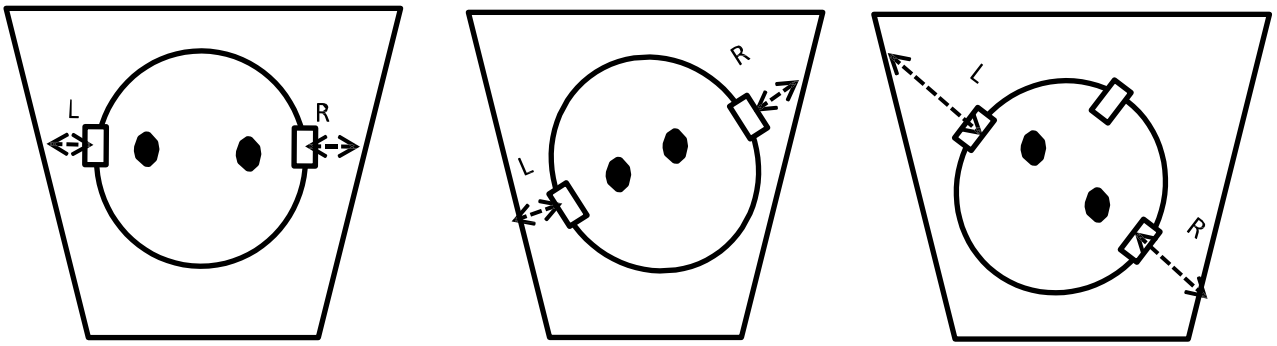

(a) Level (L=R) (b) Roll Left (L<R) (c) Roll Right (L>R)

Figure 3.20 Front view of the sonar arrangement.

Once again, in the neutral (level) position (a), paths L and R are of equal length. When the head rolls to the left (b), path L is shorter than path R, whereas a roll to the right (c) will result in path L being longer than path R.

Finally, figure 3.21 shows a side view of the reflector arrangement, illustrating the various path lengths for the rear sonar sensor. Path (a) is the gaze forward path. As can be seen, as the gaze lifts (c), the path shortens, when the gaze lowers (b) the path lengthens, thus there is no ambiguity regarding position.

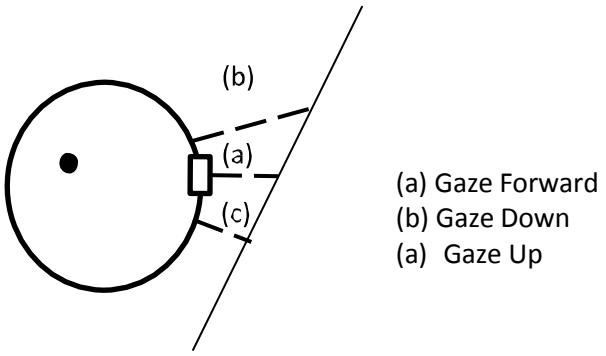

Figure 3.21 Side view of the final sonar arrangement

3.8.2 Ultrasonic transducers

When evaluating various sensors for establishing the datum position of the head and also checking the validity of the data from the accelerators and gyroscopes, a number of options were explored before it was decided to use ultrasonic sensors. These were chosen as they are not subject to any kind of drift. Additionally, their accuracy, with a maximum error of 3mm over their maximum usable range of 4m was more than sufficient, as in this application, the maximum range was around 10cm, thus giving a maximum error of less than 0.1mm.

The first alternative to the ultrasonic sensors to be considered were infra-red proximity sensors, which operate on the basis of measuring distance to a target by means of an infra-red light emitting diode (LED) and photoreceptor. The infra-red (IR) light from the LED is

transmitted with no direct path to the photo-receptor. The only way that the IR light can fall on the receptor is when it is reflected from a target. This principle is shown in figure 3.22.

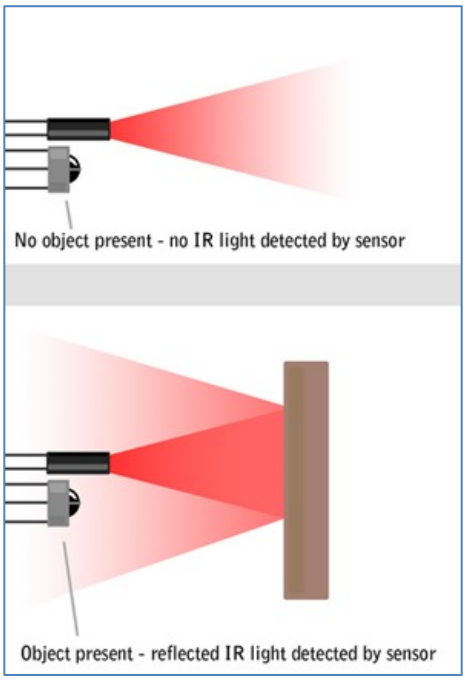

Figure 3.22 Operating principle of infra-red proximity sensors.

As can be seen, when there is no target present, no IR light falls on the IR sensor. However, when the light hits a target, it is reflected back and falls upon the sensor. The sensor changes resistance according to the light intensity hitting it, hence, the distance to the target. The closer the target, the higher the intensity of light. A typical one, the Sharp GP2Y0A21YK0F can measure in the 10 to 80cm range (Sharp.com, 2017) These can be very accurate in detecting levels of reflected light, and outputs a signal in either analogue or digital format depending on the particular variant used. There is a problem, however, in that the reflected light level is not solely dependent upon distance to the target. It is also dependent upon the colour and reflective properties of the target. An additional problem is that the sensor can be affected by ambient IR light from other sources. For these reasons, it was decided not to use this type of sensor.

Another option for optically establishing the position of the head was to use a laser distance measuring device. These sensors are not affected by the reflective properties of the target, in that they sense distance based upon the time that a signal takes to return rather than its intensity, as is shown if figure 3.23.

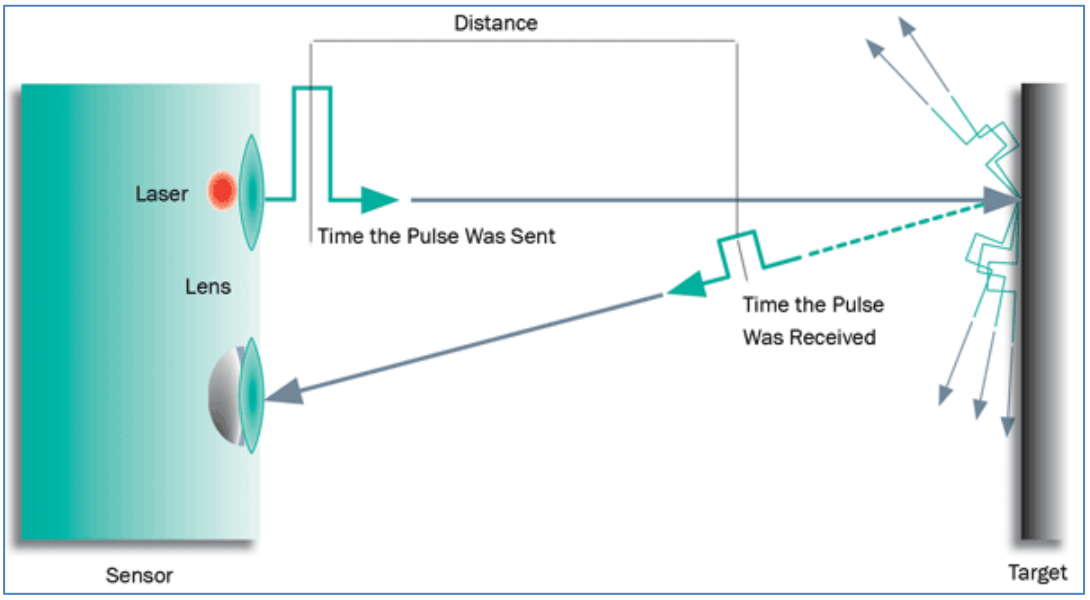

Figure 3.23 Operating principle of laser proximity detectors (machinedesign.com, 2017).

These sensors therefore seemed to provide ideal functionality, but their cost was prohibitive, therefore, it was decided to use ultrasonic (sonar) sensors, as they are considerably cheaper, whilst providing the levels of accuracy required. The datasheet (micropik.com, 2017) states an error of no more than 3 millimetres over a 4 metre range.

The sonar sensors used in the robot are HC-SR04 ultrasonic ranging modules. The receive/transmit pair is shown in figure 3.24.

Figure 3.24 HC-SR04 Ultrasonic ranging module.

The datasheet (micropik.com, 2017) states that to operate the unit and start the ranging, a +5V (TTL High) 10uS pulse is sent to the trigger pin, which causes the unit to send out an 8 cycle burst of 40KHz ultrasound, and then switch to listen mode. The echo from the target is received, and the distance to the target can be calculated from the time taken from the trigger signal to receipt of the echo, as shown below in figure 3.25.

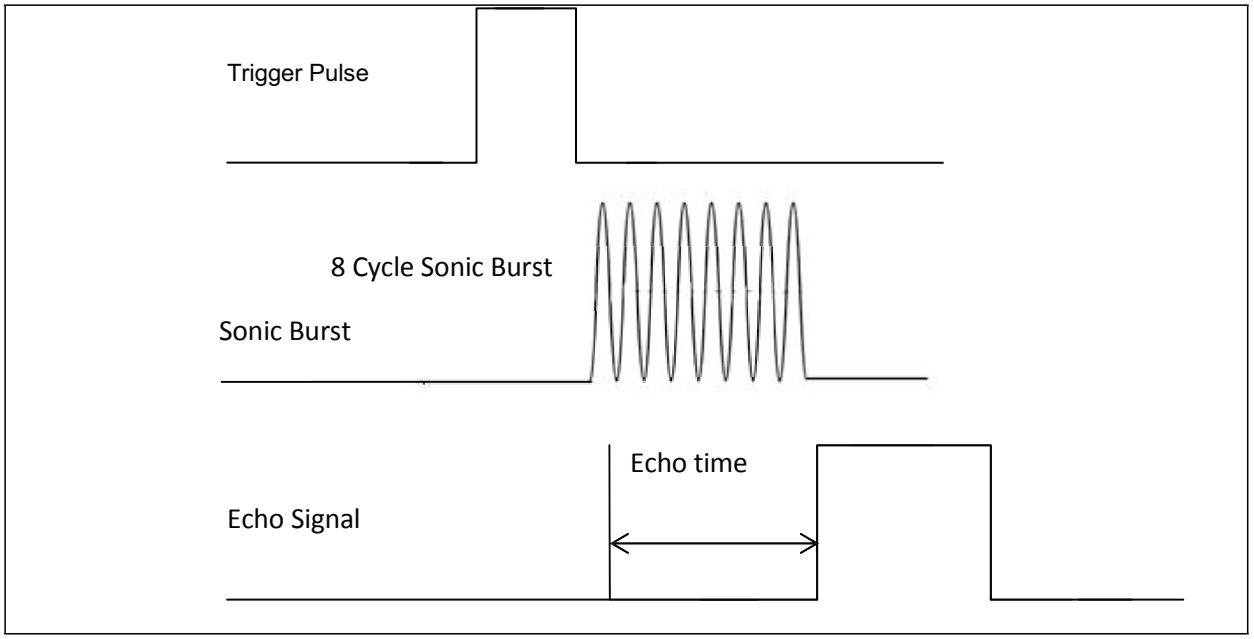

Figure 3.25 HC-SR04 timing diagram.

The formulas stated in the datasheet to calculate the distance from the ultrasonic transducer to a reflector in inches and centimetres, and based on echo time are shown below. The manufacturers claim a maximum error of 3mm over their maximum usable range of 4m. The method for establishing distance is shown in equation (1).

$$\text{Distance in cm} = mS/58;\ \text{Distance in inches} = mS/148 \qquad (1)$$

The trigger and echo signals of the HC-SR04s were connected to the digital pins of the main controller (an Arduino Mega 2560) as shown in figure 3.26.

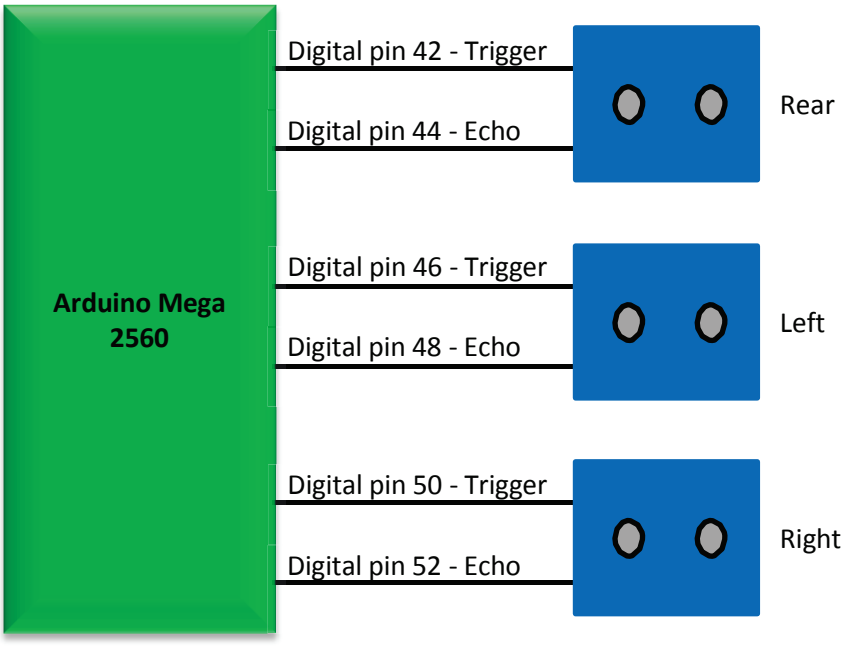

Figure 3.26 Connections between ultrasonic transducers and main controller board

3.8.3 Gyroscope/accelerometer

The gyroscope/accelerometer fitted to the robot is the Invensense MPU6050 built onto a GY521 breakout board, and an extract from the datasheet can be seen in Appendix A1. This particular board was chosen, as it offers a 6-axis gyroscope and accelerometer all on one chip. Additionally, there are prewritten software libraries available for it in the Arduino IDE, thus simplifying programming. As can be seen in figure 3.27, the orientation of the X and Y planes were shown on the board. The Z plane can be envisaged as an on-page rotation about the large chip in the centre of the board.

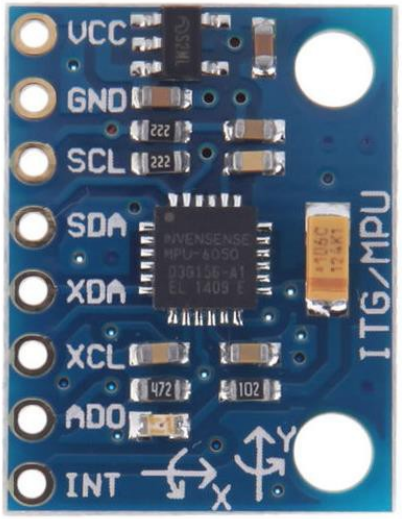

Figure 3.27 GY521 board with an MPU6050 6 Axis Gyroscope and Accelerometer.

The unit comprises an embedded 3 axis micro-electromechanical systems (MEMS) gyroscope, a 3 axis MEMS accelerometer, and a digital motion processor (DMP™) hardware accelerator engine. Although the sensors are actually analogue devices, the data is from them is passed though analogue to digital converters (ADCs), before being fed out of the chip via an I^2C serial interface using the SDA (serial data) and SDC (serial clock) pins. A block diagram in shown in figure 3.28.

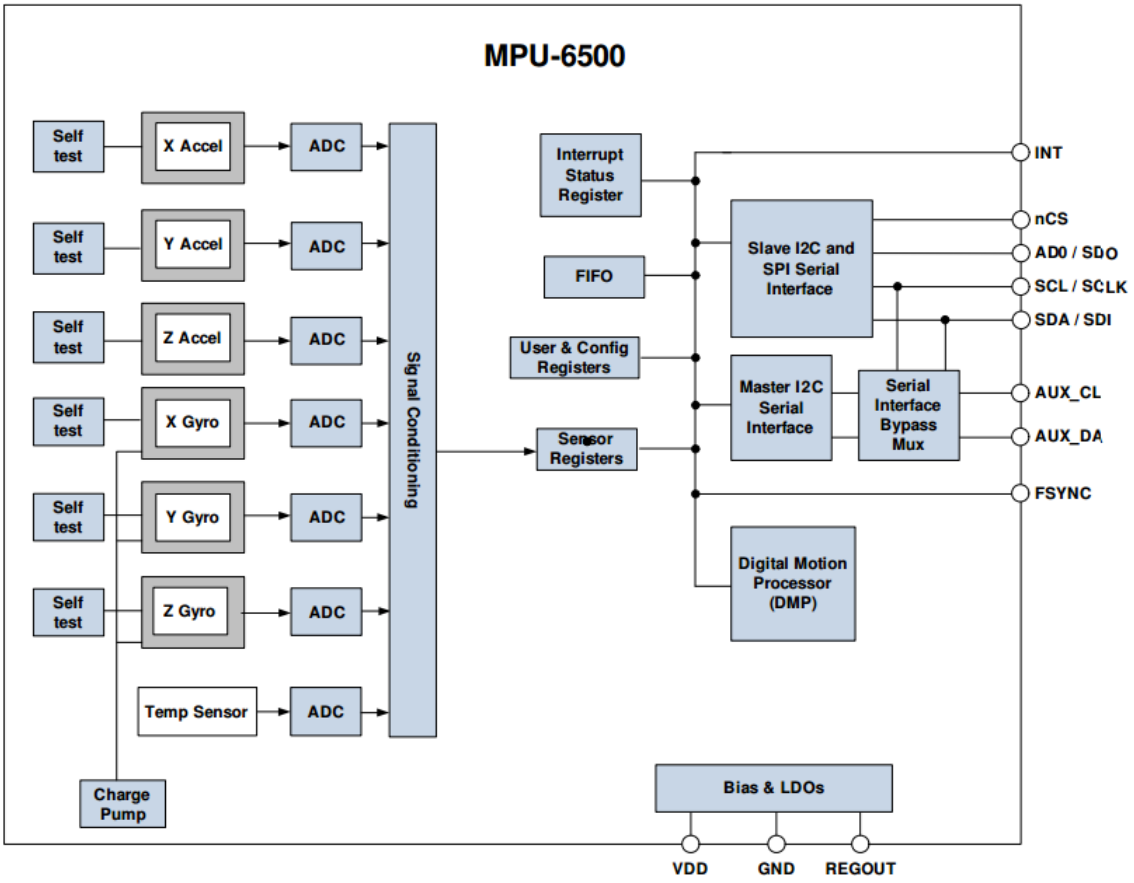

Figure 3.28 MPU6050 block diagram (invensense.com, 2016).

The device consists of three accelerometers, providing X, Y and Z acceleration data in the user-programmable full-scale ranges of ±2g, ±4g, ±8g, and ±16g. The outputs from these are fed into 16 bit analogue to digital converters (ADCs) for digitising these signals. These acceleration data were also used to gather velocity data through a process of intergration. Similarly, the three X, Y and Z gyroscopes feed into 16 bit ADCs. This arrangement allows simultaneous sampling of all the accelerations and angular velocities. After digitisation, the signal is passed though user-programmable filters in the signal conditioning block, which can be used to remove low frequency noise, before being fed into the sensor registers, and ultimately, out through the I^2C interface. The digital motion processor which supports 3D motion processing and gesture recognition algorithms was used in this application to filter out the drift which is inherent in accelerometers.

3.9 The main controller board

An Arduino Mega 2560 was chosen as the main controller after consideration of several other options. A field programmable gate array (FPGA) was considered, as its architecture provides for true parallel (rather than sequential) processing, thus providing higher processing speeds. It was, however, rejected as it did not have the required analogue inputs and outputs, which were needed for the air muscle pressure monitoring and actuation, and additionally, it required considerably more time spent on low level programming. A number of

more 'conventional' microprocessor chips were considered, but these required quite a lot of external circuity to support them, which would have bought about delays through design, simulation, prototype testing and manufacture. For this reason, these were also ruled out.

For the reasons above, it was decided that the best option was to use an 'embedded' controller, that is, a microprocessor and associated support circuitry on a ready-made, commercially available board. After some investigation, it became apparent that Arduino boards were the best option. This was because they have the required digital and analogue inputs and outputs, and they are comparatively easy to program using the Arduino programming environment and its supporting libraries.

As the final design for the robot used a large number of electrical signals, it was decided that out of the Arduino range, an Arduino Mega 2560 was the best option due to its large number (54) of input/output pins. The Arduino Mega 2560 is shown in figure 3.29. The major signal connections are labelled on the board.

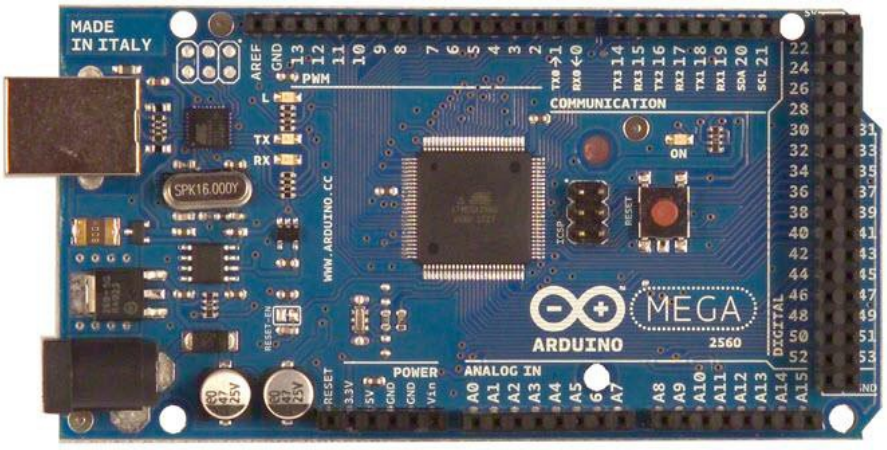

Figure 3.29 Arduino Mega 2560 (arduino.cc, 2016(b)).

Figure 3.30 shows a more detailed view of the pinout allocations.

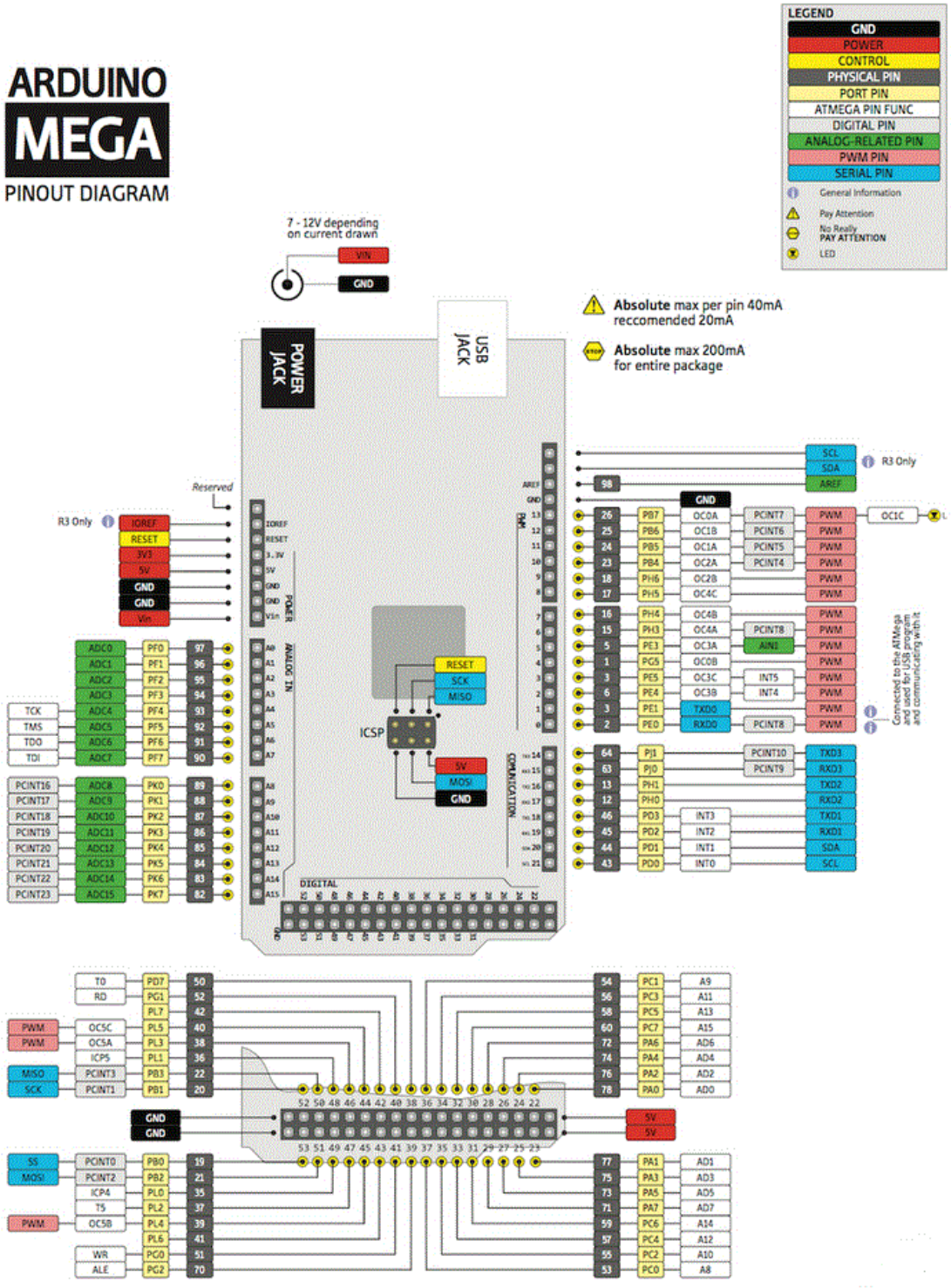

Figure 3.30 Arduino Mega 2560 pinouts (ibid).

As can be seen, it has 54 digital input/output pins, 14 of which can be used a pulse width modulation (PWM) outputs (for later conversion to true analogue for PAM control), 16 analogue inputs (used for reading the air muscle pressures), and it also has I^2C communication using pins 20(SDA) and 21(SCL) which are used for communication with the accelerometer/gyroscope. The technical specifications of the board are given below in table 3.3.

As can be seen, the board is based around an Atmel2560 8 bit microcontroller with 256KB of in-system self-programmable flash memory with read/write capabilities.

Table 3.3 Arduino Mega2560 Technical Specifications (arduino.cc, 2015(b)).

Microcontroller	ATmega2560
Operating Voltage	5V
Input Voltage (recommended)	7-12V
Input Voltage (limit)	6-20V
Digital I/O Pins	54 (of which 15 provide PWM output)
Analogue Input Pins	16
DC Current per I/O Pin	20 mA
DC Current for 3.3V Pin	50 mA
Flash Memory	256 KB of which 8 KB used by bootloader
SRAM	8 KB
EEPROM	4 KB
Clock Speed	16 MHz
Length	101.52 mm
Width	53.3 mm
Weight	37 g

As mentioned previously, one of the reasons that this board was chosen was because of its ability to accept analogue voltage inputs – in this case, the pressure level signals from the air muscles, measured by the Festo proportional valves. The analogue inputs each pass into an analogue to digital converter which provides 10 bit resolution *(ie*, 1024 different values). By default, they measure between ground (0V) up to 5V. It is possible to change the upper end of the range using the AREF pin, but this was not necessary in this application.

The PWM (pulse width modulation) outputs are used to drive the proportional valves that control the air flow into and out of the air muscles. The PWM outputs have an 8 bit resolution (*ie*, 256 different values/levels). The proportional valves need 'true' analogue signals in the 0-10V range, rather than (5V) PWM ones, and for this reason some signal processing was necessary to convert the PWM to true analogue, and then boost it up to the appropriate levels.

3.9.1 Programming the Arduino board

All Arduino boards are programmed through use of the Arduino Integrated Development Environment (Arduino IDE), which is a cross-platform system written in Java, and is a derivative of the Processing programming language and the Wiring projects. Programs are written in C or C++, and the Arduino IDE comes with a software library called 'Wiring', which is from the original Wiring project, and makes many common input and output operations simpler to use. It consists of a text editor for writing code, a text console, a toolbar with buttons for the common functions, and a series of menus. As one of the original aims of Arduino was to make embedded programming accessible to artists and musicians (Arduino.cc, 2015(b)), the programs are called sketches. The Arduino IDE is shown in figure. 3.31.

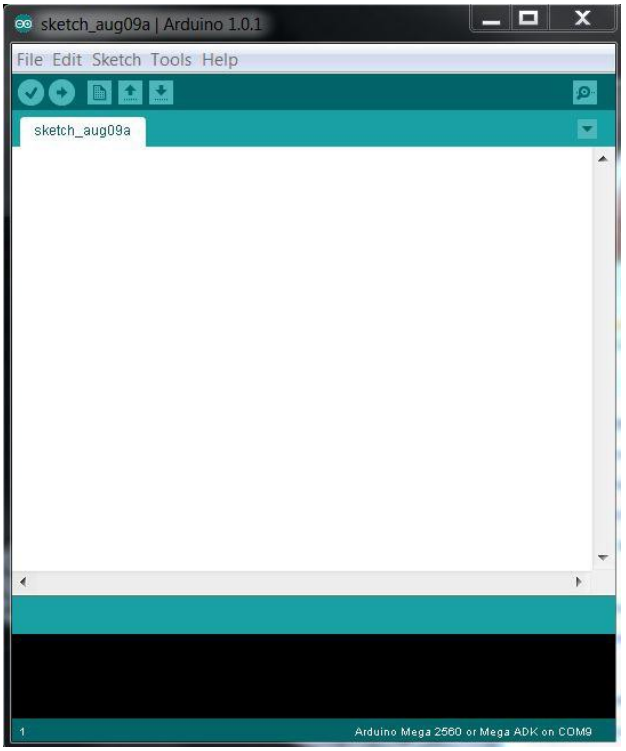

Figure 3.31 The Arduino IDE (*ibid*).

The main programs are written in the Editor window. The upload sketch button (with the arrow pointing to the right) checks the program for syntax errors (which would be listed in the error console – the black area at the bottom), before compiling (converting to binary machine code) and uploading to the board. Once uploaded, the programs begin to run automatically, and will loop until the board is powered off.

3.10 Filter and amplifier

As stated earlier, the proportional valves require a 0V to 10V true analogue control voltage, whilst the Arduino board only outputs 5V PWM signals. PWM is a representation of analogue values, created by varying the duty cycle of a digital signal, as shown in figure 3.32.

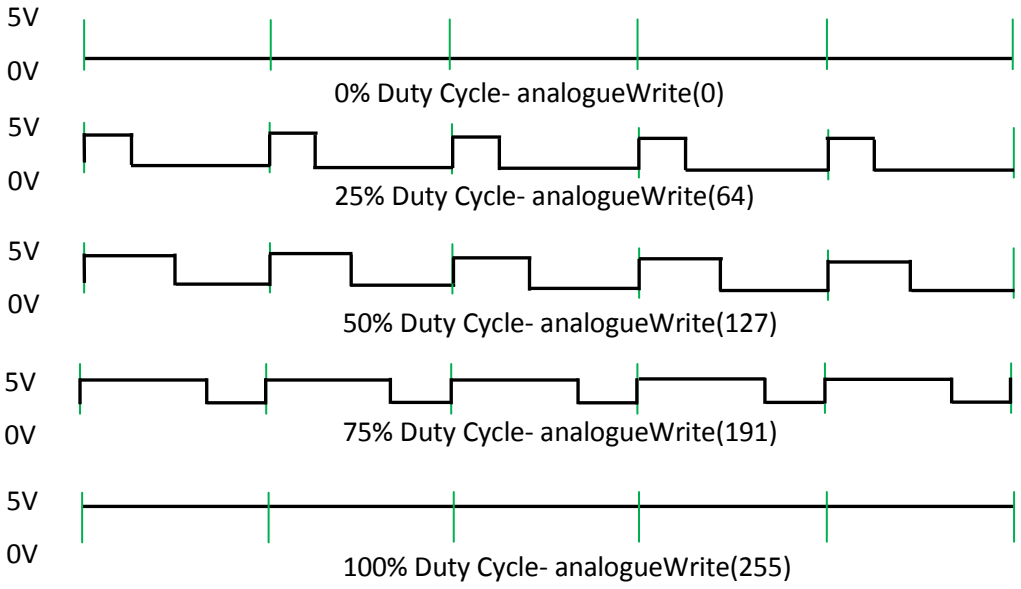

Figure 3.32 PWM using an Arduino board (Arduino.cc, 2015(b)).

In figure 3.32, the regular time periods shown by the green lines are 2ms apart, meaning that the Arduino's PWM frequency is 500Hz. The PWM output is accessed through use of the 'analogueWrite()' command, which operates on a 0 to 255 scale, where analogueWrite(0) calls for a 0% duty cycle (always off), analogueWrite(255) calls for 100% duty cycle (always on), and, for instance, analogueWrite(127) would give a 50% duty cycle (equal on and off periods).

In order to convert these on-off 5V pulses to true analogue, it is necessary to filter out the 500Hz frequency component, and smooth the resultant signal. Finally, it this then necessary to boost the signal level from a 0V to 5V level to a 0V to 10V level.

To achieve the filtering and smoothing, a capacitor/resistor (CR) low-pass filter was used. This is a passive filter, and hence has no gain, but this is not an issue, as a voltage amplifier is used after the filter to multiply the voltage to the right level. The amplifier circuit needed to provide a gain of 2, to take the signal levels from 5V to 10V, and needed to be non-inverting. The design was based around the TL074 quad operational amplifier (opamp). The pinout is shown in figure 3.333. More details can be seen in Appendix A2, and the full datasheet can be found at ti.com (2016).

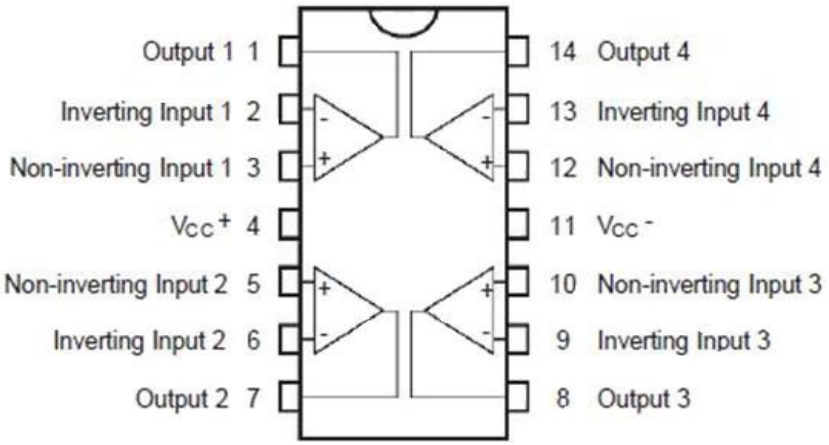

Figure 3.33 TL074 quad opamp pinout (ibid)

The TL074 was chosen as it was tolerant of the voltages involved, and came in a quad package. This was very useful, as eight copies of the filter/amplifier circuit had to be made to control the eight proportional valves, and each circuit used one opamp. Hence, the circuit could be constructed using just two TL074s. The absolute maximum ratings of the TL074 are shown in table 3.4.

Table 3.4 TL074 absolute maximum electrical ratings (from datasheet extract in appendix A2).

	MAX
Supply Voltage	18V
Differential Input Voltage	30V
Input Voltage	15V
Duration Of Output Short Circuit	Unlimited

The input voltages fed to the circuit were the 5V PWM signals from the Arduino, so this falls easily within the 15V limit. In order to have headroom for the 10V desired output, that is, not saturate the amplifier, it was decided to run it off a 12V supply, which again, easily falls in the 18V limit. The original circuit design of the filter and amplifier is shown in figure 3.34.

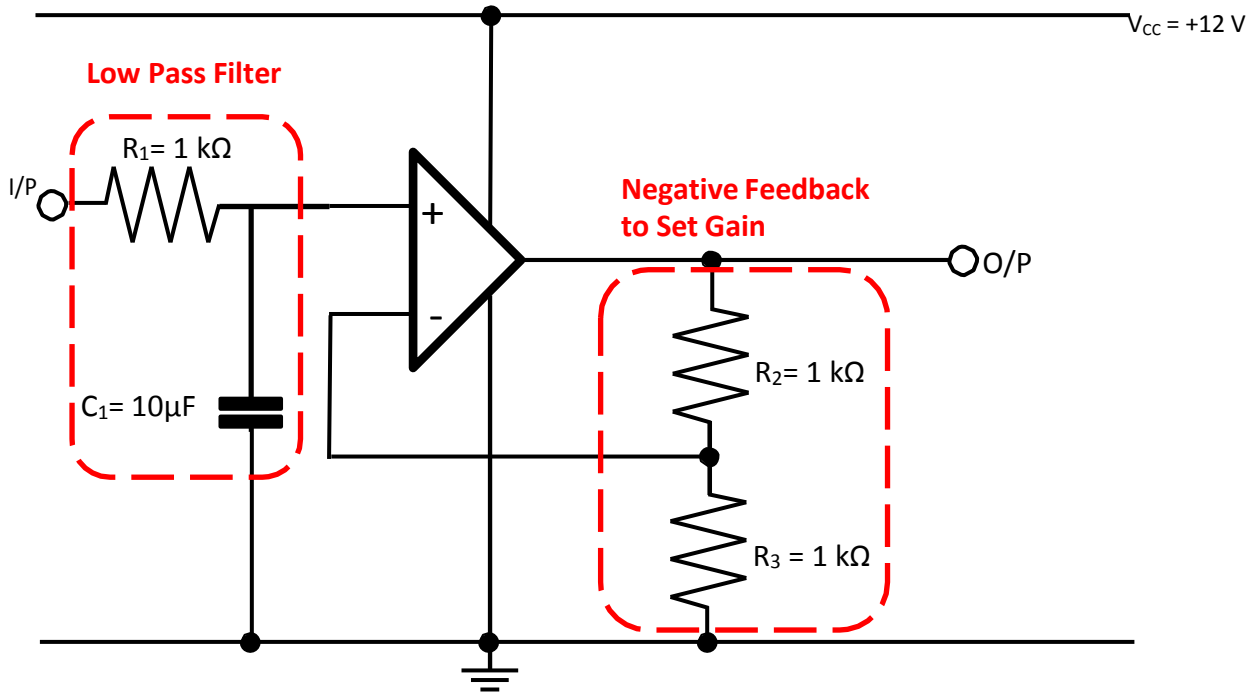

Figure 3.34 Initial filter and amplifier design.

As can be seen, the circuit consists of a first order low-pass filter formed by C1 and R1, followed by a non-inverting gain stage formed by the operational amplifier, R2 and R3. Negative feedback is derived from the potential divider formed by R2 and R3, and this was used to set the gain of the amplifier.

In the filter circuit, the cut off frequency (the frequency at which the filter attenuates the input power by half (or 3dB) is determined by the time-constant (τ)) as shown in equation (2).

$$f_c = \frac{1}{2\pi\tau} = \frac{1}{2\pi RC} \qquad (2)$$

Substituting the values for R1 and C1 into the above equation gives equation (3).

$$f_c = \frac{1}{2\pi \times 1\times 10^{3} \times 10\times 10^{-6}} = 1.59Hz \qquad (3)$$

This is reflected in the bode plot in figure 3.35.

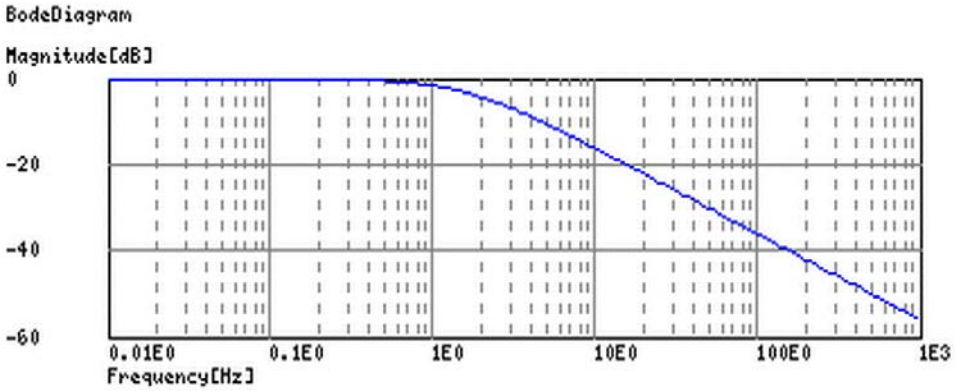

Figure 3.35 Bode plot of CR first order low-pass filter.

The resultant cut off frequency of around 1.5Hz means that the 500Hz switching component of the PWM signal is filtered out, whilst allowing for sufficiently quick variations in the resulting filtered (analogue) signal to control the air muscles at the required speeds.

Following the CR low pass filter is the amplification stage of the opamp with its gain controlling resistors R2 and R3. In this case, the amplifier is required to step up the voltage swings from 0 to 5V, to 0 to 10V. Thus, this gives a voltage gain requirement of 2, as demonstrated in equation (4).

$$\text{Voltage gain} = \frac{V_{out}}{V_{in}} = \frac{10}{5} = 2 \qquad (4)$$

In this configuration of a non-inverting op-amp circuit, the voltage gain is given by equation (5).

$$\text{Voltage gain} = 1 + \frac{R_2}{R_3} = 2 \qquad (5)$$

Therefore (equation (6))

$$\frac{R_2}{R_3} = 2 - 1 = 1 \qquad (6)$$

Meaning that for a gain of 2, R2 = R3. The value is not critical, as long as they are equal.

3.10.1 Performance of the initial circuit

Whilst the circuit design and component calculations did provide the necessary filtering and gain characteristics (on paper), when tested, it was found that the output voltage never went above 5V. The individual parts of the circuits were tested with a function generator – and worked according to theory, but when connected to the PWM output of the Arduino board the circuit still would not operate according to the desired specifications.

After further testing, it was realised that the problem was due to using a single-ended supply (just +12V and 0V). This meant that the output could only respond in one direction,

whilst losing the opposite half-cycle – hence the voltage only moved by half the desired amount.

3.10.2 The improved circuit design

The solution to this problem was to operate the amplifier and filter circuit on a split supply, as shown in figure 3.36. The input and output are referenced to an independent ground at 0V.

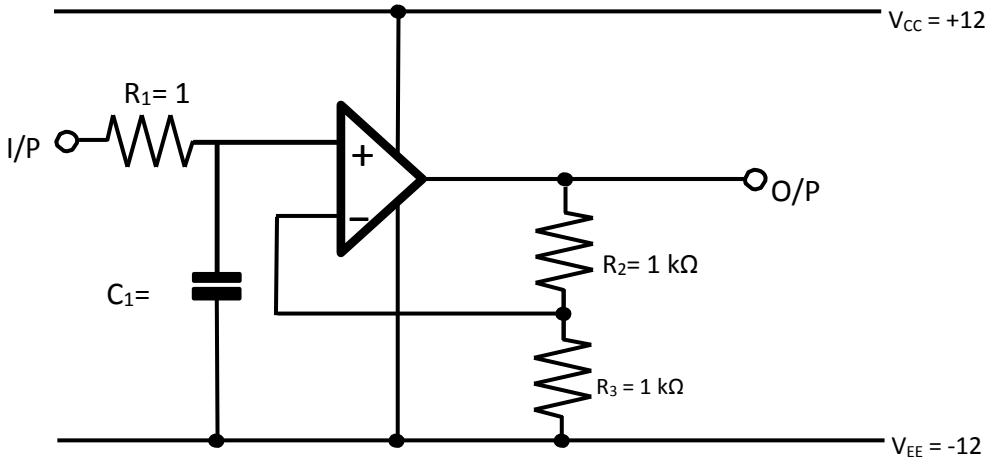

Figure 3.36 Final design for the filter and amplifier.

As is shown, the circuit now operates with supplies of +12 and -12V with respect to ground. When the circuit with this power configuration was tested, it performed fully to specification, with the output voltage swinging over the full range 0V to 10V as the duty cycle of the input varied from 0% to 100%.

As mentioned earlier, the analogue inputs of the Arduino controller are used to monitor the pressure in the PAMs. This is a feature that will be used in future work on machine learning, and was not used for the purposes of this thesis. This pressure signal is supplied by the proportional valves, in the range 0 to 10V representing 0bar to 10bar pressure. Also as was stated earlier, the Arduino analogue input returns values in the 0 to 1024 ranges for voltages in the 0 to 5V range. This means that the analogue signal from the proportional has to be reduced by a factor of 2. This was done by means of a simple potential divider, as shown in figure. 3.37.

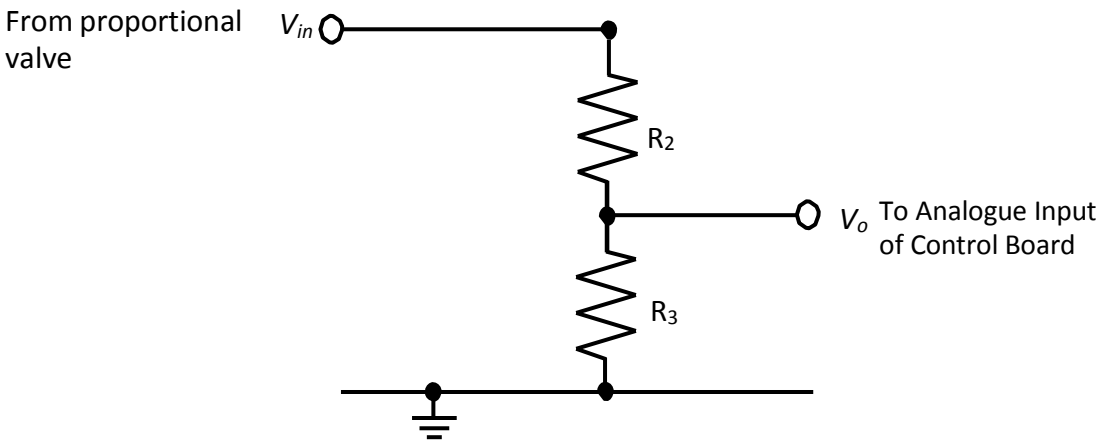

Figure 3.37 Potential divider.

The circuit shown is a classic potential divider where the output voltage across R2 is given by equation (7)

$$V_0 = V_{in}\left(\frac{R_2}{R_1 + R_2}\right) \qquad (7)$$

Hence, if R1 = R2, as equation (8) shows

$$V_0 = V_{in}\left(\frac{R}{2R}\right) = \frac{V_{in}}{2} \qquad (8)$$

Thus reducing the voltage range from 0 to 10V down to 0 to 5V.

The actual resistor values are only important insofar as they do not draw excessive current from the source of $V_{in,}$ so for this reason, they were set at 10kΩ.

All the electronic circuitry was built on stripboard. Figure 3.38 shows the Arduino controller, filter, amplifier and potential divider as fitted to the robot.

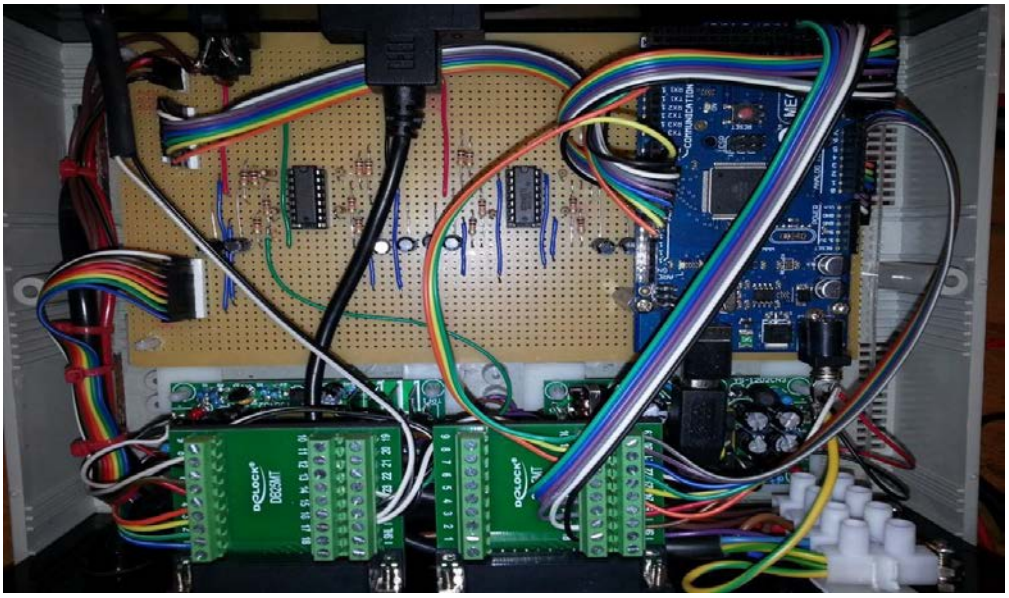

Figure 3.38 Arduino controller, filter and amplifier.

3.11 Proportional valves

Now having achieved a true analogue voltage from the control circuitry, this was applied to the Festo proportional valves in order to control the air pressure in the PAM's. These valves allow for a 0bar to 10bar pressure control, though use of a 0V to 10V DC control voltage. To preserve the life of the PAMs and minimise the chance of air leaks, the pressure was limited to 4bar, as through experimentation this was found to be enough for the actuation of the robot.

The front and rear view of the supply air system on the robot are shown in figure 3.39.

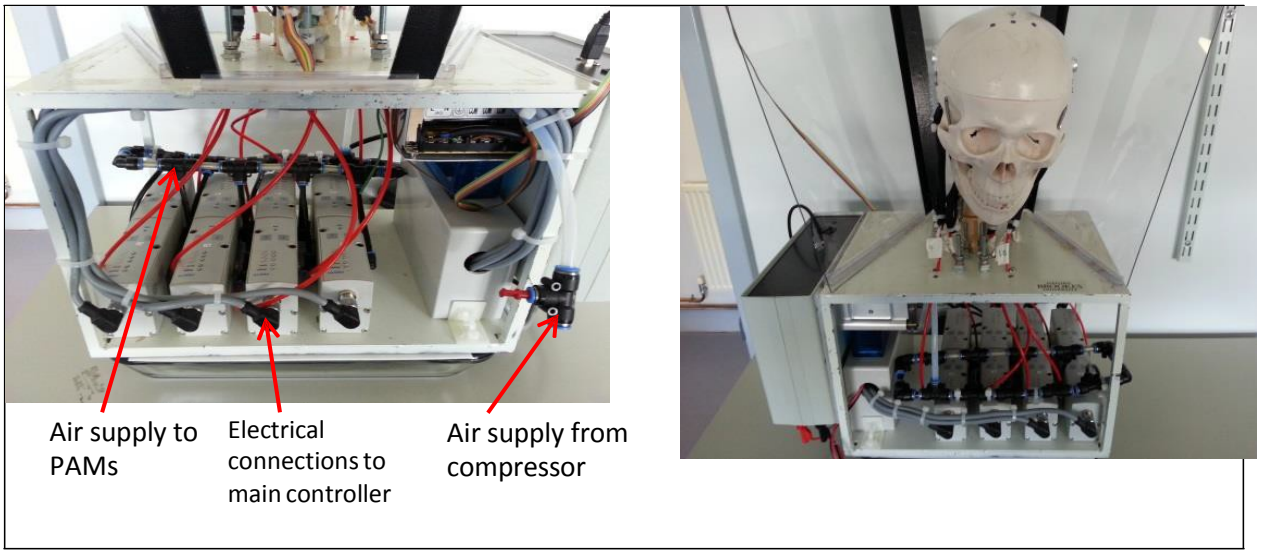

Figure 3.39 Air supply and control system rear (left) and front (right) views.

These diagrams show the 8 proportional valves as physically situated in the robot. As can be seen, air is fed from the compressor into a single manifold shown on the right of the rear view. This air supply is taken to all the proportional valves in parallel, and the outputs taken to the individual PAMs, as shown in figure. 3.40.

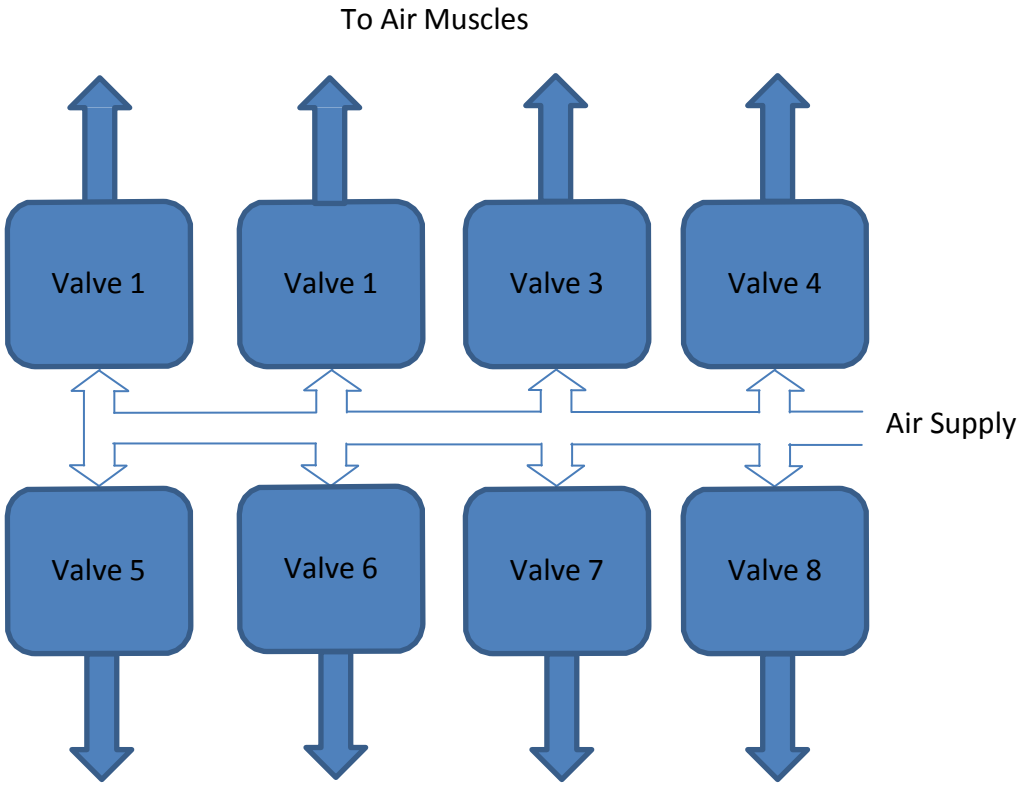

Figure 3.40 Schematic of air supply and control system

3.12 Summary

This chapter discussed the design and implementation of the robot, along with the rationales behind the various design decisions. The discussion covered all the varying aspects of the design, including mechanical, pneumatic and electronic systems, and the integration of all these. As can be seen, there were a few problems with the original design ideas, but rather than being seen as a set-back, these diversions very much helped to inform the design process and much was learnt from them.

As will be seen in the next chapter, not all the features built into the robot were used in the evaluation for the purposes off this thesis, namely the pressure monitoring system. This is fully completed and working according to specifications, and will be used in future work into machine learning. However, all the positional sensory systems were used.

CHAPTER 4

EVALUTION OF ROBOT ANGULAR SPEEDS AND RANGES, AND EMOTIONAL ACCEPTABILITY

4.1 Introduction

The chapter presents the experimental work carried out on the robot to see how its performance compared to the benchmarks set out in chapter 3, as well as an analysis and discussion of the results obtained. It also presents the testing carried out to establish the emotional acceptance of the robot to human participants. Thus, the objective of the experiments were to gather both objective (using all the sensors) and subjective (using humans) data regarding the movements of the head.

The first tests carried out were designed to establish the velocities and rotational ranges of the head in terms of Roll (head tilt – X axis), Pitch (head nod – Y axis), and Yaw (head rotate – Z axis), because, as mentioned in chapter 2, there are no measurements in the literature for non-rotational lateral movements, although, as mentioned earlier, it was necessary to assess the capability to perform non-rotational lateral movement during the Nod and Tilt movements. These movements were explained in chapter 3, and are reiterated below in figure 4.1. and 4.2. Also as mentioned earlier, the yaw, pitch and roll axis shown in figure 4.1 are for definition only, and do not take into account the fact that the neck also moves during head movements.

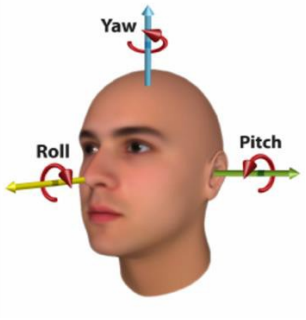

Figure 4.1 Human head roll, pitch and yaw (Arcoverde *et al.,* 2014. P.281).

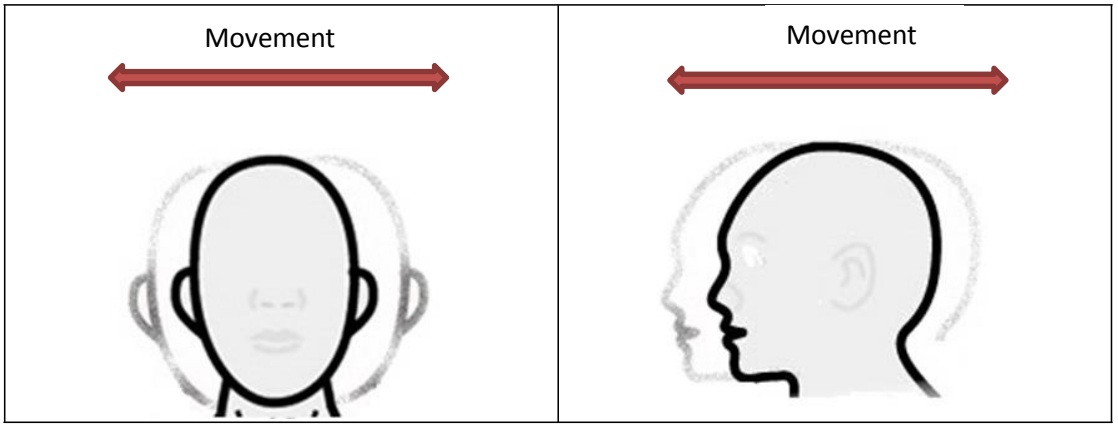

Figure 4.2 Non-rotational, linear translations

The average ranges of movement for an adult male, which were seen as desired ranges are shown again in table 4.1 below.

Table 4.1 Average ranges of movement for and adult male (Fitzpatrick, 2010).

Total Nod	107°	<430°/Sec absolute maximum (involuntary) <100°/Sec (voluntary)
Total Tilt	90°	<360°/Sec absolute maximum (involuntary) <100°/Sec (voluntary)
Total Rotate	140°	<467°/Sec absolute maximum (involuntary) <100°/Sec (voluntary)

Also as discussed earlier neurological studies by Leigh and Zee (2015) show that under normal voluntary conditions angular head velocities do not exceed 100 deg/sec, so this figure was used as the comparison for the angular velocity for the various degrees of freedom for the neck.

The data provided by the positional and rotational measures from the MPU6050 gyroscope/accelerometer were used to firstly calibrate the head in an upward motionless resting position and secondly, to track the displacement. To calibrate the head position, it was manually set so that three markers on the head aligned with three laser beams projected from and overhead support. This method was used, as to use the ultrasonic sensors to achieve the same would have required the simultaneous reading of three distances from the three sensors on a computer screen. The laser arrangement is shown below in figure 4.3 and 4.4, which show an un-aligned head in order for both the laser dots and the markers on the head to be seen. This alignment was carried out to ensure that the head was always in the same position when the accelerators were being calibrated/compensated for drift at the start of each experimental run.

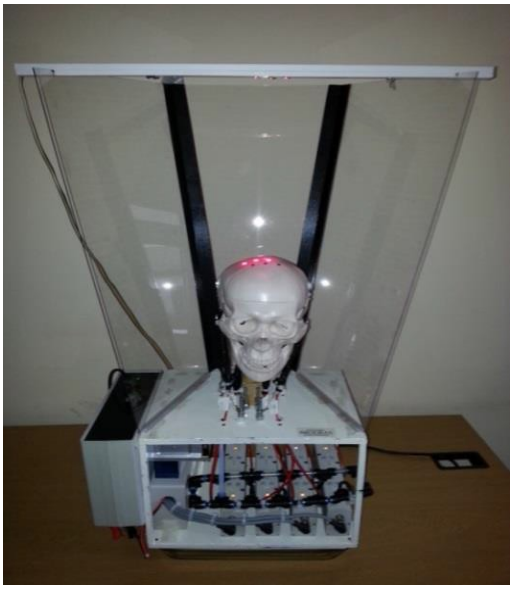

Figure 4.3 The arrangement of the head alignment lasers (front view).

Figure 4.4 The arrangement of the head alignment lasers (plan view).

Once the initial head position is calibrated, that is, the datum or absolute position established, the angular displacements and accelerations in three dimensions were measured by use of an MPU-6050 6-axis gyroscope/accelerometer, with the data from this being validated by the ultrasonic sensors connected to the main Arduino controller board. The MPU6050 gyroscope/accelerometer was located within the robot head as shown in figure 4.5.

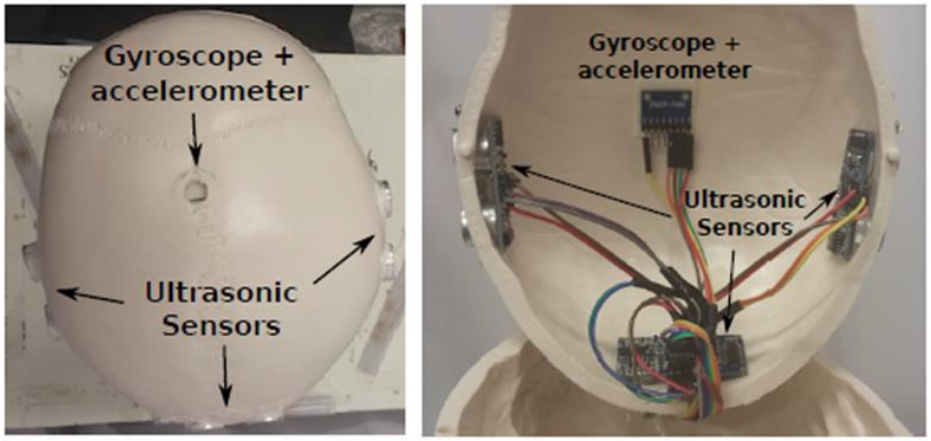

Figure 4.5 Gyroscope/accelerometer positioning.

4.2 Method

Firstly, the complete system was set up, and connected to a PC via the USB connection on the Arduino controller board. This allowed for programming of the head movements and also the collection of gyroscope and accelerometer data along with the data from the ultrasonic sensors. The data from these sensors were collected via RealTerm terminal software, and stored in text files for later analysis. The data from the accelerometers and gyroscopes were used to establish the physical position of the head by combined use of trigonometry and integration. To ensure that the measures taken to remove any drift affects from the accelerometer data were successful, these data were compared to the absolute data regarding the head distance from the ultrasonic enclosure using the ultrasonic sensors, and a statistical analysis of the repeatability of coincidence was undertaken. That is, when the accelerometers and gyroscopes show that the head is at (for instance) 'Point A' and an ultrasonic measurement is taken, is this ultrasonic measurement the same next time the accelerometers and gyroscopes indicate that the head is at 'Point A'. The velocities of the head were obtained by integrating the accelerations, and the displacements by integrating the velocities.

4.3 Statistical Analysis

The statistical analysis was undertaken using the IBM SPSS software package. It was first intended to use the p-value test, but this proved to be unsuitable, as the data did not fall into a normal distribution, which is a prerequisite for using this test (Field, 2015). After some research and discussion with the Head of Statistics at Oxford Brookes University, it was decided that the best approach was to use the Kendall rank correlation coefficient test, commonly known as Kendall's tau coefficient (*ibid*). This is a non-parametric hypothesis test, that is, it makes no assumptions about the probability distributions of the variables being tested – which was the problem the with p-value test. For hypothesis testing, it is used to

establish whether or not the two variables may be considered statistically associated. In this case, whether the data from the accelerometers and gyroscopes (corrected for drift) and the absolute (no drift) data from the ultrasonic sensors were statistically related – which would demonstrate the accelerometer drift correction was accurate, and therefore, that the measurements of the head movements were correct. If the agreement between the two rankings is perfect, the value returned is 1, and if there is a perfect disagreement, a value of -1 is returned, whereas a null hypothesis returns a value of 0. It is common practice to consider a relationship greater than 95% to be statistically significant (*ibid*), and this was the figure used in this testing. In addition to the Kendall's tau coefficient test, it was also decided to provide a 'double-check' of the statistical relationship using the Pearson product-movement correlation coefficient test, which again is a non-parametric test, but this time, it measures the linear correlation between two variables, where a total positive linear correlation returns a value of 1, a totally negative correlation returns a value of -1, whilst a value of 0 signifies no linear correlation.

4.4 Moving the Head

To undertake the measurements, the PAMs worked in agonist/antagonist pairs, with one side being fully inflated to produce maximum contraction, whilst the opposing ones were fully deflated. Unused PAMS were fully deflated. The pressure was controlled by an analogue DC voltage signal in the range of 0V (fully deflated) to 10V (100% pressure). This in turn was derived from a low-pass filter and amplifier circuit designed to take the 5V pulse width modulation outputs from the Arduino controller, and then smooth and amplify it to provide the required 0 to 10V control signal. The signals were taken from the Arduino digital pins, and were controlled by use of the analogueWrite function. This allows the 256 step control of the duty cycle of a pulse width modulated signal ranging from analogueWrite(0) – 0% duty cycle, to analogueWrite(255) – 100% duty cycle. The whole process is shown below in figure 4.6. This method was used in order to collect data on the maximum angular ranges and accelerations of the head. The air pressure fed to the PAMs was restricted to a maximum of 4bar to minimise the risk of air leaks. Greater contraction of the PAMs would have been obtained by allowing higher pressures, but experiments with higher pressures showed the tendency to develop leaks and so lower pressures were utilised to ensure durability. Also, 4bar was found by experimentation to be more than sufficient for the purpose. The PAMs were inflated and deflated by the use of proportional valves, which allowed an ‘analogue’ type control of the pressure – with a step-less control ranging from zero pressure to the maximum, as opposed to use of a ‘digital’ and more conventional on-off type valve.

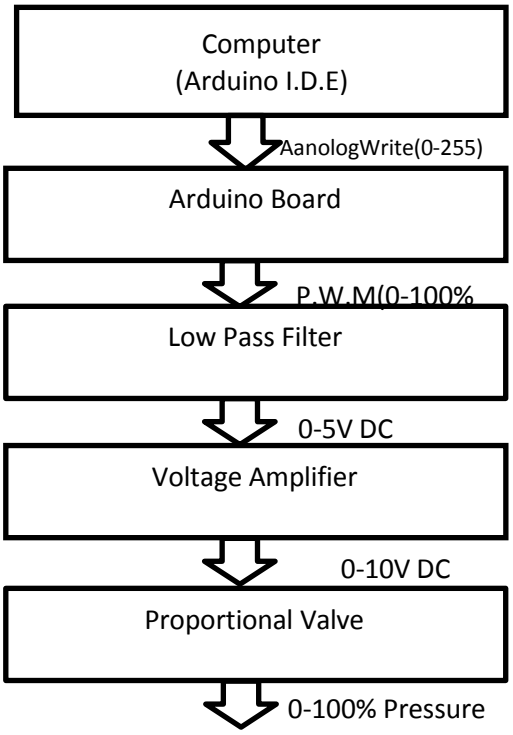

Figure 4.6 Control of the PAMs.

The tests were organised into three runs, Pitch (nod), Roll (tilt) and Yaw (rotate). For each test, the head was moved from one extreme to the other (one cycle), and this was repeated 20 times. When the head reached an extreme, the head paused for one second, to allow any bounce to settle. The Arduino code for reproducing these movements in given in Appendices A3, A4 and A5. As the aim of the thesis is to determine the capability for non-rotational linear translations and the maximum ranges of movement possible by the head, no attempt was made to utilise the same muscles as used in a biological neck for each movement. Rather, all the possible PAMs for each movement were used in order to establish the maximum angular ranges and velocities, given the comparatively low pressure at which they were operated. A plan view of the muscle layout is shown in figure 4.7 along with a list of the biological muscles that they represent.

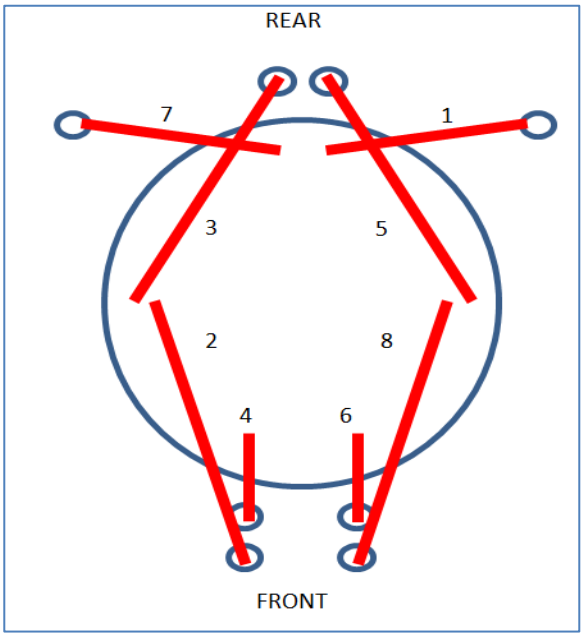

2 and 8 Sternocleidomastoid

4 and 6 Longus Colli

1 and 7 Longissimus Captis

3 and 5 Splenius Captis

Figure 4.7 Plan view of head showing the muscle layout.

4.5 Muscles used in the pitch, roll and yaw tests

4.5.1 Pitch test

To measure the maximum pitch (nod) range and velocity, the agonist/anatagonist muscle groups (in green and red) are shown in figure 4.8. As can be seen muscles 1, 3, 5 and 7 worked in opposition to muscles 2, 4, 6 and 8.

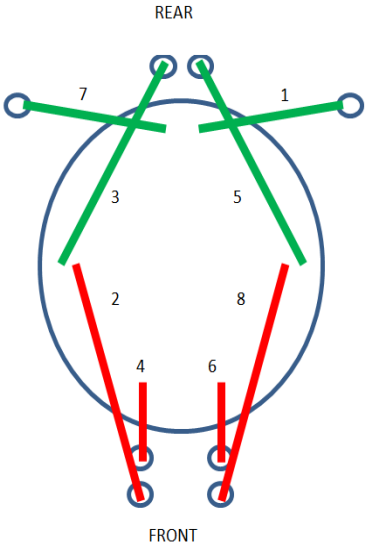

Figure 4.8 Agonist/antagonist pairs used in the pitch test.

4.5.2 Roll test

To measure the roll (tilt) ranges and velocities, the agonist/anatagonist muscles 2, 3, and 7 worked against muscles 1, 5, and 8 (in green and red) as shown in figure 4.9. Here it can be seen that the dotted lines for muscles 4 and 6 indicate that these were not energised for this movement.

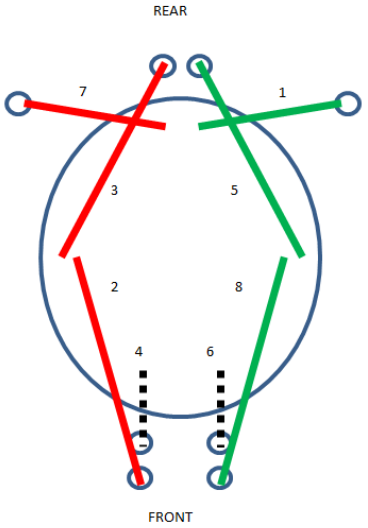

Figure 4.9 Agonist/antagonist pairs used in the roll test.

4.5.3 Yaw test

To measure the maximum yaw (rotate) ranges, the agonist/anatagonist muscles 1, 3, and 8 worked against muscles 2, 5, and 7 (in green and red) as shown in figure 4.10. As in the roll test, muscles 4 and 6 were not used.

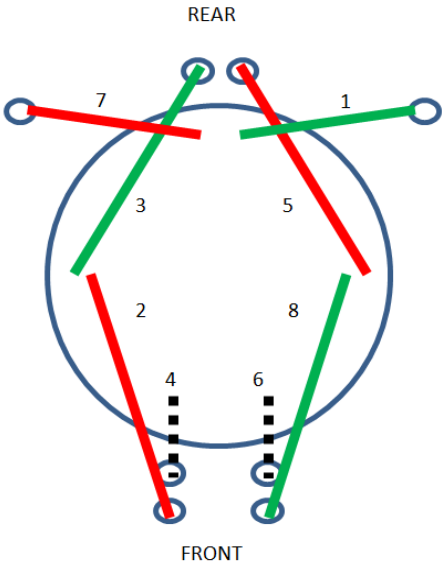

Figure 4.10 Agonist/antagonist pairs used in the yaw test.

4.5.4 Accelerometer/gyroscope calibration and smoothing using the Madgwick filter

As discussed earlier, the Arduino software environment was used to program the movements and data capture. To obtain angular displacements, translational displacements and translational velocities the accelerations and angular velocities were integrated. The problem with this is that the accelerations and angular velocities vary continuously with time, but due to sampling have to be fixed over the time step which leads to drift. This caused a severe skewing of the data. In addition, gravity needs to be removed from the acceleration data, which is not straight forward. The best method to tackle the problem was investigated and it became apparent that the use of a Madgwick filter (Madgwick, 2010) was a good approach. A Kalman filter was also considered, but discounted as it was found to have 18 times the computational burden of a Madgwick filter on embedded systems (Cavallo *et al.,* 2014), as used in this research. The Madgwick filter uses data from both the accelerator and gyroscope together within the Inertial Monitoring Unit (IMU) to accurately define the orientation on the sensors, and hence, the robot head. Madgwick's filter algorithm then uses these data to calculate four quaternions from each of the 3 axes of the gyroscope and accelerometer. Following this, the quaternions are then used to calculate Pitch, Roll and Yaw Euler angles. The Madgwick filter used was part of the Madgwick library for the Arduino IDE, which had to be downloaded and installed into the IDE.

When the program was uploaded to the system, the library commands used the Digital Motion Processor (DMP) built into the MPU6050 accelerator/gyroscope chip. This DMP enables 6 axis fusion algorithms to be carried out at 200Hz, which then outputs its data in the form of quaternions, and pitch, roll and yaw. For the purposes of this research, the quartenions were not needed. The outputs used were the pitch, roll and yaw angles calculated from the quaternions, and the X, Y and Z accelerations with gravity removed.

The actual physical calibration of the head was carried out by moving the head so that the three dots on the top of the skull aligned with the laser dots. This ensured that the accelerometers and gyroscopes always outputted a datum position at the start of the experimental run, in case absolute positions needed to be established in future work. The datum position would be held for ten seconds whilst the Madgwick filter calculated any offsets and drifts and compensated accordingly. The Arduino code used in the gyroscope and accelerometer data acquisition and the implementation of the Madgwick filtering was obtained from github.com (2016), and is reproduced in Appendix A6.

4.6 Results and discussion

As discussed earlier, 3 sets of experiments were carried out to establish the maximum angular velocities and ranges of the robotic neck; namely pitch, roll and yaw measurements. The data were collected as per the procedures, and then pasted into an Excel spreadsheet for further analysis and graphing. It was at this point that it became evident that despite using the Madgwick filter, a small amount gyroscope and accelerometer drift was still apparent in the data. This could be seen both in the acceleration figures and the Euler angles. The ranges and velocities could still be measured from the graphs, but it was decided to try and tackle the problem within Excel to reduce the drift even further. To compensate for this, firstly, the data were plotted for the acceleration and Euler angles for all the movements. Following this, a line of best fit for the drift was produced, which was then subtracted from the data. The result was a set of data with very much reduced drift, and which was flat enough to allow for accurate analysis. To calculate the angular speed, the Euler angles were differentiated with respect to time. This bought its own problem, in that it became necessary to know the time period between the Euler angle samples. That is, it became necessary to find out how quickly the Arduino processor was taking to perform one loop of the program code. The clock speed of the processor is of no use in this case, as it is merely an indication of how many clock cycles per second the processor can perform, and different programming operators can take a variety of clock cycles to complete. To measure that data rate accurately, the data were captured in 10 runs of 1 minute duration, and the samples counted then averaged over the 10 runs. This gave a figure of 66Hz for the capture rate, which was then used in the angular speed calculations.

4.6.1 Pitch (nod) test

The pitch test involved rotating the head through the Y axis from the viewpoint of the orientation of the accelerometer/gyroscope. Hence, this dimension was expected to show the largest ranges and velocities. The other (X and Z) dimensions were measured too, to establish the interplay between the differing movements, hence, the extent of coincidental movements. The non-rotational displacement in the Y axis was also measured.

Figure 4.11 shows the rotation angles in the Y plane, as can be seen the data were smooth, although some bounce and overshoot of the head can be seen at the extremes. The bounce was due to the fact that in the testing conditions, it was necessary to fully inflate one of the agonist/antagonist pair, whilst the opposing one was fully deflated, in order to get the absolute maximum figure for angular velocity. The overshoot was due to the inertia of the head. As can be seen, the head moved from -5° to +35°, giving an angular range of 40°. It was found that the somewhat limited backward tilt of the head of -5° was due to the

similarity in length of the agonist and antagonist muscle pairs used in the movement, whilst in nature they are of different lengths.

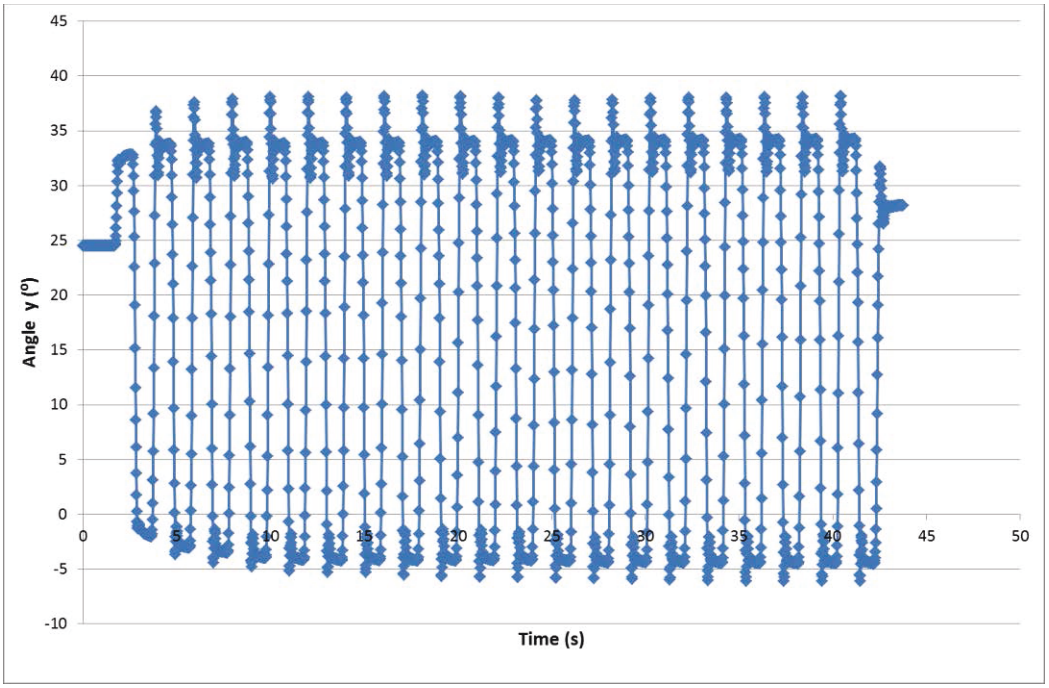

Figure 4.11 Rotation angle in the Y plane.

Figure 4.12 shows the results of a statistical analysis of accelerometer drift compensation in the Y plane during Y plane rotational movements. As can be seen, the Pearson product-moment correlation coefficient of 1 shows a total positive linear correlation between the drift-compensated accelerometer/gyroscope data and the absolute (non-drifting) ultrasonic data. The Kendall rank correlation coefficient shows a 95.7% likelihood of a statistical association between the drift-compensated accelerometer/gyroscope data and the absolute (non-drifting) ultrasonic data. Both sets of statistics confirm the accuracy of the drift-compensated accelerometer/gyroscope data, and hence the accuracy of the angular rotation figures.

```
CORRELATIONS
  /VARIABLES=AccelGyro Ultrasonic
  /PRINT=TWOTAIL NOSIG
  /MISSING=PAIRWISE.
```

Correlations

Correlations

		AccelGyro	Ultrasonic
AccelGyro	Pearson Correlation	1	1.000**
	Sig. (2-tailed)		.000
	N	2889	2889
Ultrasonic	Pearson Correlation	1.000**	1
	Sig. (2-tailed)	.000	
	N	2889	2889

**. Correlation is significant at the 0.01 level (2-tailed).

```
NONPAR CORR
  /VARIABLES=AccelGyro Ultrasonic
  /PRINT=KENDALL TWOTAIL NOSIG
  /MISSING=PAIRWISE.
```

Nonparametric Correlations

Correlations

			AccelGyro	Ultrasonic
Kendall's tau_b	AccelGyro	Correlation Coefficient	1.000	.957**
		Sig. (2-tailed)	.	.000
		N	2889	2889
	Ultrasonic	Correlation Coefficient	.957**	1.000
		Sig. (2-tailed)	.000	.
		N	2889	2889

**. Correlation is significant at the 0.01 level (2-tailed).

Figure 4.12 Statistical analysis of accelerometer drift compensation in the Y plane during Y plane rotational movements.

Figure 4.13 shows the angular velocities in the Y plane. It shows that the head achieved angular rotation speeds of around 300°/s. The 50°/s spikes are again evidence of the bounce exhibited at the extremes of the angular ranges.

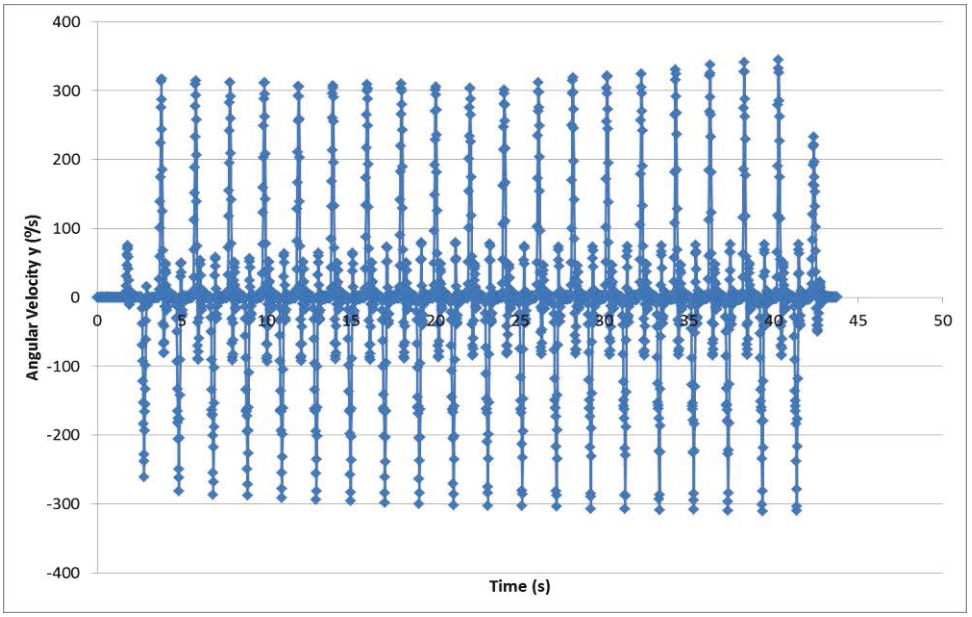

Figure 4.13 Angular velocity in the Y plane.

4.6.1.1 *Coincidental X (Roll/Tilt) plane movements during intentional Y (Pitch/Nod) plane movements*

Whilst the head was moving in the intentional direction, that is, the Y (pitch) plane, it can be seen from figure 4.14 that there was a small (5°) non-intentional movement in the X (roll) plane too. This is due to non-perfect matching of the muscle lengths various pairs of muscles.

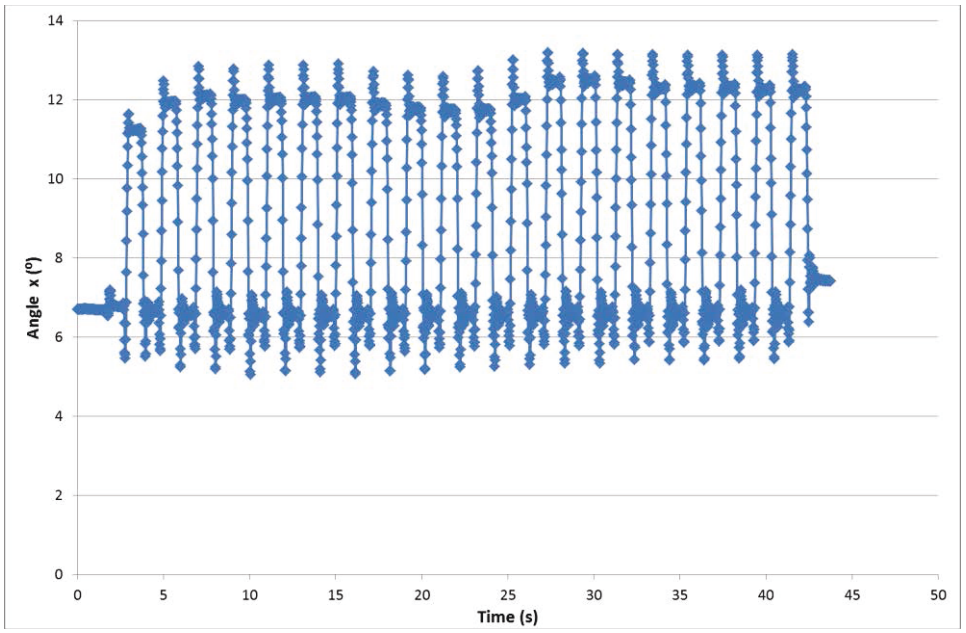

Figure 4.14 Rotation angle in the X plane during Y plane movement.

Figure 4.15 shows the results of a statistical analysis of accelerometer drift compensation in the X plane during Y plane rotational movements. With a Pearson product-moment

correlation coefficient of 1, and a Kendall rank correlation coefficient of 95.3% this again confirms the accuracy of the drift compensated data.

```
CORRELATIONS
  /VARIABLES=AccGyro Ultrasonic
  /PRINT=TWOTAIL NOSIG
  /MISSING=PAIRWISE.
```

Correlations

Correlations

		AccGyro	Ultrasonic
AccGyro	Pearson Correlation	1	1.000**
	Sig. (2-tailed)		.000
	N	2889	2889
Ultrasonic	Pearson Correlation	1.000**	1
	Sig. (2-tailed)	.000	
	N	2889	2889

**. Correlation is significant at the 0.01 level (2-tailed).

```
NONPAR CORR
  /VARIABLES=AccGyro Ultrasonic
  /PRINT=KENDALL TWOTAIL NOSIG
  /MISSING=PAIRWISE.
```

Nonparametric Correlations

Correlations

			AccGyro	Ultrasonic
Kendall's tau_b	AccGyro	Correlation Coefficient	1.000	.953**
		Sig. (2-tailed)	.	.000
		N	2889	2889
	Ultrasonic	Correlation Coefficient	.953**	1.000
		Sig. (2-tailed)	.000	.
		N	2889	2889

**. Correlation is significant at the 0.01 level (2-tailed).

Figure 4.15 Statistical analysis of accelerometer drift compensation in the X plane during Y plane rotational movements.

Figure 4.16 shows that the angular velocity for this X plane rotation was around a maximum of 90°/s. Again, the bounce of the head can be seen around the centre of the graph.

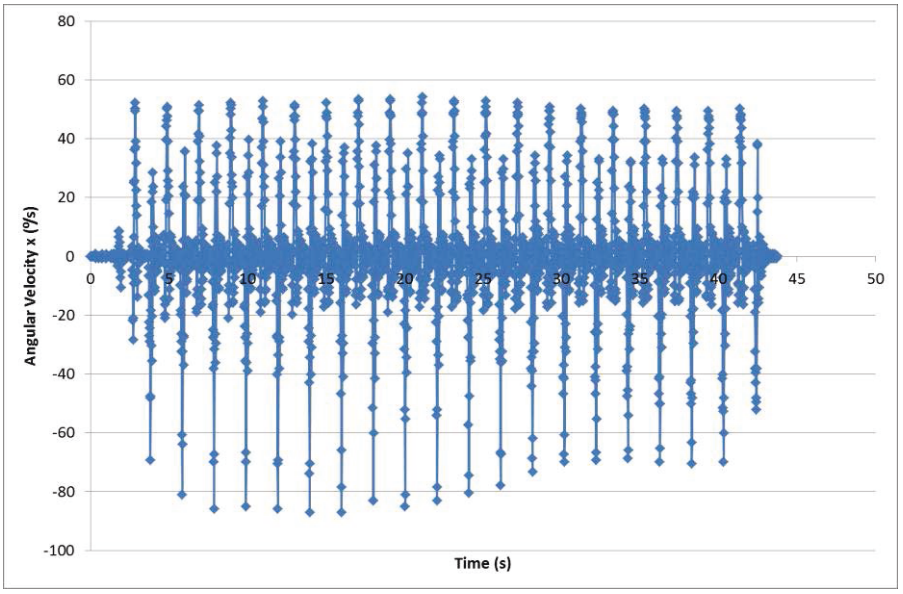

Figure 4.16 Angular velocity in the X plane during Y plane movement.

4.6.1.2 *Coincidental Z (Yaw/Rotate) plane movements during intentional Y (Pitch/Nod) plane movements*

As can be seen from figure 4.17, as the head nodded in the X plane, there was a small (3°) rotational movement in the Z plane. As also can be seen, that was a drift of around 3.5° in this movement, which has been visually exaggerated by the scaling of the Y axis of the graph. With such a small drift, it is quite difficult to put it down to any firm cause, although it is conjectured that this was due to a combination of non-perfect muscle length matching of the various pairs, and stiction between the wooden vertebra. The non-length matching was also the cause of the larger overshoot in the positive direction.

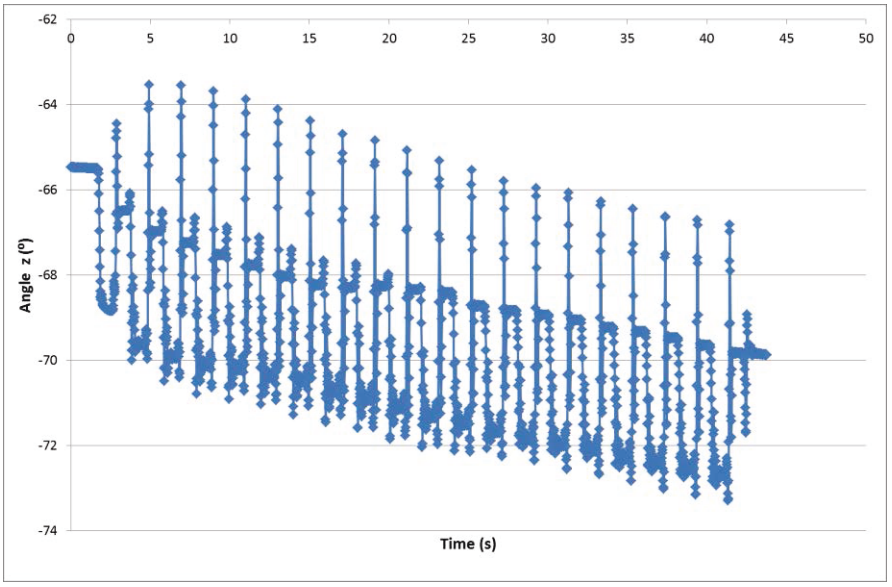

Figure 4.17 Rotation angle in the Z plane during Y plane movement.

Figure 4.18 shows the results of a statistical analysis of accelerometer drift compensation in the Z plane during Y plane rotational movements. With a Pearson product-moment correlation coefficient of 1, and a Kendall rank correlation coefficient of 97.8% this again confirms the accuracy of the drift compensated data.

In one way, this is a particularly pleasing result, as it shows that the evidential skew in the data really was due to a physical skewing of the head (although this was unintentional), rather than any drift in the accelerometer/gyroscope data.

```
CORRELATIONS
  /VARIABLES=VAR00029 VAR00030
  /PRINT=TWOTAIL NOSIG
  /MISSING=PAIRWISE.
```

Correlations

```
[DataSet0] C:\Users\p0035206\Desktop\Latest stats\Nod Z.sav
```

Correlations

		VAR00029	VAR00030
VAR00029	Pearson Correlation	1	1.000**
	Sig. (2-tailed)		.000
	N	2889	2889
VAR00030	Pearson Correlation	1.000**	1
	Sig. (2-tailed)	.000	
	N	2889	2889

**. Correlation is significant at the 0.01 level (2-tailed).

```
NONPAR CORR
  /VARIABLES=VAR00029 VAR00030
  /PRINT=KENDALL TWOTAIL NOSIG
  /MISSING=PAIRWISE.
```

Nonparametric Correlations

Correlations

			VAR00029	VAR00030
Kendall's tau_b	VAR00029	Correlation Coefficient	1.000	.978**
		Sig. (2-tailed)	.	.000
		N	2889	2889
	VAR00030	Correlation Coefficient	.978**	1.000
		Sig. (2-tailed)	.000	.
		N	2889	2889

**. Correlation is significant at the 0.01 level (2-tailed).

Figure 4.18 Statistical analysis of accelerometer drift compensation in the Z plane during Y plane rotational movements.

Figure 4.19 demonstrates that these small Z plane rotations took place at a maximum of around 120°/s. That is, although the movements were small, they happened quite quickly.

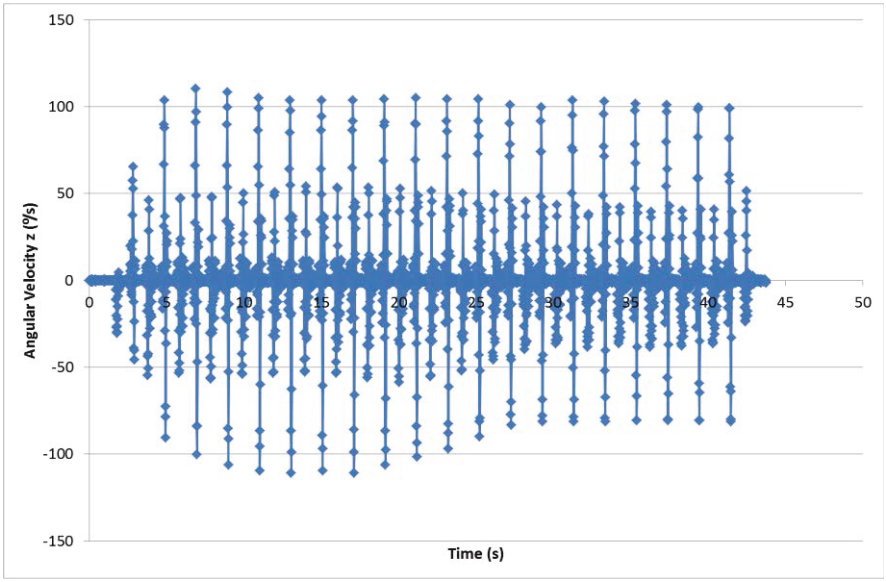

Figure 4.19 Angular velocity in the Z plane during Y plane movement.

4.6.1.3 Non-rotational lateral translations in Y plane during Y plane rotational movements

Figure 4.20, using data from the accelerometer/gyroscopes to show there was non-rotational lateral movement in the Y plane, during Y plane rotational movement. This movement was around 8 centimetres, and as such, demonstrates the robot's capability to perform the sliding front to back movements necessary for the accurate replication of human head gestures. It must be noted that the graph shows relative movement in a positive and negative direction, and therefore the total movement is the correctly stated 8 centimetres, and not 16 centimetres. Also note the large degree of bounce with each movement.

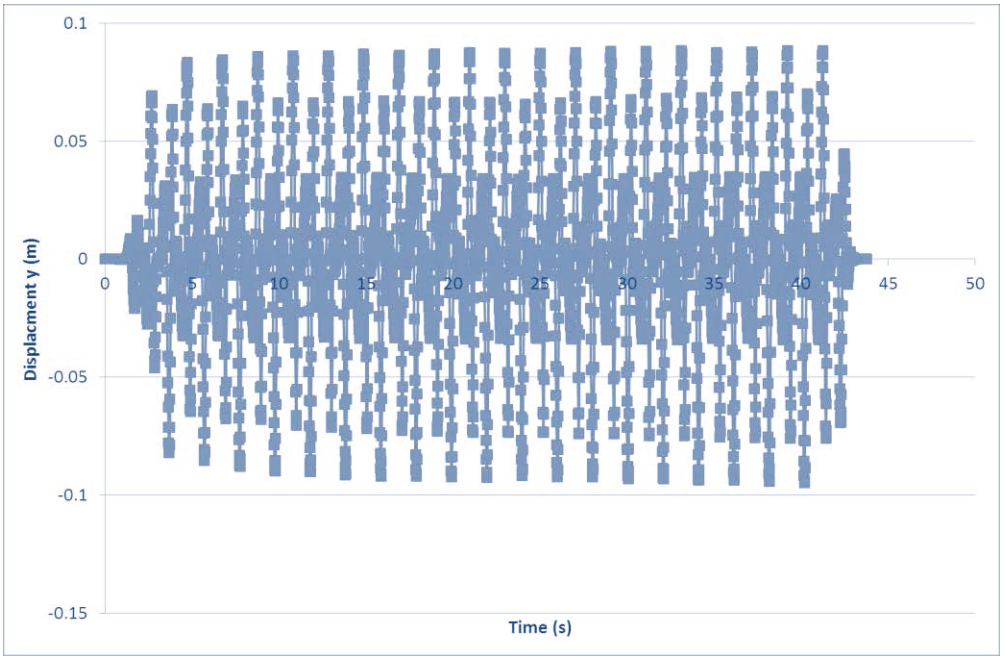

Figure 4.20 Non-rotational lateral translations in Y plane in during Y plane rotational movements.

Figure 4.21 shows the results of a statistical analysis of accelerometer drift compensation in the Y plane during Y plane non-rotational lateral translations. With a Pearson product-moment correlation coefficient of 1, and a Kendall rank correlation coefficient of 99.7% this confirms the very high accuracy of the drift compensated data.

```
CORRELATIONS
  /VARIABLES=VAR00001 VAR00002
  /PRINT=TWOTAIL NOSIG
  /MISSING=PAIRWISE.
```

Correlations

Correlations

		VAR00001	VAR00002
VAR00001	Pearson Correlation	1	1.000**
	Sig. (2-tailed)		.000
	N	2848	2848
VAR00002	Pearson Correlation	1.000**	1
	Sig. (2-tailed)	.000	
	N	2848	2848

**. Correlation is significant at the 0.01 level (2-tailed).

```
NONPAR CORR
  /VARIABLES=VAR00001 VAR00002
  /PRINT=KENDALL TWOTAIL NOSIG
  /MISSING=PAIRWISE.
```

Nonparametric Correlations

Correlations

			VAR00001	VAR00002
Kendall's tau_b	VAR00001	Correlation Coefficient	1.000	.997**
		Sig. (2-tailed)	.	.000
		N	2848	2848
	VAR00002	Correlation Coefficient	.997**	1.000
		Sig. (2-tailed)	.000	.
		N	2848	2848

**. Correlation is significant at the 0.01 level (2-tailed).

Figure 4.2115 Statistical analysis of accelerometer drift compensation in the Y plane during Y plane non-rotational lateral translations.

To put the Y planes figures into perspective, figure 4.22 shows photos of the head at the extremes of movement. As can be seen, the lengths of the sternocleidomastoid muscles limit the capacity of the head to tilt backwards.

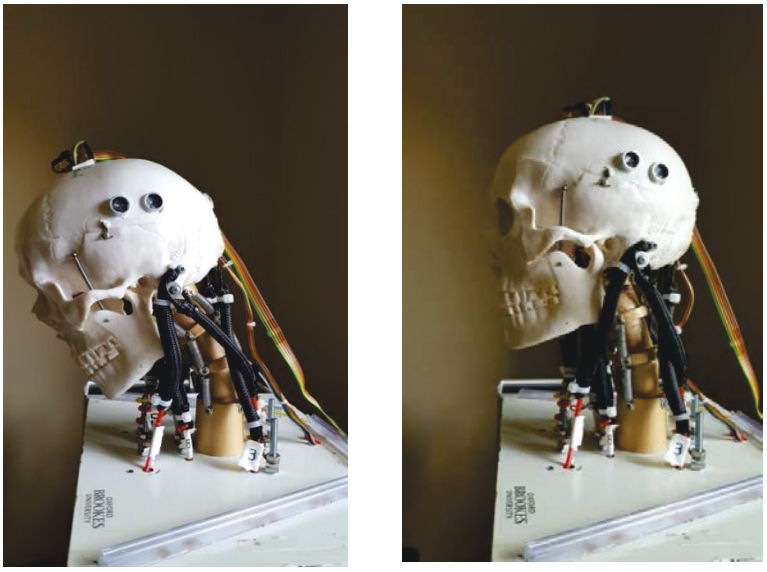

Figure 4.2216 Different poses of the head at maximum pitch angles.

4.6.2 Roll (tilt) test

The pitch test involved rotating the head through the X axis from the viewpoint of the orientation of the accelerometer/gyroscope. Hence, this dimension was expected to show the largest ranges and velocities. As in the previous experiment the other (Y and Z) dimensions were measured too, to establish the interplay between the differing movements, leading to non-intentional movements in other planes.

Figure 4.23 shows at total swing of 45°. As in the previous experiments, there was an overshoot due to the inertia of the head.

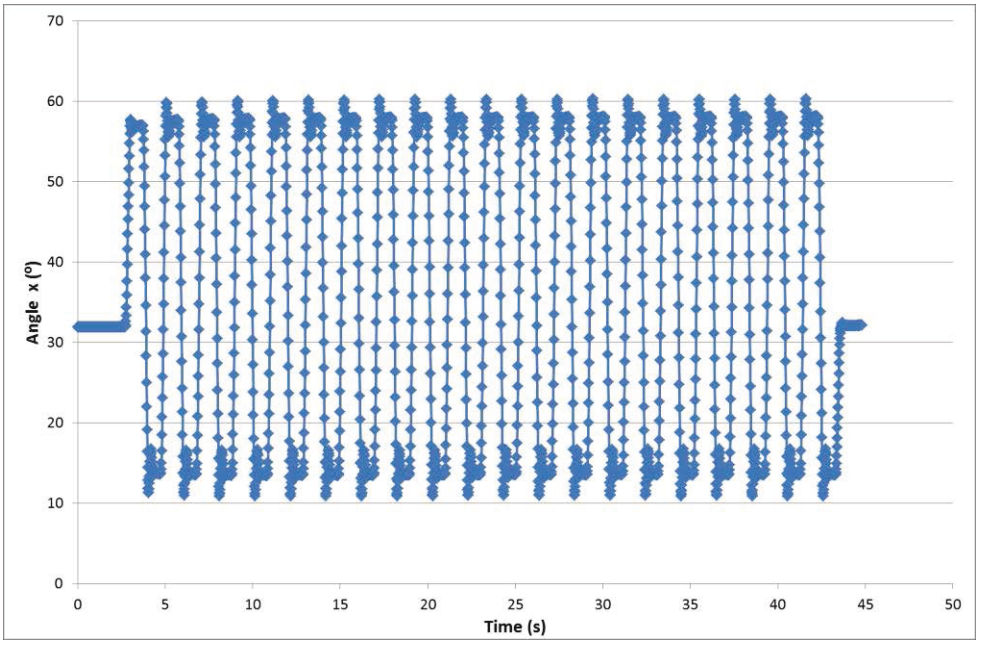

Figure 4.173 Rotation angle in the X plane.

Figure 4.24 shows the results of a statistical analysis of accelerometer drift compensation in the X plane during X rotations. With a Pearson product-moment correlation coefficient of 1, and a Kendall rank correlation coefficient of 95.8% this confirms the accuracy of the drift compensated data.

```
CORRELATIONS
  /VARIABLES=VAR00007 VAR00008
  /PRINT=TWOTAIL NOSIG
  /MISSING=PAIRWISE.
```

Correlations

Correlations

		VAR00007	VAR00008
VAR00007	Pearson Correlation	1	1.000**
	Sig. (2-tailed)		.000
	N	2959	2959
VAR00008	Pearson Correlation	1.000**	1
	Sig. (2-tailed)	.000	
	N	2959	2959

**. Correlation is significant at the 0.01 level (2-tailed).

```
NONPAR CORR
  /VARIABLES=VAR00007 VAR00008
  /PRINT=KENDALL TWOTAIL NOSIG
  /MISSING=PAIRWISE.
```

Nonparametric Correlations

Correlations

			VAR00007	VAR00008
Kendall's tau_b	VAR00007	Correlation Coefficient	1.000	.958**
		Sig. (2-tailed)	.	.000
		N	2959	2959
	VAR00008	Correlation Coefficient	.958**	1.000
		Sig. (2-tailed)	.000	.
		N	2959	2959

**. Correlation is significant at the 0.01 level (2-tailed).

Figure 4.24 Statistical analysis of accelerometer drift compensation in the X plane during X plane rotational movements.

Figure 4.25 shows that during the X plane rotation speeds of 230°/s were reached.

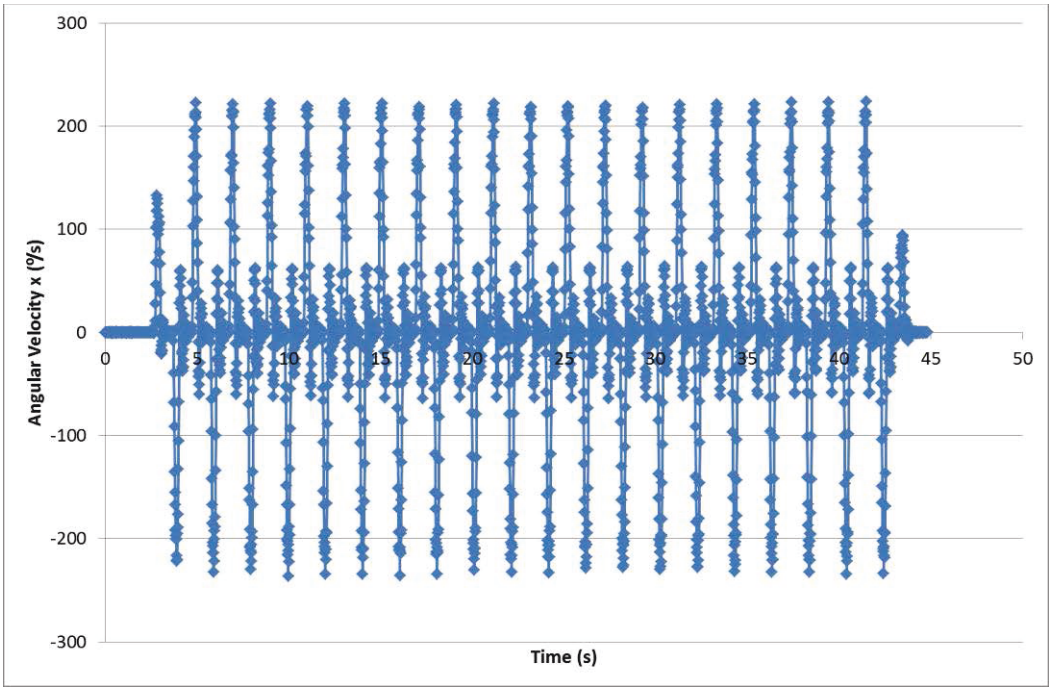

Figure 4.25 Angular velocity in the X plane.

4.6.2.1 *Coincidental Y (Pitch/Nod) plane movements during intentional X (Roll/Tilt) plane movements*

Figure 4.26 shows that there was a non-intentional rotation of 5° in the Y plane during the X plane movement. It can be seen that upon starting the X plane movements the head was pulled from its neutral position by around 11°, as well as exhibiting a non-symmetrical bounce. This was due to the non-matching of the muscle lengths.

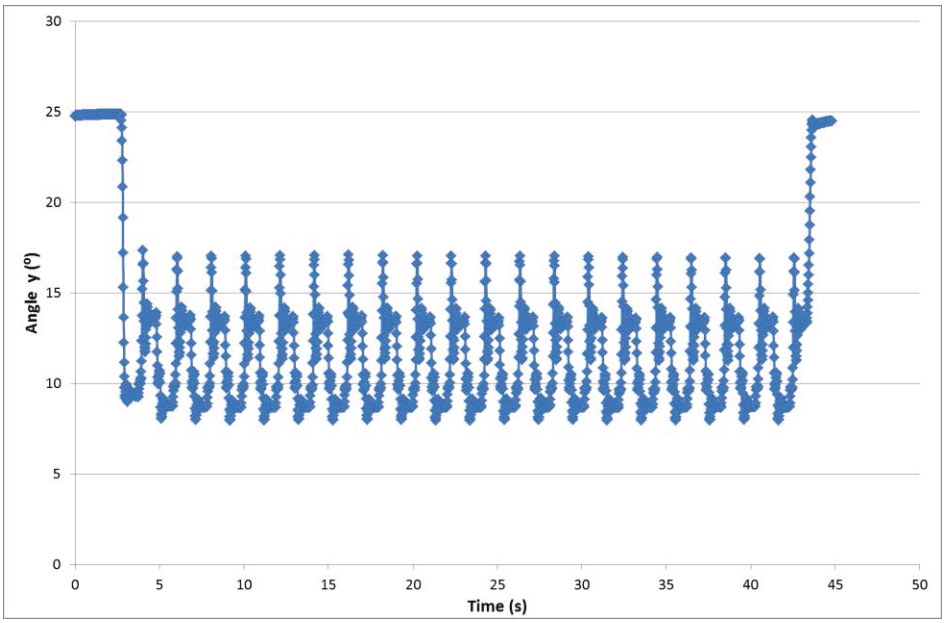

Figure 4.26 Rotation angle in the Y plane during X plane movement.

Figure 4.27 shows the results of a statistical analysis of accelerometer drift compensation in the Y plane during X rotations. With a Pearson product-moment correlation coefficient of 1, and a Kendall rank correlation coefficient of 95.1% this confirms the accuracy of the drift compensated data.

```
CORRELATIONS
  /VARIABLES=AccGyro Ultrasonic
  /PRINT=TWOTAIL NOSIG
  /MISSING=PAIRWISE.
```

Correlations

Correlations

		AccGyro	Ultrasonic
AccGyro	Pearson Correlation	1	1.000**
	Sig. (2-tailed)		.000
	N	2959	2959
Ultrasonic	Pearson Correlation	1.000**	1
	Sig. (2-tailed)	.000	
	N	2959	2959

**. Correlation is significant at the 0.01 level (2-tailed).

```
NONPAR CORR
  /VARIABLES=AccGyro Ultrasonic
  /PRINT=KENDALL TWOTAIL NOSIG
  /MISSING=PAIRWISE.
```

Nonparametric Correlations

Correlations

			AccGyro	Ultrasonic
Kendall's tau_b	AccGyro	Correlation Coefficient	1.000	.951**
		Sig. (2-tailed)	.	.000
		N	2959	2959
	Ultrasonic	Correlation Coefficient	.951**	1.000
		Sig. (2-tailed)	.000	.
		N	2959	2959

**. Correlation is significant at the 0.01 level (2-tailed).

Figure 4.27 Statistical analysis of accelerometer drift compensation in the Y plane during X plane rotational movements.

Figure 4.28 shows that the head achieved a maximum Y plane angular velocity of 100°/s during the X plane movements. Also evident is the non-symmetry of the velocities in the plus and minus directions, which correlates well with the skewing phenomena and causes demonstrated in figure 4.26.

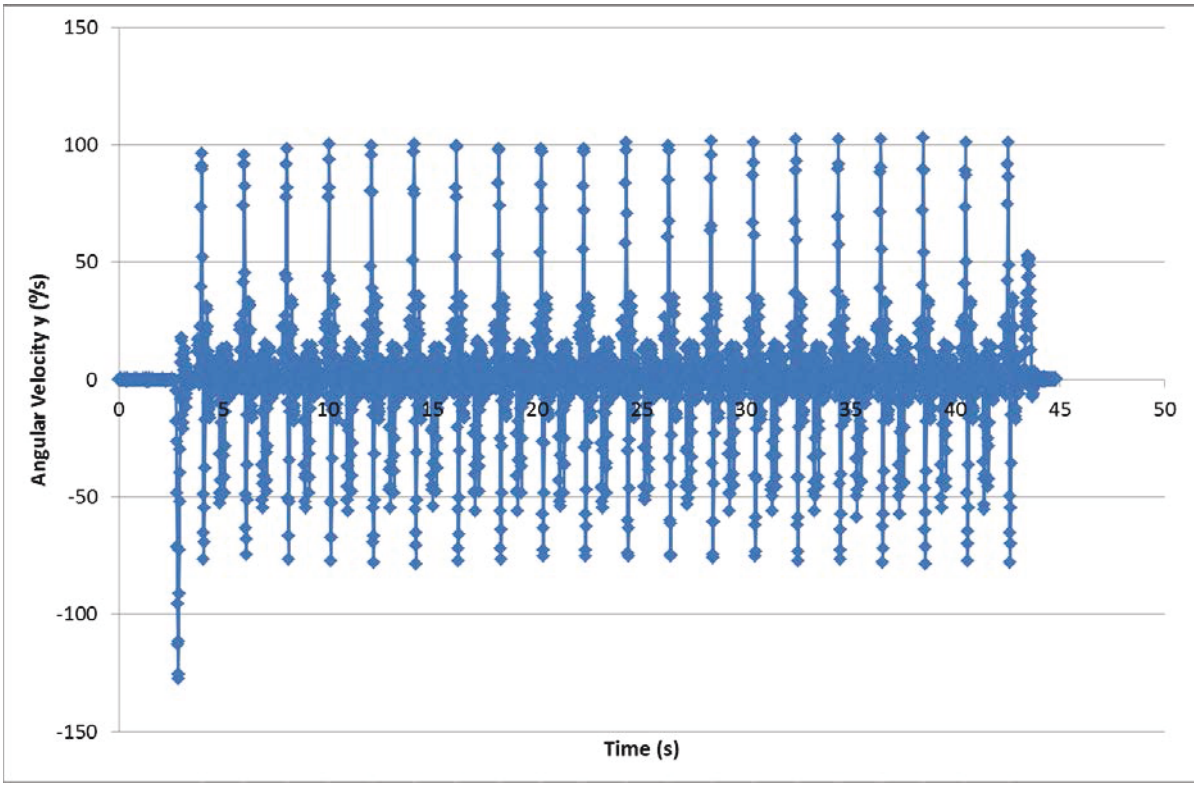

Figure 4.28 Angular velocity in the Y plane during X plane movement.

4.6.2.2 *Coincidental Z (Yaw/Rotate) plane movements during intentional X (Roll/Tilt) plane movements*

Figure 4.29 shows a 19° rotation in the Z plane during X plane movements. As in the other figures pertaining to X plane movement, it also shows a non-symmetrical skew and bounce due to non-matching of the muscle lengths.

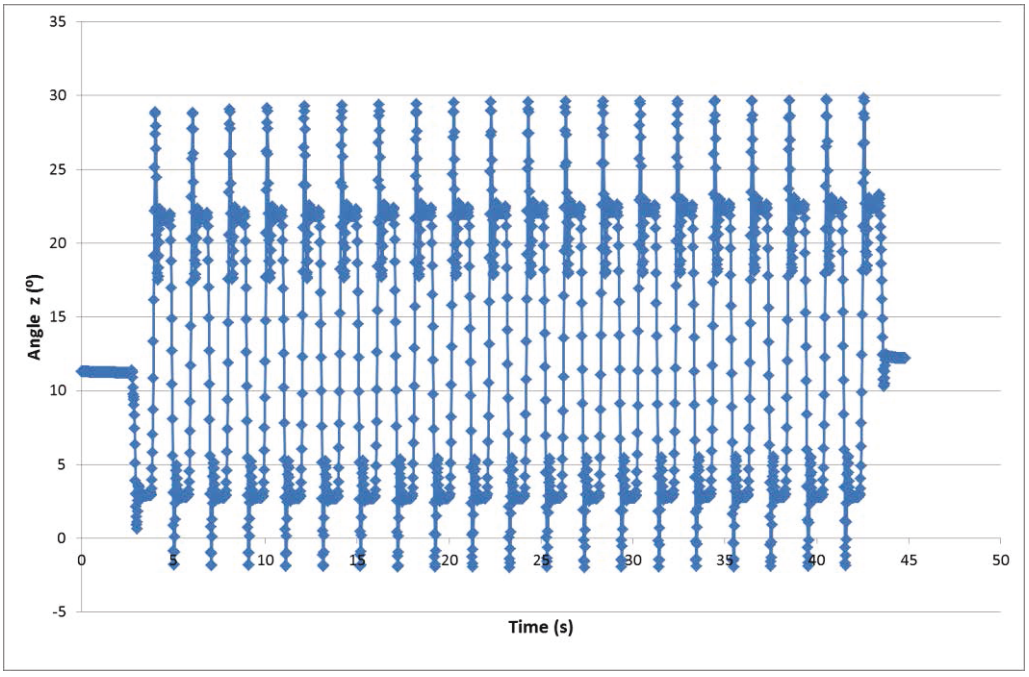

Figure 4.29 Rotation angle in the Z plane during X plane movement.

Figure 4.30 shows the results of a statistical analysis of accelerometer drift compensation in the Z plane during X rotations. With a Pearson product-moment correlation coefficient of 1, and a Kendall rank correlation coefficient of 97.1% this confirms the accuracy of the drift compensated data.

```
CORRELATIONS
  /VARIABLES=AccGyro Ultrasonic
  /PRINT=TWOTAIL NOSIG
  /MISSING=PAIRWISE.
```

Correlations

Correlations

		AccGyro	Ultrasonic
AccGyro	Pearson Correlation	1	1.000**
	Sig. (2-tailed)		.000
	N	2959	2959
Ultrasonic	Pearson Correlation	1.000**	1
	Sig. (2-tailed)	.000	
	N	2959	2959

**. Correlation is significant at the 0.01 level (2-tailed).

```
NONPAR CORR
  /VARIABLES=AccGyro Ultrasonic
  /PRINT=KENDALL TWOTAIL NOSIG
  /MISSING=PAIRWISE.
```

Nonparametric Correlations

Correlations

			AccGyro	Ultrasonic
Kendall's tau_b	AccGyro	Correlation Coefficient	1.000	.971**
		Sig. (2-tailed)	.	.000
		N	2959	2959
	Ultrasonic	Correlation Coefficient	.971**	1.000
		Sig. (2-tailed)	.000	.
		N	2959	2959

**. Correlation is significant at the 0.01 level (2-tailed).

Figure 4.30 Statistical analysis of accelerometer drift compensation in the Z plane during X plane rotational movements.

Figure 4.31 shows that during the X plane movement, the head reached speeds of 200°/s in the Z plane.

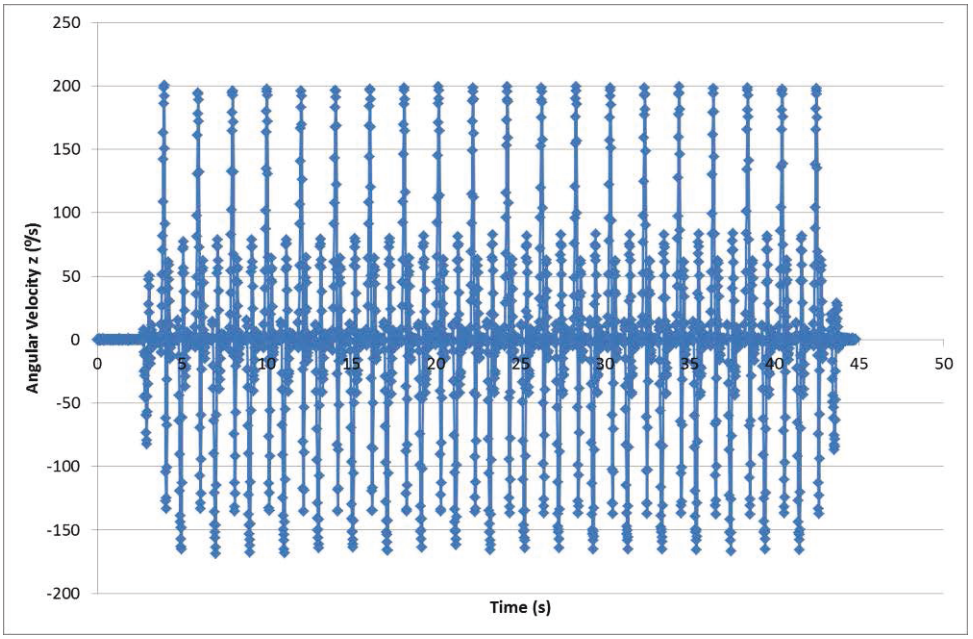

Figure 4.31 Angular velocity in the Z plane during X plane movement.

4.6.2.3 *Non-rotational lateral translations in X plane in during X plane rotational movements*

As the data from the accelerometer/gyroscopes show in figure 4.32, there was non-rotational lateral movement in the X plane, during X plane rotational movement. This movement was over 10 centimetres, and as such, demonstrates the robots capability to perform the sliding shoulder to shoulder movements necessary for the accurate replication of human head gestures. It can also be seen from figure 5.25 that there is an asymmetry. This was due to the no-matching of the opposing muscle lengths.

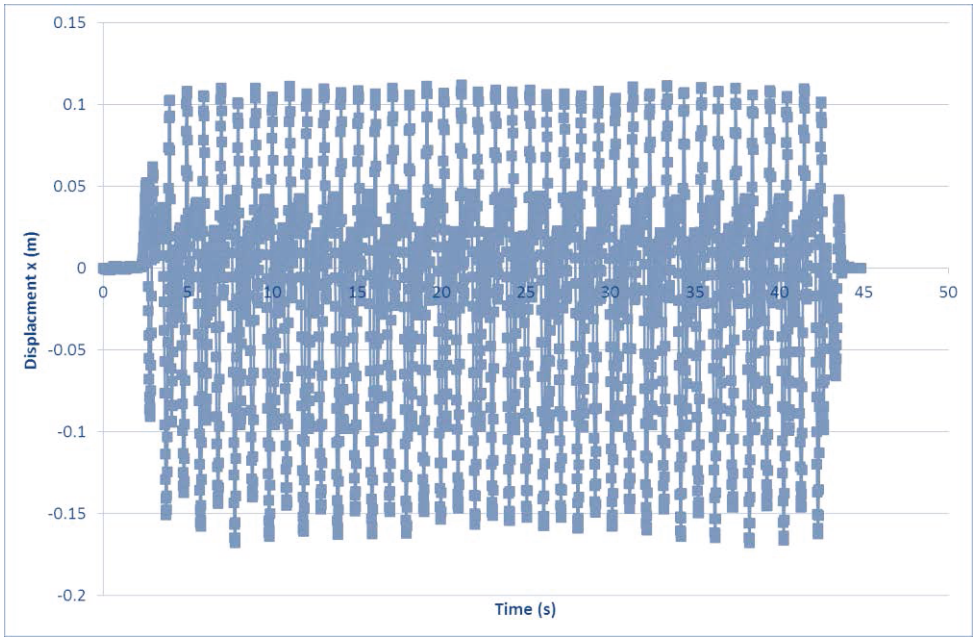

Figure 4.32 Non-rotational lateral translations in X plane in during X plane rotational movements.

Figure 4.33 shows the results of a statistical analysis of accelerometer drift compensation in the X plane during X plane non-rotational lateral translations. With a Pearson product-moment correlation coefficient of 1, and a Kendall rank correlation coefficient of 99.5% this confirms the accuracy of the drift compensated data.

```
CORRELATIONS
  /VARIABLES=AccelGyro Ultrasonic
  /PRINT=TWOTAIL NOSIG
  /MISSING=PAIRWISE.
```

Correlations

```
[DataSet0]
```

Correlations

		AccelGyro	Ultrasonic
AccelGyro	Pearson Correlation	1	1.000**
	Sig. (2-tailed)		.000
	N	2878	2878
Ultrasonic	Pearson Correlation	1.000**	1
	Sig. (2-tailed)	.000	
	N	2878	2878

**. Correlation is significant at the 0.01 level (2-tailed).

```
NONPAR CORR
  /VARIABLES=AccelGyro Ultrasonic
  /PRINT=KENDALL TWOTAIL NOSIG
  /MISSING=PAIRWISE.
```

Nonparametric Correlations

Correlations

			AccelGyro	Ultrasonic
Kendall's tau_b	AccelGyro	Correlation Coefficient	1.000	.995**
		Sig. (2-tailed)	.	.000
		N	2878	2878
	Ultrasonic	Correlation Coefficient	.995**	1.000
		Sig. (2-tailed)	.000	.
		N	2878	2878

**. Correlation is significant at the 0.01 level (2-tailed).

Figure 4.33 Statistical analysis of accelerometer drift compensation in the X plane during X plane non-rotational lateral translations.

Figure 4.34 shows photos of the head at its maximum roll angles, and clearly shows the asymmetry of movement due to the non-matching of the muscle lengths.

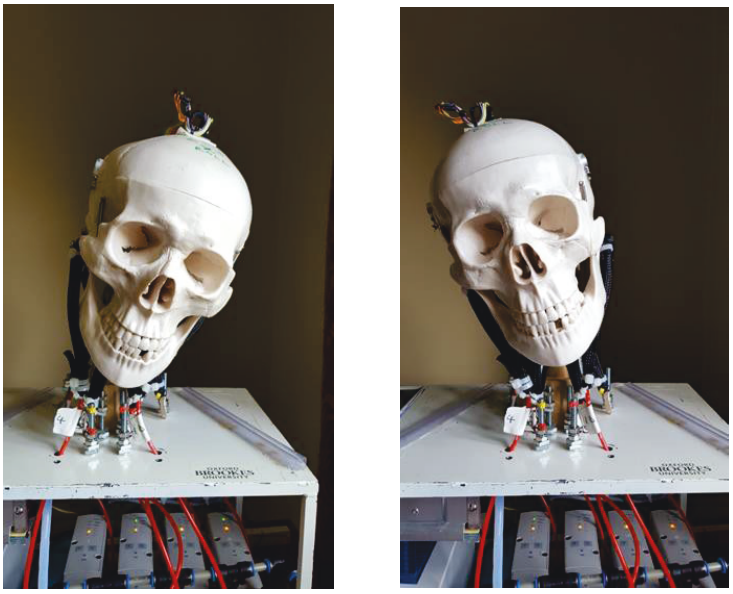

Figure 4.34 Different poses of the head at maximum roll angles.

4.6.3 Yaw (rotate) test

The pitch test involved rotating the head through the Z axis from the viewpoint of the orientation of the accelerometer/gyroscope. Hence, this dimension was expected to show the largest ranges and velocities. As with the pitch and roll tests, the other (X and Y) dimensions were measured too, to establish the interplay between the differing movements, and hence, the extent of Coincidental movements.

It can be seen from figure 4.35 that the head moved over a 26° range in the Z plane. Again, a skewing can be seen due to the mismatch of muscle lengths. This is also the reason for the larger overshoot at one end of the movement when compared to the other, although both are comparatively small, as is the bounce.

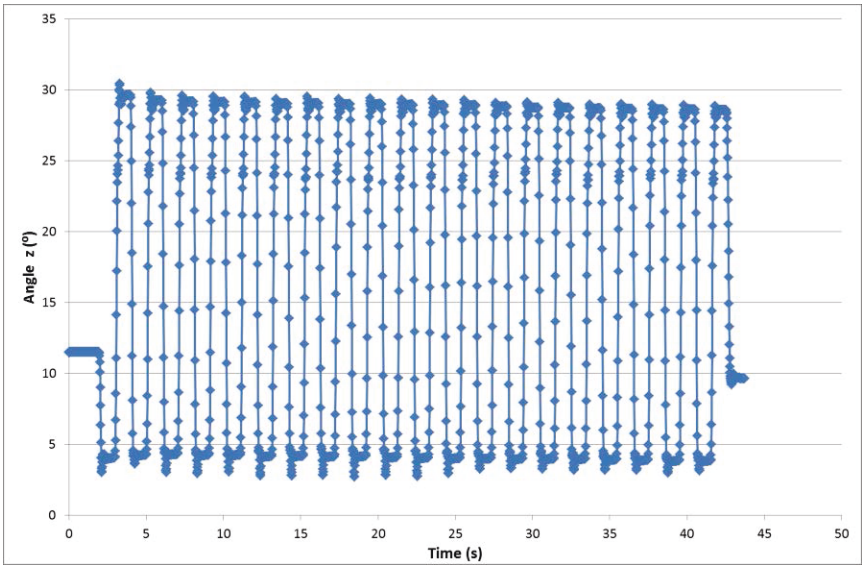

Figure 4.35 Rotation angle in the Z plane.

Figure 4.36 shows the results of a statistical analysis of accelerometer drift compensation in the Z plane during Z plane rotations. The Pearson product-moment correlation coefficient of 1 is pleasing, however, Kendall rank correlation coefficient of 94.7% is 0.3% below the threshold of statistical significance. This is not too disappointing though, as it still shows a 94.7% accuracy of the drift compensated data.

```
CORRELATIONS
  /VARIABLES=AccGyro Ultrasonic
  /PRINT=TWOTAIL NOSIG
  /MISSING=PAIRWISE.
```

Correlations

```
[DataSet2] C:\Users\p0035206\OneDrive\PhD\Steve's PhD writin
```

Correlations

		AccGyro	Ultrasonic
AccGyro	Pearson Correlation	1	1.000**
	Sig. (2-tailed)		.000
	N	2888	2888
Ultrasonic	Pearson Correlation	1.000**	1
	Sig. (2-tailed)	.000	
	N	2888	2888

**. Correlation is significant at the 0.01 level (2-tailed).

```
NONPAR CORR
  /VARIABLES=AccGyro Ultrasonic
  /PRINT=KENDALL TWOTAIL NOSIG
  /MISSING=PAIRWISE.
```

Nonparametric Correlations

Correlations

			AccGyro	Ultrasonic
Kendall's tau_b	AccGyro	Correlation Coefficient	1.000	.947**
		Sig. (2-tailed)	.	.000
		N	2888	2888
	Ultrasonic	Correlation Coefficient	.947**	1.000
		Sig. (2-tailed)	.000	.
		N	2888	2888

**. Correlation is significant at the 0.01 level (2-tailed).

Figure 4.36 Statistical analysis of accelerometer drift compensation in the Z plane during Z plane rotations.

Figure 4.37 shows that during the Z plane rotation the head reached speeds of up to 240°/s, with only around 20°/s for the bounce.

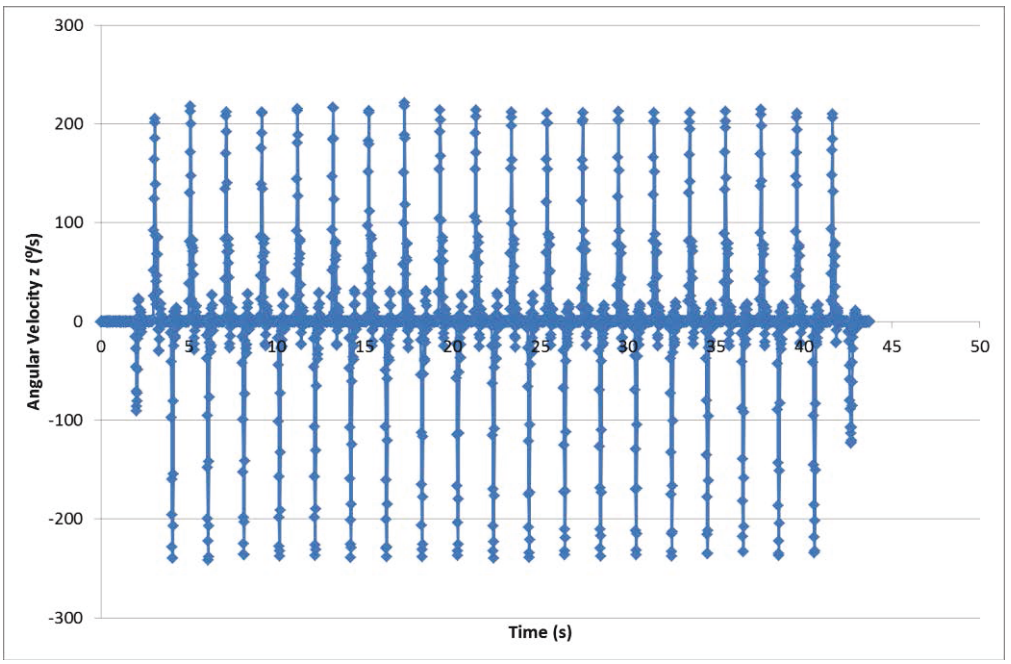

Figure 4.37 Angular velocity in the Z plane.

4.6.3.1 *Coincidental X (Roll/Tilt) plane movements during intentional Z (Yaw/Rotate) plane movements*

Figure 4.38 shows the degree of X plane movement during Z plane rotations. As can be seen, there was a 16° movement, with very negligible bounce and overshoot.

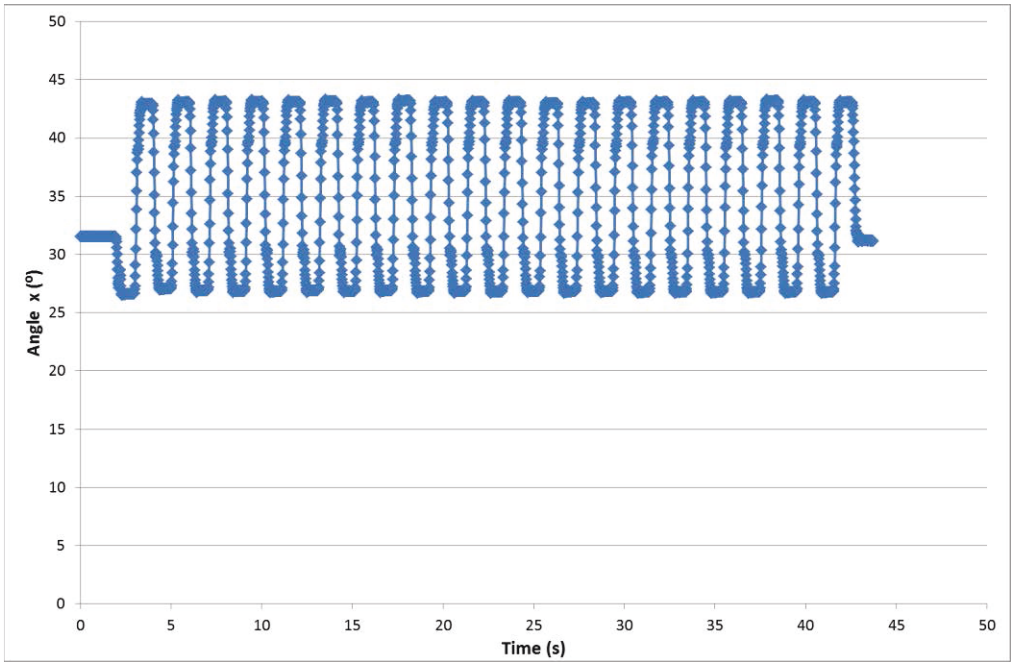

Figure 4.38 Rotation angle in the X plane during Z plane movement.

Figure 4.39 shows the results of a statistical analysis of accelerometer drift compensation in the X plane during Z plane rotations. The Pearson product-moment correlation coefficient of 1, and the Kendall rank correlation coefficient of 95.4% shows the accuracy of the drift compensated data.

```
CORRELATIONS
  /VARIABLES=VAR00017 VAR00018
  /PRINT=TWOTAIL NOSIG
  /MISSING=PAIRWISE.
```

Correlations

Correlations

		VAR00017	VAR00018
VAR00017	Pearson Correlation	1	1.000**
	Sig. (2-tailed)		.000
	N	2887	2887
VAR00018	Pearson Correlation	1.000**	1
	Sig. (2-tailed)	.000	
	N	2887	2887

**. Correlation is significant at the 0.01 level (2-tailed).

```
NONPAR CORR
  /VARIABLES=VAR00017 VAR00018
  /PRINT=KENDALL TWOTAIL NOSIG
  /MISSING=PAIRWISE.
```

Nonparametric Correlations

Correlations

			VAR00017	VAR00018
Kendall's tau_b	VAR00017	Correlation Coefficient	1.000	.954**
		Sig. (2-tailed)	.	.000
		N	2887	2887
	VAR00018	Correlation Coefficient	.954**	1.000
		Sig. (2-tailed)	.000	.
		N	2887	2887

**. Correlation is significant at the 0.01 level (2-tailed).

Figure 4.39 Rotation angle in the X plane during Z plane movement.

Figure 4.40 shows that the X plane rotation during the Z plane movement was limited to around 140°/s.

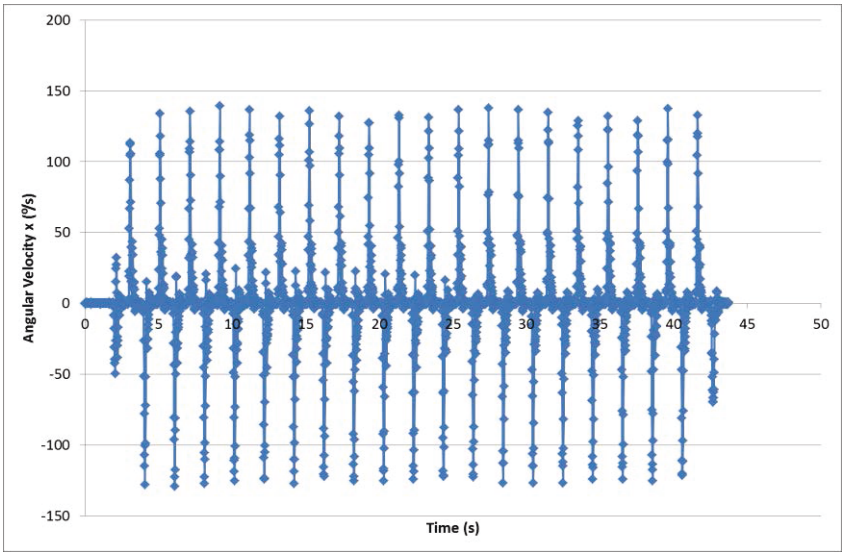

Figure 4.40 Angular velocity in the X plane during Z plane movement.

4.6.3.2 *Coincidental Y (Pitch/Nod) plane movements during intentional Z (Yaw/Rotate) plane movements*

Figure 4.41 shows the Y plane movement during Z plane rotation, which can be seen to be around 3°. The figure also shows some interesting phenomena. Firstly, the 18° skew from its initial position, due to the non-matching of the muscle lengths, which also caused the non-symmetrical bounce. The skew can be seen to correct itself when the muscles are released at the end of the experimental run. Secondly, as can be seen that as the head moves in one particular direction in the (intentional) Z plane, it causes a jerk in one (Coincidental) direction of the Y plane before moving in the other direction. This is due to the complexity of construction of the neck, and poses an interesting question for future work.

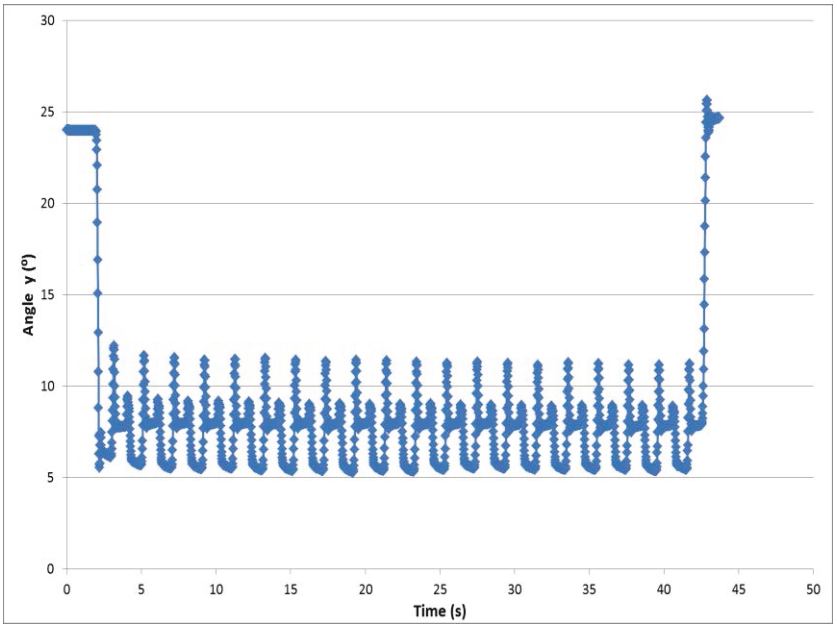

Figure 4.41 Rotation angle in the Y plane during Z plane movement.

Figure 4.42 shows the results of a statistical analysis of accelerometer drift compensation in the Y plane during Z plane rotations. The Pearson product-moment correlation coefficient of 1, and the Kendall rank correlation coefficient of 95.8% shows the accuracy of the drift compensated data. Again, pleasing to see that the 18° skew in the data was really due to the physical skewing of the head (although this was unintentional), rather than accelerometer drift.

```
CORRELATIONS
  /VARIABLES=AccGyro Ultrasonic
  /PRINT=TWOTAIL NOSIG
  /MISSING=PAIRWISE.
```

Correlations

Correlations

		AccGyro	Ultrasonic
AccGyro	Pearson Correlation	1	1.000**
	Sig. (2-tailed)		.000
	N	2888	2888
Ultrasonic	Pearson Correlation	1.000**	1
	Sig. (2-tailed)	.000	
	N	2888	2888

**. Correlation is significant at the 0.01 level (2-tailed).

```
NONPAR CORR
  /VARIABLES=AccGyro Ultrasonic
  /PRINT=KENDALL TWOTAIL NOSIG
  /MISSING=PAIRWISE.
```

Nonparametric Correlations

Correlations

			AccGyro	Ultrasonic
Kendall's tau_b	AccGyro	Correlation Coefficient	1.000	.958**
		Sig. (2-tailed)	.	.000
		N	2888	2888
	Ultrasonic	Correlation Coefficient	.958**	1.000
		Sig. (2-tailed)	.000	.
		N	2888	2888

**. Correlation is significant at the 0.01 level (2-tailed).

Figure 4.42 Rotation angle in the Y plane during Z plane movement.

Figure 4.43 shows that the Y plane rotations during Z plane movement were limited to around 55°/s, with a bounce of around 20°/s. The spikes at the beginning and end of the experimental run correlate directly with the skewing and correction shown in figure 4.41.

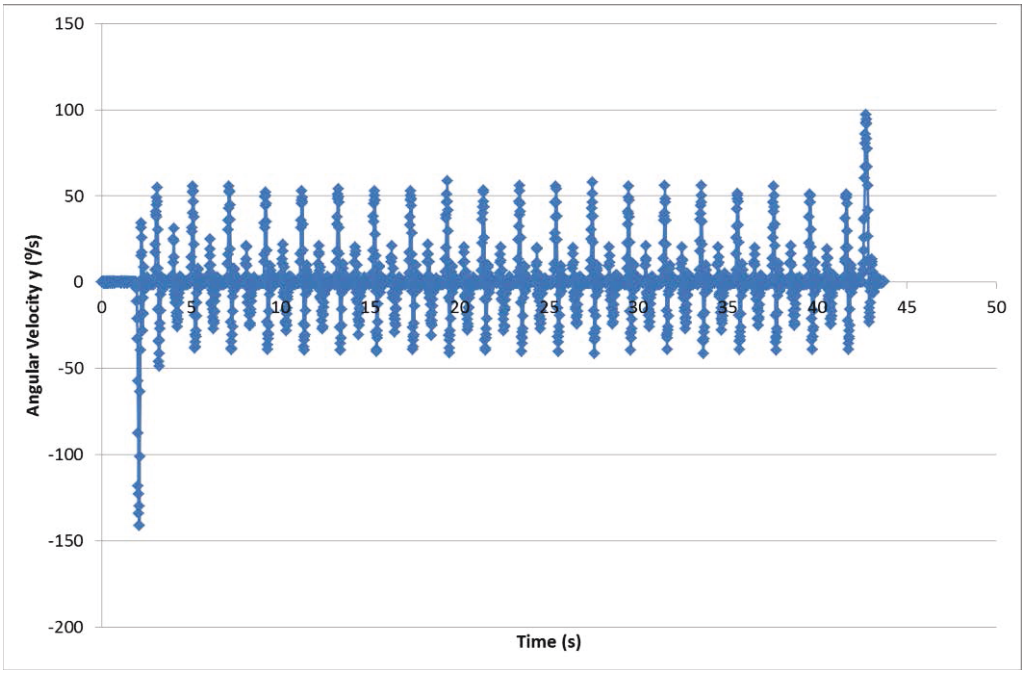

Figure 4.43 Angular velocity in the X plane during Z plane movement.

Figure 4.44 shows different poses of the head at its maximum yaw angles.

Figure 4.44 Different poses of the head at maximum yaw angles.

4.7 Evaluating the emotional response to the robot.

Having now measured the physical parameters of the robot's movements, experiments were carried out to establish the emotional reaction of human participants to the robot whilst undertaking a series of movements. That is, the subjective reaction, as opposed to the objective measurements taken thus far. As the robot performed both rotational and non-rotation translations, the reactions are based on these.

To undertake this, a series of three videos were taken, one each of ; a) the robot presented in this thesis, b) another humanoid robot, known as Robothespian (engineeredarts.co.uk, 2017), and c) a human (referred to as 'Human' in the statistics). As Robothespian was not able to reproduce non-rotational translational movements, and also the human found it impossible to consciously perform them, the videos for comparison were chosen to be of a very similar set of movements for the robots and the human, and they were all exactly 55 seconds in length. Perhaps if it were possible to program normal human communicative head gestures at this stage, then this would have been a useful evaluation, as the evaluators could have been questioned regarding what was being communicated the robot.

The testing procedure consisted of showing a group of 25 human participants the three videos, and asking them to fill in a questionnaire concerning their reactions to them. The questionnaires were based on the validated measurement tool developed by Bartneck *et al.,* (2009) to measure user reactions using a five point Likert scale with the scale extremes being Fake/Natural, Machinelike/Humanlike, Artificial/Lifelike, Unconscious/Conscious and Moving rigidly/Moving elegantly.

The questionnaire used for evaluation is shown in figure 4.45,

Age (optional)			**Gender (optional)**			
Fake	1	2	3	4	5	**Natural**
Machinelike	1	2	3	4	5	**Humanlike**
Artificial	1	2	3	4	5	**Lifelike**
Unconscious	1	2	3	4	5	**Conscious**
Moving rigidly	1	2	3	4	5	**Moving elegantly**

Figure 4.45 The Set of questions used for the evaluation of each video.

The videos were shown to the participants with a view to evaluating how their reactions to the movements of each the robots and the human compared. In order to maintain a 'non

bias', it was necessary to make sure that the robots and human could not be identified by appearance. That is, it was necessary to disguise them in some way. To this end, a mask was developed, that could be worn by both the human and robots alike. This was made of a matt black material, and the eyes and mouth were backlit. Figure 4.46 shows the mask in daylight, and then in darkness, as it was filmed.

Figure 4.46 The mask used for testing the reaction of human participants to human and robot movements.

Fig 4.47 shows a daylight view of the human and the two robots with the masks fitted.

Figure 4.47 Human (Phil) (left), Artie (centre), and Eddie (right) with mask fitted.

This shows that when filmed in darkness, it was impossible for the participants to identify the human and robots by appearance when they watched the videos. The videos were shown to the human participants, without any indication of what/who was producing the movements. The statistical analysis was done by the use of SPSS v. 23.

4.7.1 Overall Results

A Repeated Measures analysis of variance (ANOVA) was used to test the null hypotheses that the mean overall rating for the human and robot head movements were the same (i.e. that H_0: $\mu_A = \mu_B = \mu_C$, where μ_X is the mean overall rating for video X, against the alternative that at least two of the means are different). In all the following cases Mauchley's test assumed sphericity. The results of this test are shown in table 4.2.

Table 4.2 Tests of within-subjects effects.

Tests of Within-Subjects Effects					
Measure: MEASURE_1					
Source	Type III Sum of Squares	df	Mean Square	F	Sig.
Rating	316.667	2	158.333	16.193	.000
Error(Rating)	469.333	48	9.778		

The results in Table 4.2 show that F(2; 48) = 16:193 with the p-value < 0.001 indicating a less than 0.1% probabilityof the means being the same across all videos. The null hypothesis can therefore be rejected and a post-hoc test used to discover where the differences lie in the evaluations of the videos. The post-hoc test was done using pairwise comparisons between the questionnaire results for the 3 videos. The results of the pairwise test are shown in Table 4.3.

Table 4.3 Pairwise comparisons.

Measure: MEASURE_1

(I) Rating	(J) Rating	Mean Difference (I-J)	Std. Error	Sig.[b]
A	C	-3.000*	.733	.001
	B	5.000*	.902	.000
B	C	-3.000*	.733	.001
	A	2.000	.998	.160

*. The mean difference is significant at the .05 level.
b. Adjustment for multiple comparisons: Sidak.

The post hoc tests, using Sidak adjustment, test the null hypotheses that

H_0: $\mu_i = \mu_j$ *for i, j* – 1,2,3. The outcome of this test is:

Reject H_0: $\mu_C = \mu_A$, p-value <.001.

Reject H_0: $\mu_C = \mu_B$, p-value <.001.

Fail to reject H_0: $\mu_A = \mu_B$, at 5% as p-value = 0.16.

The validity of Repeated Measures ANOVA is based on the underlying assumptions of normality for population in each group. The graphical checks and normality tests that were conducted, show that this assumption is valid. Moreover, the equal group sizes guarantee that even moderate departures from the underlying assumptions are not problematic. However, to confirm the results even more emphatically, a non-parametric test (Friedman) was also used, as shown in table table 4.4.

Table 4.4 Friedman test.

N	25
Chi-Square	20.702
Df	2
Asymp. Sig.	.000
Exact Sig.	.000
Point Probability	.000

The test rejects the null hypothesis of equality of medians, and the post hoc test based on Studentized Range Test confirms the results of the parametric test above. Having now established a statistically significant difference between the overall means of the 3 subjects, tests were carried out on the different aspects of the questionnaire.

4.7.2 Different Aspects Results

4.7.2.1 4.7.2.1 Fake v Natural

To test the hypothesis that the mean overall rating for the three were the same, I ran a Repeated Measures ANOVA. That is to test H_0: $\mu_A = \mu_B = \mu_C$ against the alternative that at least two means are different. The partial results of the test are shown in table 4.5.

Table 4.5 Tests of Within-Subjects Effects.

Tests of Within-Subjects Effects					
Measure: MEASURE_1					
Source	Type III Sum of Squares	df	Mean Square	F	Sig.
F_N	37.520	2	18.760	14.727	.000
Error(F_N)	61.147	48	1.274		

F(2,48) = 14.727 and p-value<.001. So, I rejected the null hypothesis. I now needed to find out where the differences lay, using a post hoc test. This is shown in tables 4.6 and 4.7.

Table 4.6 Marginal Means.

Measure: MEASURE_1

F_N	Mean	Std. Error	95% Confidence Interval	
			Lower Bound	Upper Bound
1	4.120	.176	3.756	4.484
2	3.440	.252	2.920	3.960
3	2.400	.238	1.909	2.891

Table 4.7 Pairwise Comparisons.

Pairwise Comparisons

Measure: MEASURE_1

(I) F_N	(J) F_N	Mean Difference (I-J)	Std. Error	Sig.[b]
A	C	.680	.304	.101
	B	1.720*	.297	.000
B	C	-.680	.304	.101
	A	1.040*	.353	.021
C	A	-1.720*	.297	.000
	B	-1.040*	.353	.021

Based on estimated marginal means

*. The mean difference is significant at the .05 level.

b. Adjustment for multiple comparisons: Sidak.

The post hoc tests, using Sidak adjustment, tests the null hypothesis that

H_0: $\mu_i = \mu_j$ for $_{i, j}$ – 1,2,3. The outcome is:

Do not reject H_0: $\mu_C = \mu_A$, p-value - 0.101.

Reject H_0: $\mu_C = \mu_{B \text{ and }} H_0$: $\mu_A = \mu_{B.}$

This shows when rating the fake/natural parameter, the means ratings for the human and Edie were not statistically different, whereas the mean rating for Robothespian video was statistically different from the other two.

The results of the Friedman Test for the Fake vs Natural case are shown in Table 4.8.

Table 4.8 Friedman Test.

Test Statistics

N	25
Chi-Square	16.349
Df	2
Asymp. Sig.	.000
Exact Sig.	.000
Point Probability	.000

The test rejects the null hypothesis of equality of medians and the post hoc test based on Studentized Range Test confirms the same result.

Similar tests were carried out for the remaining 4 questions on the questionnaire, and the results are shown in the following sections.

4.7.2.2 Machinelike v Humanlike

Table 4.9Tests of Within Subjects Effects.

Tests of Within-Subjects Effects					
Measure: MEASURE_1					
Source	Type III Sum of Squares	df	Mean Square	F	Sig.
M_H	4.827	2	2.413	1.252	.295
Error(M_H)	92.507	48	1.927		

Do not reject H_0: $\mu_A = \mu_B = \mu_C$ since the test shows no statistically significant difference between the means of all 3 videos in the machinelike/humanlike aspect.

Table .iraeMara igraM 4.10

Marginal Means

Measure: MEASURE_1

M_H	Mean	Std. Error	95% Confidence Interval	
			Lower Bound	Upper Bound
A	2.360	0.276	1.790	2.930
B	2.520	0.295	1.911	3.129
C	2.960	0.303	2.335	3.585

Table.taMg nra egMF 4.11

Test Statistics[a]

N	25
Chi-Square	5.692
df	2
Asymp. Sig.	.058
Exact Sig.	.058
Point Probability	.004

a. Friedman Test

Do not reject the null hypothesis of equality of medians (marginally). Therefore, regarding the machinelike/humanlike parameter, all three subjects exhibited no significant differences.

4.7.2.3 *Artificial v Lifelike*

Table 4.12 Tests of Within Subjects Effects.

Tests of Within-Subjects Effects					
Measure: MEASURE_1					
Source	Type III Sum of Squares	df	Mean Square	F	Sig.
A_L	15.707	2	7.853	3.661	.033
Error(A_L)	102.960	48	2.145		

Reject H_0: $\mu_A = \mu_B = \mu_C$, thereby rejecting the significant relationship of the 3 videos when comparing the means of the artificial/lifelike aspect.

Table 4.13 Marginal Means.

Estimates

A_L	Mean	Std. Error	95% Confidence Interval	
			Lower Bound	Upper Bound
A	3.160	0.269	2.605	3.715
B	2.560	0.300	1.940	3.180
C	3.680	0.256	3.151	4.209

Table 4.14 Pairwise Comparisons.

Pairwise Comparisons

Measure: MEASURE_1

(I) A_L	(J) A_L	Mean Difference (I-J)	Std. Error	Sig.[a]
A	C	.520	.366	.424
	B	1.120	.437	.050
B	C	-.520	.366	.424
	A	.600	.436	.451
C	A	-1.120	.437	.050
	B	-.600	.436	.451

Based on estimated marginal means

a. Adjustment for multiple comparisons: Sidak.

The p-value of 5% is too marginal to rule out the difference between video B (Robothespian) and video C (human).

Table 4.15 Friedman Test.

Test Statistics[a]

N	25
Chi-Square	4.207
df	2
Asymp. Sig.	.122
Exact Sig.	.123
Point Probability	.005

a. Friedman Test

However, the non-parametric test fails to reject equality of medians. Therefore, overall, it would appear that the means for the artificial/lifelike parameter are significantly similar for video B (Robothespian) and video C (human) and video A (Artie), as well as the medians.

4.7.2.4 Unconscious v Conscious

Table 4.16 Tests of Within Subjects Effects.

Tests of Within-Subjects Effects						
Measure: MEASURE_1						
Source		Type III Sum of Squares	df	Mean Square	F	Sig.
U_C	Sphericity Assumed	2.587	2	1.293	.846	.436
Error(U_C)	Sphericity Assumed	73.413	48	1.529		

Does not reject H_0: $\mu_A = \mu_B = \mu_C$, therefore, there are no significant differences between the means.

Table 4.17 Marginal Means.

Marginal Means

Measure: MEASURE_1

U_C	Mean	Std. Error	95% Confidence Interval	
			Lower Bound	Upper Bound
A	3.160	0.243	2.659	3.661
B	2.720	0.268	2.167	3.273
C	3.040	0.241	2.542	3.538

Table 4.18 Friedman Test.

Test Statistics[a]

N	25
Chi-Square	.494
df	2
Asymp. Sig.	.781

a. Friedman Test

Does not reject the hypothesis of equality of medians. Therefore, in the aspect conscious/unconscious all 3 videos demonstrated no statistically significant differences between their means and medians.

4.7.2.5 Rigidly v Elegantly

Table 4.19 Tests of Within Subjects Effects.

Tests of Within-Subjects Effects

Measure: MEASURE_1

Source	Type III Sum of Squares	df	Mean Square	F	Sig.
R_E	30.907	2	15.453	11.280	.000
Error(R_E)	65.760	48	1.370		

Result; Reject H_0: $\mu_A = \mu_B = \mu_C$. The pairwise comparisons show significant diffences in means for video C (human) and video A (Eddie), and vidoe C and B (Robothespian), but not in the means for video A and video B.

Table 4.20 Marginal Means.

Marginal Means

Measure: MEASURE_1

R_E	Mean	Std. Error	95% Confidence Interval	
			Lower Bound	Upper Bound
A	2.880	0.273	2.317	3.443
B	2.800	0.265	2.254	3.346
C	4.200	0.173	3.843	4.557

Table 4.21 Pairwise Comparisons.

Pairwise Comparisons

(I) R_E	(J) R_E	Mean Difference (I-J)	Std. Error	Sig.[b]
C	A	1.320*	.330	.002
	B	1.400*	.316	.001
A	C	-1.320*	.330	.002
	B	.080	.346	.994
B	C	-1.400*	.316	.001
	A	-.080	.346	.994

*. The mean difference is significant at the .05 level.

b. Adjustment for multiple comparisons: Sidak.

Table 4.22 Friedman Test.

Test Statistics[a]

N	25
Chi-Square	17.062
df	2
Asymp. Sig.	.000
Exact Sig.	.000
Point Probability	.000

a. Friedman Test

Result: Rejects the hypothesis of equality of medians. Overall, this indicates a similarity in means between the 2 robots, which is also confirmed by the post hoc test for equality of medians.

4.8 Summary

This chapter demonstrated the methods used to gather the data during experimentation. The ability of the robot to perform non-rotational lateral movements was demonstrated, thus achieving the major aim of the research. Figures 4.48 and 4.49 shows the capability of the robot to perform these movements, if the required muscle control signals were established.

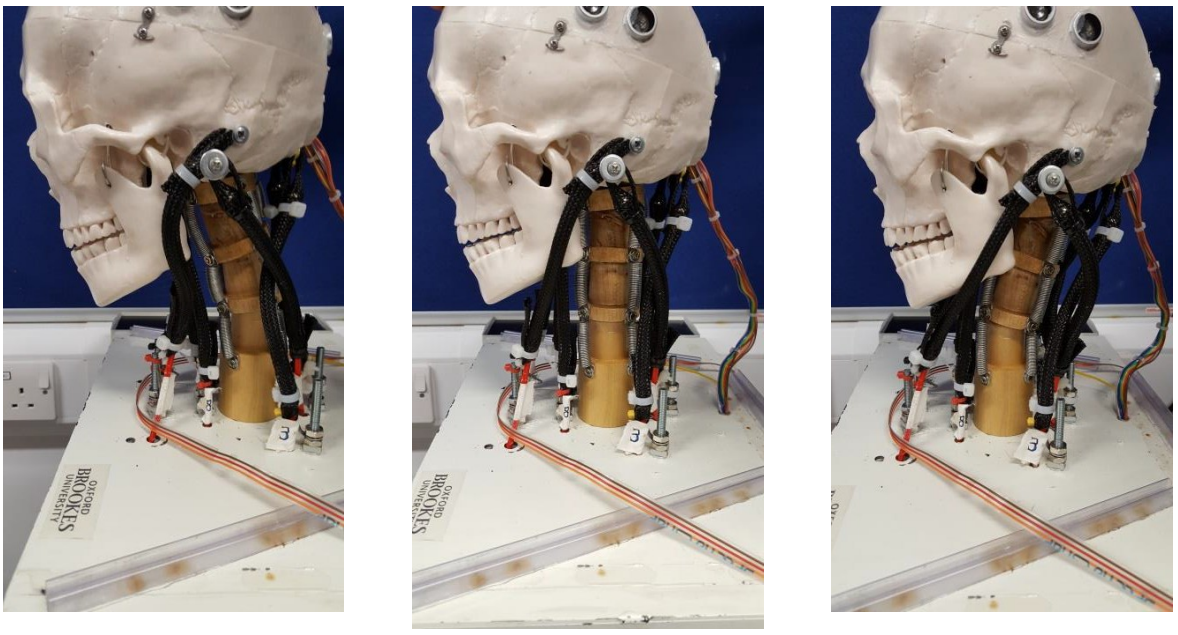

Figure 4.48 Robot's ability to perform front to back non-rotational linear translations.

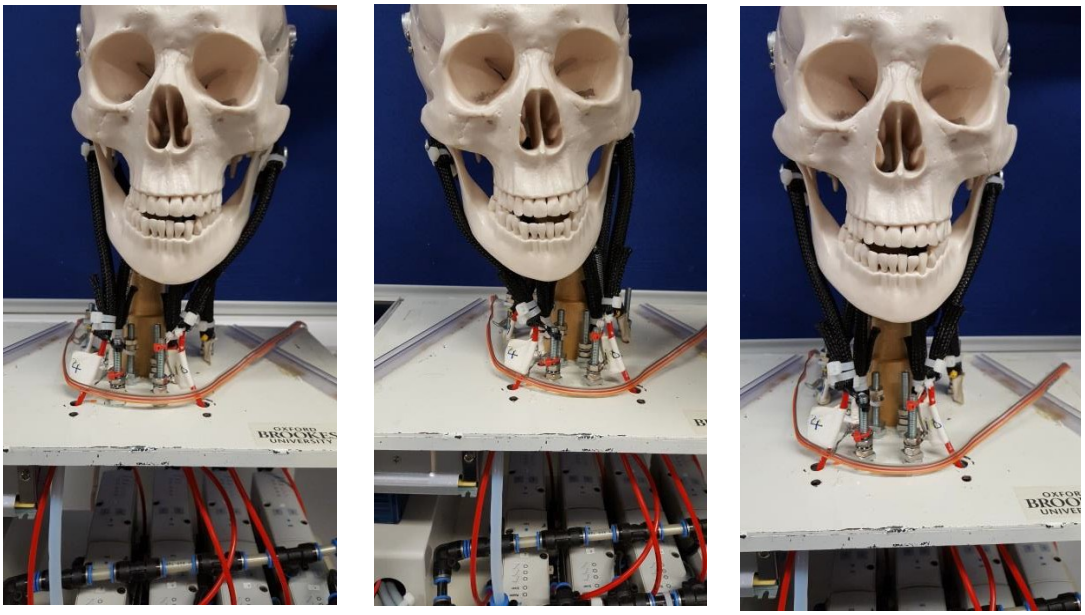

Figure 4.9 Robot's ability to perform side to side non-rotational linear translations

Also included were the results for the Pitch, Roll and Yaw tests, and alongside each experimental result was a discussion and explanation of the phenomena observed.

Table 4.23 summarises the results, and shows the angular ranges and velocities achieved by the robot during the experimental runs for Pitch (nod), Roll (tilt) and Yaw (rotate). As can be seen, given the comparatively low pressure (4bar maximum) at which the air muscles were operated the results look promising.

Table 4.23 Ranges of rotation, angular speed and acceleration for the various degrees of freedom of the robot based on 20 measurements.

	Range		**Angular Velocity**	
	Robot	**Human**	**Robot**	**Human (voluntary)**
Pitch/Nod	40%	107.5°	300°/Sec	100°/Sec
Roll/Tilt	45%	90°	220°/Sec	100°/Sec
Yaw/Rotate	26%	140°	240°/Sec	100°/Sec

The figures show that the angular velocities exceeded those of normal voluntary movement in humans. The angular ranges, whilst expectedly low due to the low air supply pressure to the muscles do show exciting possibilities of movement using air muscles as actuators in humanoid robotic head/necks.

Another contributing factor in the limitation of angular ranges stems from the fact that all the air muscles have the same length with the exception of those representing the Longus Colli muscles (muscles labelled 2 and 6 on the robot). While this configuration favours a straight central neutral position of the humanoid robotic head, the smaller size of the Longus Colli air muscles induces an undesirable flexion, and limits the motion range when the other air muscles operate.

Table 4.24 summarises the accuracy of the accelerometer drift compensated data when compared to the non-drifting ultrasonic data. This shows that the data were associated within the 5% significance level, with just the Z plane rotation during Z plane movement data falling short by 0.3% with a significance level of 94.7%. Overall, a very pleasing result which statistically validates the data presented in this chapter.

Table 4.24 Summary of the statistical significance of the accelerometer drift compensated data in comparison to the non-drifting ultrasonic data.

Action	Movement	Accuracy of drift compensated data
Nod (Y plane)		
	Y plane rotation	95.7%
	X plan rotation	95.3%
	Z plane rotation	97.8%
	Non-rotational lateral translation in Y plane	99.7%
Tilt (X plane)	X plane rotation	95.8%
	Y plan rotation	95.1%
	Z plane rotation	97.1%
	Non-rotational lateral translation in X plane	99.5%
Rotate (Z plane)	Z plane rotation	94.7%
	X plan rotation	**95.4%**
	Z plane rotation	**95.8%**

In addition to the more objective tests of the robot's movements, subjective tests were carried out with human subjects evaluating various aspects of the robot's movements in comparison to another robot and a human being. The tests were blind, in that the participants had no way of knowing if the movements that they were watching were those of a human or a robot. As was seen, although (as expected) the human came top in the scoring, it was found that overall, Eddie scored higher than a robot with a more 'convential' actuation. The results were pleasing in that the robot scored statistically similar means and medians to a human in 3 of the 5 measurements, these being Fake/Natural, Machinelike/Humanlike, and Unconscious/Conscious.

In final summary, the results show some exciting potential for the future development of air muscle actuated, spine-based robotic head and neck systems, and this will be discussed further in the following chapter, conclusion and future work.

CHAPTER 5
CONCLUSIONS AND FUTURE WORK

5.1 Conclusions

5.2 Future work

5.1 Conclusions

This thesis has presented the design, build and evaluation of a humanoid robotic head/neck, the design of which was based upon the structure and function of the human neck musculoskeletal system. The main design idea was to have a flexible structure (cervical spine) actuated by surrounding contractile elements (muscles). In the implementation, the flexible kinematic structure was simplified, in that it was represented by four interconnected wooden vertebrae. The individual vertebrae were linked using four steel springs and an extensible cable which transverses them through a central hole. This coupling contributes to limit the flexion of the cervical spine and provides stability. Its actuation was achieved by eight air muscles whose topology is biologically inspired by the antagonist muscular actuation found in humans.

The proposed design was complemented with a sensory system composed of three ultrasonic sensors; one 3 axis gyroscope, one 3 axis accelerometer, and three ultrasonic sensors. The gyroscope and accelerometer were needed to collect the data required to measure the angular ranges and velocities of the head, whilst the ultrasonic sensors were used to validate this data.

As can be seen from the thesis, the design was iterative in process, in that some initial design decisions did not hold up to scrutiny when realised. However, the time spent on these was not viewed as wasted. Rather, they were viewed as an important exploration and review of design alternatives, which informed and justified the final design decisions. During this design process, much use was made of the literature on current approaches, although great effort was put into the process of coming up with an original approach and design. As stated earlier, the design was also much informed by the structure of its biological counterpart, a human neck. During the physical actuation of the neck the air supply to the robot was restricted to 4bar, in order to minimise failure of the air muscles due to air leaks, whilst being sufficient to produce the desired movements. Despite this self-imposed restriction, the preliminary results are encouraging. They demonstrate that the combination of a flexible cervical spine-like structure with an antagonistic air muscle based actuation system allows the development of robotic musculoskeletal humanoid necks that closely mimic the biomechanical systems of movement of a human head, thus allowing both rotational and linear movements to be performed. This is the major original contribution of this work, as this has not been done before.

During the testing phase, some interesting (if not unexpected) phenomena became very apparent. At the end of each movement, the head exhibited bounce and overshoot. The

bounce was due to the lack of a restraining force from the antagonist in the active muscle pair, and also no deceleration pressure curve as the head approached its limit of movement. As the point of the experiments was to establish maximum angular velocities and ranges, it was undesirable to include such a deceleration curve in the testing. The overshoot was due to the inertia of the head. Again, this could have been reduced by decelerating the head as it approached its limit of movement, and also by reducing the mass of the head. The head, at times, also showed a tendency to skew in some movements. This was due to the non-perfect length matching of the air muscles. These imperfections were due to the difficulties in precise manufacture, which is something that can be addressed in future work. Also apparent at times, was some element of stiction between the wooden vertebrae. Much as the ball and socket arrangements were machined, they were not totally precise in their fit. The balls and sockets were lubricated, but the problem persisted. It is therefore posited that this stiction was very much in part due to the nature of the material itself, that is, in this case, wood.

Rather than restrict the testing to the gathering of data only from the plane of movements under test, data from all three planes, namely, X, Y and Z were gathered to establish the interplay between them. That is, for instance, how an intentional Pitch (nod) movement may also result in coincidental Roll (tilt) and Yaw (rotate) movements. To do this, for each intentional movement, data were gathered for angular velocity and range in all three planes, with the linear translations being measured for two of them. The displacement for the Z was not measured, as this in itself is a rotational plane. As the resultant data showed, as in human neck movements, the movements were interrelated, and the relationship between them was explored, quantified and discussed. Also, during this testing, a gradual positional skew was observed in some coincidental planes of motion. During the analysis of this phenomena, it became apparent that the most likely causes of this were the non-perfection in the matching of the air muscle lengths, and also the stiction between the wooden vertebrae.

After testing the results showed that the angular velocities in voluntary head movements of humans were exceeded by the robot. Indeed, they were close to the absolute maximum (involuntary) angular speeds. The experimentation also demonstrated the robot's ability to perform non-rotational linear translations. The angular ranges show the potential to match the range of motions of a human head, given the limitation of the relatively low air pressure supplying the air muscles. Another limiting factor in the achieved angular ranges is the fact that six of the eight air muscles were set to be the same length, which is not the case in a human neck. This is quite an interesting problem for the future, as the longer they are, the

more distance they contract. Conversely though, they do have to be short enough to fit in the space available, which ideally should mimic the muscle positions within the human body.

Following the objective measurements of the robot's performance, tests were then carried out to establish its emotional acceptability. To do this, 25 people were shown 3 videos comprising; a human, another robot with more conventional actuation (a motor at the axis of rotations), and a human. The robots and the human were fitted with a black mask, with illuminated eyes and mouth, and then filmed in the dark. This ensured that the people watching the video had not way of identifying whether the videos were of a human or robot. Whilst watching the videos the people were asked to fill in a validated questionnaire consisting of 5 measurements on a 5 part Likert scale.

In comparing “machine-like vs humanlike”, “artificial vs lifelike” and “unconscious vs conscious” all the movement in the videos were seen as similar. This indicates that the conventional and the muscular skeletal robot head both give perceived realistic movement for these Libert human likeness scales. When comparing “fake vs natural” there was seen to be similarity between the muscular skeletal movement (A) and human movement (C). Although there is this improvement, with the muscular skeletal robot, the robot movement videos were still seen to be more similar to each other than to the human movement video. Most markedly when it comes to “rigidity vs elegantly”. When examining the mean values for each video it can be seen that participants often struggled to judge realistic movement (Tables 4.10, 4.13, 4.17), with values falling close to the mid-scale value of 3. Apart from “unconscious vs conscious”, Table 4.17, the human movement video was always perceived to be more realistic (higher mean values). For “fake vs natural” and “rigidity vs elegantly” participants were much more able to identify the human movement video as being realistic (Tables 4.6, 4.10). Although improvement has been seen with the muscular skeletal robot; work is still required to give convincing human movement, particularly when comparing “Rigidity vs Elegantly”.

In conclusion, when referring to the aims at the beginning of the thesis, it can be seen that these aims have been met, in particular, the production of a humanoid robotic head capable of non-rotational lateral movements and of approximating the angles and velocities of human head movements where the actuation and neck closely resemble that of their biological counterparts, which is an original contribution to the field of robotics.

The robot was featured on BBC World News on November 17th 2014. To view this, please go to:

https://www.youtube.com/watch?v=ze42n6xiRkk

5.2 Future work

After analysis, the data showed that whilst it was moving in a particular plane, inevitably there was some simultaneous movement in the other two planes. Much as this was expected and acceptable, there was an unexpected gradual skewing evident in some planes. This was due to the unequal lengths of some of the muscle pairs, which was due to the difficulties of manufacture. In the future, this issue requires much more experimentation. This should minimise the problem of skew, and also the issue of non-symmetrical bounce at the limits of movement. Further work could also be carried out to match the lengths of the air muscles to their biological counterparts, because, as it was stated earlier, the manufacture of four of the 6 air muscles to the same length somewhat restricted the angular ranges of movement. The bounce at each end of the movements was due to the inertia of the head, and to the way it was fully energised throughout its movement. That is, moving at its maximum speed. To compound this, the antagonist muscles were fully de-energised, thus allowing the head to move unabated. In future work, the head movements should include the operation of the antagonist muscles to effectively brake the movement where necessary. Also, the agonist muscle could be deflated as it approaches its target position. This would slow the movements somewhat, but as was seen, the angular velocities well exceeded voluntary human ones, so this reduction would not pose a problem.

Another opportunity for future work is the optimisation of the vertebrae design. Whilst in this thesis the design and mechanism of the neck is presented, as mentioned earlier, there were problems of stiction between the vertebrae, and bounce due to the inertia of the head, which in turn was due to the mass of the head. A refinement of the vertebrae design and the reduction in the mass of the head could reduce these problems.

A major challenge for the future is the coordination of the air muscles, particularly if the non-rotational linear head gestures are to be replicated at will. In this work, the operation

of the air muscles has been digital, that is, they were either fully inflated or fully deflated, with the associated antagonist doing the opposite. In order for the robot to achieve any realistic human head gestures, it is necessary to coordinate eight of the muscles to work together, utilising all 256 pressure levels that are available when using an 8-bit control system. This ability to perform realistic head gestures would have improved the acceptability and emontional acceptance of the robot. This, although seemingly a comparatively simple at first glance, is indeed a mammoth task, as to do so would mean a possible 256^8 combinations to work with. This gives a figure of approximately 1.84e+19 combinations. If these were explored at a rate of one combination per second, it would

take over 500 Billion years to complete all the possibilities. For this reason, a more sophisticated control architecture and the application of autonomous learning methods could be used towards this aim. One such exploratory approach is Goal Babbling, which has already successfully been applied in the control of a pneumatically actuated elephant trunk (Rolf and Steil, 2014). It involves a trial and error process which enables the controller to discover the set of air muscle pressures to accomplish a specific movement. The pressure feedback system already built into the robot could be used for this. The aim would be to employ the respective inverse mappings to control real-time head movements that simulate natural and versatile communicative head gestures, that would in turn should improve the acceptability and believability of the robot.

REFERENCES

Reference list in Alphabetical order

Reference list in alphabetical order

(A)

Arcoverde Neto, E.N., Duarte, R.M., Barreto, R.M., Magalhães, J.P., Bastos, C.C.M, Ren, T.I. and Cavalcanti, G.D.C. (2014). 'Enhanced real-time head pose estimation system for mobile device'. Integrated Computer-Aided Engineering, 21(3), pp.281-293.

Arduino, (2015) (a). PWM Tutorial. [online] Available at: https://www.arduino.cc/en/Tutorial/PWM [Accessed 30 June 2016].

Arduino, (2015) (b). Arduino/Genuino Uno datasheet. [online] Available at: https://www.arduino.cc/en/Main/ArduinoBoardUno [Accessed 5 July 2016].

Atmel Corporation, (2015). Atmel ATmega640/V-1280/V-1281/V-2560/V-2561/V datasheet. [online] Atmel Corporation. Available at: http://www.atmel.com/Images/Atmel-2549-8-bit-AVR-Microcontroller-ATmega640-1280-1281-2560-2561_datasheet.pdf [Accessed 29 July 2015].

(B)

Bartneck, C., Croft, E. and Kulic, D. (2009). 'Measurement instruments for the anthropomorphism, animacy, likeability, perceived intelligence, and perceived safety of robots'. *International Journal of Social Robotics*, 1(1), 71-81.

Bates, J. (1994). 'The role of emotion in believable agents'. Communications of the ACM, 37(7), 122-125.

Baxter, P., Kennedy, J., Senft, E., Lemaignan, S. and Belpaeme, T. (2016). 'From characterising three years of HRI to methodology and reporting recommendations'. Human-Robot Interaction (HRI), 2016 11th ACM/IEEE International Conference on, pp. 391-398.

Beira, R., Lopes, M., Praça, M., Santos-Victor, J., Bernardino, A., Metta, G., Becchi, F. and Saltarén, R. (2006). 'Design of the robot-cub (icub) head'. Robotics and Automation, 2006. ICRA 2006. Proceedings 2006 IEEE International Conference on, pp. 94-100.

Bischoff, R. and Graefe, V. (2002). 'Dependable multimodal communication and interaction with robotic assistants'. In Robot and Human Interactive Communication, 2002. Proceedings. 11th IEEE International Workshop on, pp. 300-305.

Breazeal, C. (2003). 'Emotion and sociable humanoid robots'. International Journal of Human-Computer Studies, 59(1), pp.119-155.

Breazeal, C.L. (2004). 'Designing sociable robots'. Massachusetts: MIT press.

Brooks, R.A., Breazeal, C., Marjanović, M., Scassellati, B. and Williamson, M.M. (1999). 'The Cog project: Building a humanoid robot'. In Computation for metaphors, analogy, and agents, pp. 52-87.

Bogduk, N. and Mercer, S. (2000). 'Biomechanics of the cervical spine. I: Normal kinematics'. Clinical biomechanics,15(9), pp.633-648.

(C)

Cavallo, A., Cirillo, A., Cirillo, P., De Maria, G., Falco, P., Natale, C. and Pirozzi, S. (2014). 'Experimental comparison of sensor fusion algorithms for attitude estimation'. IFAC Proceedings Volumes, 47(3), pp.7585-7591.

Chou, C.P. and Hannaford, B. (1996). 'Measurement and modeling of McKibben pneumatic artificial muscles'. IEEE Transactions on robotics and automation, 12(1), pp.90-102.

Cocaud, C. and Jnifene, A. (2003). 'Analysis of a two DOF anthropomorphic arm driven by artificial muscles'. In Haptic, Audio and Visual Environments and Their Applications, 2003. HAVE 2003. Proceedings. The 2nd IEEE Internatioal Workshop on, pp. 37-42.

Colbrunn, R.W., Nelson, G.M. and Quinn, R.D. (2001). 'Modeling of braided pneumatic actuators for robotic control'. In Intelligent Robots and Systems, 2001. Proceedings. 2001 IEEE/RSJ International Conference on, Vol: 4, pp. 1964-1970.

(D)

Daerden, F. and Lefeber, D. (2002). 'Pneumatic artificial muscles: actuators for robotics and automation'. European journal of mechanical and environmental engineering, 47(1), pp.11-21.

Dautenhahn, K. (2002). 'Design spaces and niche spaces of believable social robots'. Robot and Human Interactive Communication, 2002. Proceedings. 11th IEEE International Workshop on, pp. 192-197.

Davis, S.T. and Caldwell, D.G. (2001). 'The bio-mimetic design of a robot primate using pneumatic muscle actuators'. In CLAWAR 2001: Proceedings of the 4th International Conference on Climbing and Walking Robots, pp. 197-204.

Davis, S., Tsagarakis, N., Canderle, J. and Caldwell, D.G. (2003). 'Enhanced modelling and performance in braided pneumatic muscle actuators'. The International Journal of Robotics Research, 22(3-4), pp.213-227.

Deniz, O., Castrillon, M., Lorenzo, J., Guerra, C., Hernandez, D. and Hernandez, M. (2002). 'Casimiro: A robot head for human-computer interaction'. In Robot and Human Interactive Communication, 2002. Proceedings. 11th IEEE International Workshop on pp. 319-324.

Dillon, A. (2001). 'User acceptance of information technology'. In W. Karwowski (ed). Encyclopedia of Human Factors and Ergonomics. London: Taylor and Francis.

Dutia, M.B. (1991). 'The muscles and joints of the neck: their specialisation and role in head movement'. Progress in neurobiology, 37(2), pp.165-178.

(E)

Equilibar, (2015). 'How Electronic Pressure Regulators Work'. [online] Available at: http://www.equilibar.com/electronic-pressure-regulators/how-eprs-work/ [Accessed 25 July 2015].

Engineered Arts, (2017). Robothespian. Available at www.engineeredarts.co.uk/robothespian/ [Accessed 15th January 2017].

(F)

FESTO, (2015). Proportional Valves. [online] Available at: http://www.festo.com/wiki/en/Proportional_valves#Proportional_directional_control_valves [Accessed 25 July 2015].

Field, A. (2015). 'Discovering Statistics Using IBM SSPS Statistics'. 4th ed. London: Sage.

Fitzpatrick, R. (2010). 'Designing and constructing an animatronic head capable of human motion programmed using face-tracking software'. Graduate project for Degree of Master of Science. Worcester Polytechnic Institute.

(G)

GitHub, (2016). Madgwick Library. [online] GitHub, Inc. Available at: https://github.com/arduino-libraries/MadgwickAHRS [Accessed 21 July 2016].

(H)

Hannaford, B. and Winters, J.M. (1990). 'Multiple Muscle Systems'. New York: Springer, pp. 101–120.

Hayes-Roth, B. (1995). 'Agents on stage: Advancing the state of the art of AI'. IJCAI'95 Proceedings of the 14th international joint conference on Artificial intelligence, Vol: 1, pp. 967–971.

Hill, S. and Hallbert, B. (2000). 'Human Interface Concepts for Autonomous/Distributed Control'. In DARPA ITO Sponsored Research 2000, Idaho National Engineering and Environmental Laboratory.

Hitchin, N. (2000). 'The geometry of three-forms in six dimensions'. Journal of Differential Geometry, 55(3), pp.547-576.

World.Honda, ASIMO. [online] available at: http://world.honda.com/ASIMO/ [Accessed 16 May 2015].

(I)

Valverde Ibáñez, R., Keysermann, M.U. and Vargas, P.A. (2014). 'Emotional memories in autonomous robots'. Robot and Human Interactive Communication, 2014 RO-MAN: The 23rd IEEE International Symposium on, pp. 405-410.

InvenSens, (2016). 'MPU-6500 Six-Axis (Gyro + Accelerometer) MEMS MotionTracking™ Devices'. [online] Available at: https://www.invensense.com/products/motion-tracking/6-axis/mpu-6500/ [Accessed 20 July 2016].

Ishiguro, H. (2006). 'Interactive humanoids and androids as ideal interfaces for humans'. Proceeding IUI '06 Proceedings of the 11th international conference on Intelligent user interfaces, pp. 2-9.

(J)

Jamone, L., Fumagalli, M., Metta, G., Natale, L., Nori, F. and Sandini, G. (2010). 'Machine-learning based control of a human-like tendon-driven neck' Robotics and Automation (ICRA), 2010 IEEE International Conference on, pp. 859-865.

(K)

Kenhub, (2014). 'Directional terms and body planes'. [online] Available at: https://www.kenhub.com/en/videos/terms-of-direction-and-planes-and-axes-of-the-body [Accessed 16 July 2016].

Keywordteam.net. [online] Available at: http://keywordteam.net/gallery/523237.html [Accessed 19th February 2017].

Kozima, H., Nakagawa, C. and Yano, H. (2005). 'Using robots for the study of human social development'. In AAAI Spring Symposium on Developmental Robotics, pp. 111-114.

Kuno, Y., Sadazuka, K., Kawashima, M., Tsuruta, S., Yamazaki, K. and Yamazaki, A. (2007). 'Effective head gestures for museum guide robots in interaction with humans'. In RO-MAN 2007-The 16th IEEE International Symposium on Robot and Human Interactive Communication, pp. 151-156.

(L)

Leigh, R.J. and Zee, D.S. (2015). 'The neurology of eye movements'. Oxford University Press, Vol: 90.

Lester, J.C. and Stone, B.A. (1997). 'Increasing believability in animated pedagogical agents'. Proceeding AGENTS '97 Proceedings of the first international conference on Autonomous agents, pp.16-21.

Liebenson, C. (1996). 'The C2/C3 Joint and Neck Pain'. Dynamic Chiropractic, 14(04).

LoPresti, E., Brienza, D.M., Angelo, J., Gilbertson, L. and Sakai, J. (2000). 'Neck range of motion and use of computer head controls'. Proceedings of the fourth international ACM conference on Assistive technologies, pp. 121-128.

P. Liu, D. F. Glas, T. Kanda and H. Ishiguro. (2016). 'Data-Driven HRI: Learning Social Behaviors by Example From Human–Human Interaction'. IEEE Transactions on Robotics, 32(4), pp. 988-1008.

Lütkebohle, I., Hegel, F., Schulz, S., Hackel, M., Wrede, B., Wachsmuth, S. and Sagerer, G. (2010). 'The Bielefeld anthropomorphic robot head "Flobi"'. Robotics and Automation (ICRA), 2010 IEEE International Conference on, 3(7), pp. 3384-3391.

(M)

Machine design, Sensor Sense: Pulse ranging technology, [online] Available at: http://machinedesign.com/sensors/sensor-sense-pulse-ranging-technology [Accessed 11th February 2017].

Maddock, S., Edge, J. and Sanchez, M. (2005). ‘Movement realism in computer facial animation’, Workshop on Human-animated Characters Interaction (part of HCI 2005: The Bigger Picture The 19th British HCI Group Annual Conference).

Madgwick, S. (2010). ‘An efficient orientation filter for inertial and inertial/magnetic sensor arrays’. Report x-io and University of Bristol (UK).

Marques, H.G., Jäntsch, M., Wittmeier, S., Holland, O., Alessandro, C., Diamond, A., Lungarella, M. and Knight, R. (2010). ‘ECCE1: the first of a series of anthropomimetic musculoskeletal upper torsos’. In 2010 10th IEEE-RAS International Conference on Humanoid Robots, pp. 391-396.

Mataric, M.J. (2000). ‘Getting humanoids to move and imitate’. IEEE Intelligent Systems, 15(4), pp.18-24.

Medendorp, W.P., Melis, B.J.M., Gielen, C.C.A.M. and Van Gisbergen, J.A.M. (1998). ‘Off-centric rotation axes in natural head movements: implications for vestibular reafference and kinematic redundancy’. Journal of neurophysiology, 79(4), pp. 2025-2039.

Metta, G., Natale, L., Nori, F. and Sandini, G. (2011). ‘The icub project: An open source platform for research in embodied cognition’. In Advanced Robotics and its Social Impacts (ARSO), 2011 IEEE Workshop on, pp. 24-26.

Micropik. Sensors. [online] Available at: http://micropik.com/pag_sensores.htm#REFLEXION [Accessed 18th February 201].

Miwa, H., Okuchi, T., Takanobu, H. and Takanishi, A. (2002). ‘Development of a new human-like head robot WE-4’. In Intelligent Robots and Systems, 2002. IEEE/RSJ International Conference on, 3, pp. 2443-2448.

Mori, M., MacDorman, K.F. and Kageki, N. (2012). ‘The uncanny valley [from the field]’. IEEE Robotics & Automation Magazine, 19(2), pp.98-100.

Morin, A. H. (1953). 'Elastic diaphragm'. US Patent No. 2,642,091.

Murphy, R. R., Nomura, T., Billard A. and Burke J. L., (2010) ‘Human–Robot Interaction’, in IEEE Robotics & Automation Magazine, 17(2), pp. 85-89.

(N)

Netter, F.H. (2010). 'Atlas of human anatomy'. Amsterdam: Elsevier Health Sciences.

Nori, F., Jamone, L., Sandini, G. and Metta, G. (2007). 'Accurate control of a human-like tendon-driven neck'. In Humanoid Robots, 2007 7th IEEE-RAS International Conference on, pp. 371-378.

(O)

Openshaw, S. and Taylor, E. (2006). 'Ergonomics and Design A reference guide'. All Steel Inc., Iowa.

ÖLÇÜCÜOĞLU, O. (2007). 'HUMAN-LIKE ROBOT HEAD DESIGN'. Thesis submitted for Degree of Master of Science in Mechanical Engineering. Middle East Technical University.

(P)

Picard, R. W. and Daily, S. B. (2005). 'Evaluating Affective Interactions: Alternatives to Asking What Users Feel'. In CHI Workshop on Evaluating Affective Interfaces: Innovative Approaches. Portland, OR.

Pollack, M.E., Brown, L., Colbry, D., Orosz, C., Peintner, B., Ramakrishnan, S., Engberg, S., Matthews, J.T., Dunbar-Jacob, J., McCarthy, C.E. and Thrun, S. (2002). 'Pearl: A mobile robotic assistant for the elderly'. In AAAI workshop on automation as eldercare, pp. 85-91.

(Q)

(R)

Rodriguez G, J.E. and Valenzuela, M.A. (2011). 'Methodology for the Sizing of Air Muscles in a Robotic Arm'. In Control and Automation (ICCA), 2011 IEEE International Conference on, pp. 19-21.

Rolf, M. and Steil, J.J. (2014). 'Efficient exploratory learning of inverse kinematics on a bionic elephant trunk'. IEEE Transactions on Neural Networks and Learning Systems, 25(6), pp. 1147-1160.

Rose, R., Scheutz, M. and Schermerhorn, P. (2010). 'Towards a conceptual and methodological framework for determining robot believability'. Interact. Stud. Vol: 11, pp. 314–335.

(S)

SHARP, (2006). 'Distance Measuring Sensor Unit Measuring distance' [online] Available at: sharpsma.com/webfm_send/1489 [Accessed 18th February 2017].

Shibata, T., Wada, K., and Tanie, K. (2002). 'Tabulation and analysis of questionnaire results of subjective evaluation of seal robot at Science Museum in London'. In Proc. 11th IEEE International Workshop on Robot and Human Interactive Communication (RO-MAN 2002), pp. 23–28.

Shibata, T., Wada, K., and Tanie, K. (2003). 'Subjective evaluation of a seal robot at the national museum of science and technology in Stockholm'. In Proc. Int. Workshop on Robot and Human Interactive Communication (RO–MAN), pp. 397–407.

Shibata, T., Wada, K. and Tanie, K. (2004). 'Subjective evaluation of a seal robot in Brunei'. In Proc. Int. Workshop on Robot and Human Interactive Communication (RO–MAN), pp. 135–140.

Stewart, D. (1965). 'A Platform with Six Degrees of Freedom'. Proc. Institution of Mechanical Engineers (UK), 1(15).

Stiefelhagen, R., Fugen, C., Gieselmann, R., Holzapfel, H., Nickel K. and Waibel A. (2004). 'Natural human-robot interaction using speech, head pose and gestures'. Proceedings of 2004 IEEERSJ International Conference on, Vol: 3, pp. 2422-2427.

(T)

Texas Instruments, (2015). TL07xx Low-Noise JFET-Input Operational Amplifiers. [online] Available at: http://www.ti.com/product/TL074/datasheet [Accessed 16 July 2016].

Tilley, A. (2002). 'The measure of man and woman: human factors in design'. New Jersey: Wiley.

Tondu, B (2007). 'Artificial Muscles for Humanoid Robots'. Humanoid Robots, Human-like Machines, Matthias Hackel (Ed.), InTech, [online]. Available at: http://www.intechopen.com/books/humanoid_robots_human_like_machines/artificial_muscles_for_humanoid_robots [Accessed 7th August 2016].

Tondu, B., Boitier, V. and Lopez, P. (1994). 'Naturally compliant robot-arms actuated by McKibben artificial muscles'. In Systems, Man, and Cybernetics, 1994. Humans, Information and Technology., 1994 IEEE International Conference on, Vol: 3, pp. 2635-2640.

Tondu, B. and Lopez, P. (2000). 'Modeling and control of McKibben artificial muscle robot actuators'. IEEE control systems, 20(2), pp.15-38.

(U)

Ullman, D. and Malle, B. (2016). 'The effect of perceived involvement on trust in human-robot interaction'. Human-Robot Interaction (HRI), 2016 11th ACM/IEEE International Conference on, pp. 641-642.

(V)

Van Breemen, A., Yan, X. and Meerbeek, B. (2005). 'iCat: an animated user-interface robot with personality'. In Proceedings of the fourth international joint conference on Autonomous agents and multiagent systems, pp. 143-144.

Van Ham, R., Sugar, T., Vanderborght, B., Hollander, K. and Lefeber, D. (2009). 'Review of actuators with passive adjustable compliance/controllable stiffness for robotic apllications'. IEEE Robotics and Automation Magazine, 16(3), pp. 81-94.

Vanderborght, B., Verrelst, B., Van Ham, R., Naudet, J., Vermeulen, J., Lefeber, D. and Daerden, F. (2004). 'LUCY, a bipedal walking robot with pneumatic artificial muscles'. In IEEE Conference on Mechatronics and Robotics, pp. 106-114.

Vijayakumar, S., Conradt, J., Shibata, T. and Schaal, S. (2001). 'Overt visual attention for a humanoid robot'. In Intelligent Robots and Systems, 2001. Proceedings. 2001 IEEE/RSJ International Conference on, Vol: 4, pp. 2332-2337.

homepages.inf. 'Maveric Oculo-Motor Experimental Vision Head'. [online] http://homepages.inf.ed.ac.uk/svijayak/projects/maveric/index.html [Accessed 9th December 2016].

XEOMIN. 'Cervical Dystonia Treatment With XEOMIN' [online] http://www.xeomin.com/consumers/cervical-dystonia/xeomin-for-cervical-dystonia/ [Accessed 26th February 2017].

(W)

Wang, Y.W., Cheng, F., Zhou, Y.C. and Xu, J.H. (2012). 'Analysis of double-T filter used for PWM circuit to D/A converter'. In 2012 24th Chinese Control and Decision Conference (CCDC), pp. 2752-2756.

(X)

XEOMIN. 'Cervical Dystonia Treatment With XEOMIN' [online] http://www.xeomin.com/consumers/cervical-dystonia/xeomin-for-cervical-dystonia/ [Accessed 26th February 2017].

(Y)

H. D. Yang, A. Y. Park and S. W. Lee. (2007). ‘Gesture Spotting and Recognition for Human–Robot Interaction’. In IEEE Transactions on Robotics, 23(2), pp. 256-270.

Yamaguchi, G.T., Moran, D.W. and Si, J. (1995). ‘A computationally efficient method for solving the redundant problem in biomechanics’. Journal of Biomechanics, 28(8), pp.999-1005.

(Z)

Zinn, M., Khatib, O., Roth, B. and Salisbury, J.K. (2004). ‘Playing it safe [human-friendly robots]’. IEEE Robotics & Automation Magazine, 11(2), pp.12-21.

APPENDICES

Appendix A1 Invensense MPU6050. Extract from datasheet

Appendix A2 TL074 Operational Amplifier. Extract from datasheet

Appendix A3 Arduino code for pitch movement

Appendix A4 Arduino code for roll movement

Appendix A5 Arduino code for yaw movement

Appendix A6 Arduino code for gyroscope/accelerometer

Appendix A7 Published Papers

7.1 A1 Invensense MPU6050. Extract form datasheet

Features

Gyroscope Features

The triple-axis MEMS gyroscope in the MPU-60X0 includes a wide range of features:

- Digital-output X-, Y-, and Z-Axis angular rate sensors (gyroscopes) with a user-programmable full- scale range of ±250, ±500, ±1000, and ±2000°/sec
- External sync signal connected to the FSYNC pin supports image, video and GPS synchronization
- Integrated 16-bit ADCs enable simultaneous sampling of gyros
- Enhanced bias and sensitivity temperature stability reduces the need for user calibration
- Improved low-frequency noise performance
- Digitally-programmable low-pass filter
- Gyroscope operating current: 3.6mA
- Standby current: 5μA
- Factory calibrated sensitivity scale factor

Accelerometer Features

The triple-axis MEMS accelerometer in MPU-60X0 includes a wide range of features:

- Digital-output triple-axis accelerometer with a programmable full scale range of ±2g, ±4g, ±8g and
- ±16g
- Integrated 16-bit ADCs enable simultaneous sampling of accelerometers while requiring no external multiplexer
- Accelerometer normal operating current: 500μA
- Low power accelerometer mode current: 10μA at 1.25Hz, 20μA at 5Hz, 60μA at 20Hz, 110μA at 40Hz
- Orientation detection and signaling
- Tap detection
- User-programmable interrupts
- Free-fall interrupt
- High-G interrupt
- Zero Motion/Motion interrupt
- User self-test

Additional Features

The MPU-60X0 includes the following additional features:

- 9-Axis MotionFusion by the on-chip Digital Motion Processor (DMP)
- Auxiliary master I2C bus for reading data from external sensors (e.g., magnetometer)
- 3.9mA operating current when all 6 motion sensing axes and the DMP are enabled
- VDD supply voltage range of 2.375V-3.46V
- Flexible VLOGIC reference voltage supports multiple I2C interface voltages (MPU-6050 only)
- Smallest and thinnest QFN package for portable devices: 4x4x0.9mm
- Minimal cross-axis sensitivity between the accelerometer and gyroscope axes
- 1024 byte FIFO buffer reduces power consumption by allowing host processor to read the data in bursts and then go into a low-power mode as the MPU

ADVANCE INFORMATION

collects more data

- Digital-output temperature sensor
- User-programmable digital filters for gyroscope, accelerometer, and temp sensor
- 10,000 g shock tolerant
- 400kHz Fast Mode I2C for communicating with all registers
- 1MHz SPI serial interface for communicating with all registers (MPU-6000 only)
- 20MHz SPI serial interface for reading sensor and interrupt registers (MPU-6000 only)
- MEMS structure hermetically sealed and bonded at wafer level
- RoHS and Green compliant
-

MotionProcessing

- Internal Digital Motion Processing™ (DMP™) engine supports 3D MotionProcessing and gesture recognition algorithms
- The MPU-60X0 collects gyroscope and accelerometer data while synchronizing data sampling at a user defined rate. The total dataset obtained by the MPU-60X0 includes 3-Axis gyroscope data, 3- Axis accelerometer data, and temperature data. The MPU's calculated output to the system processor can also include heading data from a digital 3-axis third party magnetometer.
- The FIFO buffers the complete data set, reducing timing requirements on the system processor by allowing the processor burst read the FIFO data. After burst reading the FIFO data, the system processor can save power by entering a low-power sleep mode while the MPU collects more data.
- Programmable interrupt supports features such as gesture recognition, panning, zooming, scrolling, zero-motion detection, tap detection, and shake detection
- Digitally-programmable low-pass filters
- Low-power pedometer functionality allows the host processor to sleep while the DMP maintains the step count.
-

7.2 A2 TL074 Operational Amplifier. Extract from datasheet

TL07xx Low-Noise JFET-Input Operational Amplifiers

1 Features

- Low Power Consumption
- Wide Common-Mode and Differential Voltage Ranges
- Low Input Bias and Offset Currents
- Output Short-Circuit Protection
- Low Total Harmonic Distortion: 0.003% Typical
- Low Noise
  V_n = 18 nV/$\sqrt{Hz}$ Typ at f = 1 kHz
- High-Input Impedance: JFET Input Stage
- Internal Frequency Compensation
- Latch-Up-Free Operation
- High Slew Rate: 13 V/μs Typical
- Common-Mode Input Voltage Range Includes V_{CC+}

2 Applications

- Motor Integrated Systems: UPS
- Drives and Control Solutions: AC Inverter and VF Drives
- Renewables: Solar Inverters
- Pro Audio Mixers
- DLP Front Projection System
- Oscilloscopes

3 Description

The TL07xx JFET-input operational amplifier family is designed to offer a wider selection than any previously developed operational amplifier family. Each of these JFET-input operational amplifiers incorporates well-matched, high-voltage JFET and bipolar transistors in a monolithic integrated circuit.

The devices feature high slew rates, low-input bias and offset currents, and low offset-voltage temperature coefficient. The low harmonic distortion and low noise make the TL07xseries ideally suited for high-fidelity and audio pre-amplifier applications. Offset adjustment and external compensation options are available within the TL07x family.

Device Information(1)

PART NUMBER	PACKAGE	BODY SIZE (NOM)
TL07xxD	SOIC (14)	8.65 mm × 3.91 mm
	SOIC (8)	4.90 mm x 3.90 mm
TL07xxFK	LCCC (20)	8.89 mm × 8.89 mm
TL07xxJG	PDIP (8)	9.59 mm x 6.67 mm
TL074xJ	CDIP (14)	19.56 mm × 6.92 mm
TL07xxP	PDIP (8)	9.59 mm x 6.35 mm
TL07xxPS	SO (8)	6.20 mm x 5.30 mm
TL074xN	PDIP (14)	19.3 mm × 6.35 mm
TL074xNS	SO (14)	10.30 mm × 5.30 mm
TL07xxPW	TSSOP (8)	4.40 mm x 3.00 mm
TL074xPW	TSSOP (14)	5.00 mm × 4.40 mm

(1) For all available packages, see the orderable addendum at the end of the data sheet.

7.3 A3 Arduino code for pitch movement

```
int  mus1  =  3;
int  mus2  =  4;
int  mus3  =  5;
int  mus4  =  6;
int  mus5  =  7;
int  mus6  =  8;
int  mus7  =  9;
int mus8 = 10;
int c=0;  //  Define holding pressure on remainder of muscles

void setup() {

  // Declare all pins as outputs
pinMode(mus1, OUTPUT);
pinMode(mus2, OUTPUT);
pinMode(mus3, OUTPUT);
pinMode(mus4, OUTPUT);
pinMode(mus5, OUTPUT);
pinMode(mus6, OUTPUT);
pinMode(mus7, OUTPUT);
pinMode(mus8, OUTPUT);

// Set pressure on all muscles to holding pressure defined by variable c
analogueWrite(mus1, c);
analogueWrite(mus2,  c);
analogueWrite(mus3,  c);
analogueWrite(mus4,  c);
analogueWrite(mus5,  c);
analogueWrite(mus6,  c);
analogueWrite(mus7,  c);
analogueWrite(mus8, c);

}
void loop()
{
for (int i=0; i<20; i++)
 {
analogueWrite(mus1, 0);
analogueWrite(mus2, 255);
analogueWrite(mus3, 0);
analogueWrite(mus4, 255);
analogueWrite(mus5, 0);
analogueWrite(mus6, 255);
analogueWrite(mus7, 0);
analogueWrite(mus8, 255);

delay(1000);
analogueWrite(mus1, 255);
analogueWrite(mus2, 0);
analogueWrite(mus3, 255);
analogueWrite(mus4, 0);
analogueWrite(mus5, 255);
analogueWrite(mus6, 0);
analogueWrite(mus7, 255);
analogueWrite(mus8, 0);

delay (1000);
}
analogueWrite(mus1,  c);
analogueWrite(mus2,  c);
analogueWrite(mus3,  c);
analogueWrite(mus4,  c);
analogueWrite(mus5,  c);
analogueWrite(mus6,  c);
analogueWrite(mus7,  c);
analogueWrite(mus8,  c);
delay (5000);
}
```

7.4 A4 Arduino code for roll movement

```
int  mus1  =  3;
int  mus2  =  4;
int  mus3  =  5;
int  mus4  =  6;
int  mus5  =  7;
int  mus6  =  8;
int  mus7  =  9;
int mus8 = 10;
int c=0;  //  Define holding pressure on remainder of muscles

void setup() {
  // Declare all pins as outputs
pinMode(mus1, OUTPUT);
pinMode(mus2, OUTPUT);
pinMode(mus3, OUTPUT);
pinMode(mus4, OUTPUT);
pinMode(mus5, OUTPUT);
pinMode(mus6, OUTPUT);
pinMode(mus7, OUTPUT);
pinMode(mus8, OUTPUT);

// Set pressure on all muscles to holding pressure defined by variable c
analogueWrite(mus1, c);
analogueWrite(mus2,   c);
analogueWrite(mus3,   c);
analogueWrite(mus4,   c);
analogueWrite(mus5,   c);
analogueWrite(mus6,   c);
analogueWrite(mus7,   c);
analogueWrite(mus8, c);
}

void loop()
{
for (int i=0; i<20; i++)
 {
analogueWrite(mus1, 0);
analogueWrite(mus2, 255);
analogueWrite(mus3, 255);
analogueWrite(mus4, c);
analogueWrite(mus5, 0);
analogueWrite(mus6, c);
analogueWrite(mus7, 255);
analogueWrite(mus8, 0);

delay(1000);
analogueWrite(mus1, 255);
analogueWrite(mus2, 0);
analogueWrite(mus3, 0);
analogueWrite(mus4, c);
analogueWrite(mus5, 255);
analogueWrite(mus6, c);
analogueWrite(mus7, 0);
analogueWrite(mus8, 255);

delay (1000);
}
analogueWrite(mus1,  c);
analogueWrite(mus2,  c);
analogueWrite(mus3,  c);
analogueWrite(mus4,  c);
analogueWrite(mus5,  c);
analogueWrite(mus6,  c);
analogueWrite(mus7,  c);
analogueWrite(mus8, c);

delay (5000);
}
```

7.5 A5 Arduino code for yaw movement

```
int  mus1  =  3;
int  mus2  =  4;
int  mus3  =  5;
int  mus4  =  6;
int  mus5  =  7;
int  mus6  =  8;
int  mus7  =  9;
int mus8 = 10;
int c=0;  //  Define holding pressure on remainder of muscles

void setup() {
  // Declare all pins as outputs
pinMode(mus1, OUTPUT);
pinMode(mus2, OUTPUT);
pinMode(mus3, OUTPUT);
pinMode(mus4, OUTPUT);
pinMode(mus5, OUTPUT);
pinMode(mus6, OUTPUT);
pinMode(mus7, OUTPUT);
pinMode(mus8, OUTPUT);

// Set pressure on all muscles to holding pressure defined by variable c
analogueWrite(mus1, c);
analogueWrite(mus2,  c);
analogueWrite(mus3,  c);
analogueWrite(mus4,  c);
analogueWrite(mus5,  c);
analogueWrite(mus6,  c);
analogueWrite(mus7,  c);
analogueWrite(mus8, c);
}

void loop()
{
for (int i=0; i<20; i++)
 {
analogueWrite(mus1, 255);
analogueWrite(mus2, 0);
analogueWrite(mus3, 255);
analogueWrite(mus4, c);
analogueWrite(mus5, 0);
analogueWrite(mus6, c);
analogueWrite(mus7, 0);
analogueWrite(mus8, 255);

delay(1000);
analogueWrite(mus1, 0);
analogueWrite(mus2, 255);
analogueWrite(mus3, 0);
analogueWrite(mus4, c);
analogueWrite(mus5, 255);
analogueWrite(mus6, c);
analogueWrite(mus7, 255);
analogueWrite(mus8, 0);

delay (1000);

}
analogueWrite(mus1,  c);
analogueWrite(mus2,  c);
analogueWrite(mus3,  c);
analogueWrite(mus4,  c);
analogueWrite(mus5,  c);
analogueWrite(mus6,  c);
analogueWrite(mus7,  c);
analogueWrite(mus8, c);

delay (5000);
}
```

7.6 A6 Arduino code for Gyroscope and accelerometer

```
#include "I2Cdev.h"

#include "MPU6050_6Axis_MotionApps20.h"
//#include "MPU6050.h" // not necessary if using MotionApps include file

// Arduino Wire library is required if I2Cdev I2CDEV_ARDUINO_WIRE implementation
// is used in I2Cdev.h
#if I2CDEV_IMPLEMENTATION == I2CDEV_ARDUINO_WIRE
    #include "Wire.h"
#endif

// class default I2C address is 0x68
// specific I2C addresses may be passed as a parameter here
// AD0 low = 0x68 (default for SparkFun breakout and InvenSense evaluation board)
// AD0 high = 0x69
MPU6050 mpu;
//MPU6050 mpu(0x69); // <-- use for AD0 high

/* =========================================================================
   NOTE: In addition to connection 3.3v, GND, SDA, and SCL, this sketch
   depends on the MPU-6050's INT pin being connected to the Arduino's
   external interrupt #0 pin.  On the Arduino Uno and Mega 2560, this is
   digital I/O pin 2.

*/
// uncomment "OUTPUT_READABLE_QUATERNION" if you want to see the actual
// quaternion components in a [w, x, y, z] format (not best for parsing
// on a remote host such as Processing or something though)
//#define OUTPUT_READABLE_QUATERNION

// uncomment "OUTPUT_READABLE_EULER" if you want to see Euler angles
// (in degrees) calculated from the quaternions coming from the FIFO.
// Note that Euler angles suffer from gimbal lock (for more info, see
// http://en.wikipedia.org/wiki/Gimbal_lock)
//#define OUTPUT_READABLE_EULER

// uncomment "OUTPUT_READABLE_YAWPITCHROLL" if you want to see the yaw/
// pitch/roll angles (in degrees) calculated from the quaternions coming
// from the FIFO.  Note this also requires gravity vector calculations.
// Also note that yaw/pitch/roll angles suffer from gimbal lock (for
// more info, see: http://en.wikipedia.org/wiki/Gimbal_lock)
#define OUTPUT_READABLE_YAWPITCHROLL

// uncomment "OUTPUT_READABLE_REALACCEL" if you want to see acceleration
// components with gravity removed.  This acceleration reference frame is
// not compensated for orientation, so +X is always +X according to the
// sensor, just without the effects of gravity.  If you want acceleration
// compensated for orientation, us OUTPUT_READABLE_WORLDACCEL instead.
//#define OUTPUT_READABLE_REALACCEL

// uncomment "OUTPUT_READABLE_WORLDACCEL" if you want to see acceleration
// components with gravity removed and adjusted for the world frame of
// reference (yaw is relative to initial orientation, since no magnetometer
// is present in this case).  Could be quite handy in some cases.

//#define OUTPUT_READABLE_WORLDACCEL

// uncomment "OUTPUT_TEAPOT" if you want output that matches the
// format used for the InvenSense teapot demo
//#define OUTPUT_TEAPOT



#define LED_PIN 13 // (Arduino is 13, Teensy is 11, Teensy++ is 6)
bool blinkState = false;

// MPU control/status vars
bool dmpReady = false;  // set true if DMP init was successful
uint8_t mpuIntStatus;   // holds actual interrupt status byte from MPU
uint8_t devStatus;      // return status after each device operation (0 = success, !0 = error)
uint16_t packetSize;    // expected DMP packet size (default is 42 bytes)
uint16_t fifoCount;     // count of all bytes currently in FIFO
uint8_t fifoBuffer[64]; // FIFO storage buffer

// orientation/motion vars
Quaternion q;           // [w, x, y, z]         quaternion container
VectorInt16 aa;         // [x, y, z]            accel sensor measurements
```

```
    VectorInt16 aaReal;     // [x, y, z]          gravity-free accel sensor measurements
    VectorInt16 aaWorld;    // [x, y, z]            world-frame accel sensor measurements
    VectorFloat gravity;    // [x, y, z]            gravity vector
    float euler[3];         // [psi, theta, phi]    Euler angle container
    float ypr[3];           // [yaw, pitch, roll]   yaw/pitch/roll container and gravity vector

    // packet structure for InvenSense teapot demo
    uint8_t teapotPacket[14] = { '$', 0x02, 0,0, 0,0, 0,0, 0,0, 0x00, 0x00, '\r', '\n' };



    // ================================================================
    // ===               INTERRUPT DETECTION ROUTINE                ===
    // ================================================================

    volatile bool mpuInterrupt = false;     // indicates whether MPU interrupt pin has gone high
    void dmpDataReady() {
        mpuInterrupt = true;
    }



    // ================================================================
    // ===                      INITIAL SETUP                       ===
    // ================================================================

    void setup() {
        // join I2C bus (I2Cdev library doesn't do this automatically)
        #if I2CDEV_IMPLEMENTATION == I2CDEV_ARDUINO_WIRE
            Wire.begin();
            TWBR = 24; // 400kHz I2C clock (200kHz if CPU is 8MHz)
        #elif I2CDEV_IMPLEMENTATION == I2CDEV_BUILTIN_FASTWIRE
            Fastwire::setup(400, true);
        #endif

        // initialize serial communication

        Serial.begin(115200);
        while (!Serial); // wait for Leonardo enumeration, others continue immediately

        // NOTE: 8MHz or slower host processors, like the Teensy @ 3.3v or Ardunio
        // Pro Mini running at 3.3v, cannot handle this baud rate reliably due to
        // the baud timing being too misaligned with processor ticks.  You must use
        // 38400 or slower in these cases, or use some kind of external separate
        // crystal solution for the UART timer.

        // initialize device
        Serial.println(F("Initializing I2C devices..."));
        mpu.initialize();

        // verify connection
        Serial.println(F("Testing device connections..."));
        Serial.println(mpu.testConnection() ? F("MPU6050 connection successful") : F("MPU6050 connection
failed"));

        //wait for ready
        Serial.println(F("\nSend any character to begin DMP programming and demo: "));
        while (Serial.available() && Serial.read()); // empty buffer
        while (!Serial.available());                 // wait for data

        // load and configure the DMP
        Serial.println(F("Initializing DMP..."));
        devStatus = mpu.dmpInitialize();

        // supply your own gyro offsets here, scaled for min sensitivity
        mpu.setXGyroOffset(220);
        mpu.setYGyroOffset(76);
        mpu.setZGyroOffset(-85);
        mpu.setZAccelOffset(1788); // 1688 factory default for my test chip

        // make sure it worked (returns 0 if so)
        if (devStatus == 0) {
            // turn on the DMP, now that it's ready
            Serial.println(F("Enabling DMP..."));
            mpu.setDMPEnabled(true);

            // enable Arduino interrupt detection
            Serial.println(F("Enabling interrupt detection (Arduino external interrupt 0)..."));
            attachInterrupt(0, dmpDataReady, RISING);
```

```
        mpuIntStatus = mpu.getIntStatus();

        // set our DMP Ready flag so the main loop() function knows it's okay to use it
        Serial.println(F("DMP ready! Waiting for first interrupt..."));
        dmpReady = true;

        // get expected DMP packet size for later comparison
        packetSize = mpu.dmpGetFIFOPacketSize();
    } else {
        // ERROR!
        // 1 = initial memory load failed
        // 2 = DMP configuration updates failed
        // (if it's going to break, usually the code will be 1)
        Serial.print(F("DMP Initialization failed (code "));
        Serial.print(devStatus);
        Serial.println(F(")"));
    }

    // configure LED for output
    pinMode(LED_PIN, OUTPUT);
}



// ================================================================
// ===                    MAIN PROGRAM LOOP                     ===
// ================================================================

void loop() {
    // if programming failed, don't try to do anything
    if (!dmpReady) return;

    // wait for MPU interrupt or extra packet(s) available
    while (!mpuInterrupt && fifoCount < packetSize) {
        // other program behavior stuff here
        // .
        // .
        // .
        // if you are really paranoid you can frequently test in between other
        // stuff to see if mpuInterrupt is true, and if so, "break;" from the
        // while() loop to immediately process the MPU data
        // .
        // .
        // .
    }

    // reset interrupt flag and get INT_STATUS byte
    mpuInterrupt = false;
    mpuIntStatus = mpu.getIntStatus();

    // get current FIFO count
    fifoCount = mpu.getFIFOCount();

    // check for overflow (this should never happen unless our code is too inefficient)
    if ((mpuIntStatus & 0x10) || fifoCount == 1024) {
        // reset so we can continue cleanly
        mpu.resetFIFO();
        Serial.println(F("FIFO overflow!"));

    // otherwise, check for DMP data ready interrupt (this should happen frequently)
    } else if (mpuIntStatus & 0x02) {
        // wait for correct available data length, should be a VERY short wait
        while (fifoCount < packetSize) fifoCount = mpu.getFIFOCount();

        // read a packet from FIFO
        mpu.getFIFOBytes(fifoBuffer, packetSize);

        // track FIFO count here in case there is > 1 packet available
        // (this lets us immediately read more without waiting for an interrupt)
        fifoCount -= packetSize;

        #ifdef OUTPUT_READABLE_QUATERNION
            // display quaternion values in easy matrix form: w x y z
            mpu.dmpGetQuaternion(&q, fifoBuffer);
            Serial.print("quat\t");
            Serial.print(q.w);
            Serial.print("\t");
            Serial.print(q.x);
            Serial.print("\t");
```

```
    Serial.print(q.y);
    Serial.print("\t");
    Serial.println(q.z);
#endif

#ifdef OUTPUT_READABLE_EULER
    // display Euler angles in degrees
    mpu.dmpGetQuaternion(&q, fifoBuffer);
    mpu.dmpGetEuler(euler, &q);
    Serial.print("euler\t");
    Serial.print(euler[0] * 180/M_PI);
    Serial.print("\t");
    Serial.print(euler[1] * 180/M_PI);
    Serial.print("\t");
    Serial.println(euler[2] * 180/M_PI);
#endif

#ifdef OUTPUT_READABLE_YAWPITCHROLL
    // display Euler angles in degrees
    mpu.dmpGetQuaternion(&q, fifoBuffer);
    mpu.dmpGetGravity(&gravity, &q);
    mpu.dmpGetYawPitchRoll(ypr, &q, &gravity);
    mpu.dmpGetQuaternion(&q, fifoBuffer);
    mpu.dmpGetAccel(&aa, fifoBuffer);
    mpu.dmpGetGravity(&gravity, &q);
    mpu.dmpGetLinearAccel(&aaReal, &aa, &gravity);
    mpu.dmpGetLinearAccelInWorld(&aaWorld, &aaReal, &q);

    Serial.print(ypr[2] * 180/M_PI);
    Serial.print("\t");
    Serial.print(ypr[1] * 180/M_PI);
    Serial.print("\t");
    Serial.print(ypr[0] * 180/M_PI);
    Serial.print("\t");


    Serial.print(aaWorld.z);
    Serial.print("\t");
    Serial.print(aaWorld.y);
    Serial.print("\t");
    Serial.print(aaWorld.x);
    Serial.print("\t");

    Serial.println();


#endif

#ifdef OUTPUT_READABLE_REALACCEL
    // display real acceleration, adjusted to remove gravity
    mpu.dmpGetQuaternion(&q, fifoBuffer);
    mpu.dmpGetAccel(&aa, fifoBuffer);
    mpu.dmpGetGravity(&gravity, &q);
    mpu.dmpGetLinearAccel(&aaReal, &aa, &gravity);
    Serial.print("areal\t");
    Serial.print(aaReal.x);
    Serial.print("\t");
    Serial.print(aaReal.y);
    Serial.print("\t");
    Serial.println(aaReal.z);
#endif

#ifdef OUTPUT_READABLE_WORLDACCEL
    // display initial world-frame acceleration, adjusted to remove gravity
    // and rotated based on known orientation from quaternion
    mpu.dmpGetQuaternion(&q, fifoBuffer);
    mpu.dmpGetAccel(&aa, fifoBuffer);
    mpu.dmpGetGravity(&gravity, &q);
    mpu.dmpGetLinearAccel(&aaReal, &aa, &gravity);
    mpu.dmpGetLinearAccelInWorld(&aaWorld, &aaReal, &q);
    //Serial.print("aworld\t");
    Serial.print(aaWorld.x);
    Serial.print("\t");
    Serial.print(aaWorld.y);
    Serial.print("\t");
    Serial.println(aaWorld.z);
#endif

#ifdef OUTPUT_TEAPOT
```

```
            // display quaternion values in InvenSense Teapot demo format:
            teapotPacket[2] = fifoBuffer[0];
            teapotPacket[3] = fifoBuffer[1];
            teapotPacket[4] = fifoBuffer[4];
            teapotPacket[5] = fifoBuffer[5];
            teapotPacket[6] = fifoBuffer[8];
            teapotPacket[7] = fifoBuffer[9];
            teapotPacket[8] = fifoBuffer[12];
            teapotPacket[9] = fifoBuffer[13];
            Serial.write(teapotPacket, 14);
            teapotPacket[11]++; // packetCount, loops at 0xFF on purpose
        #endif

//delay (10);
        // blink LED to indicate activity
        blinkState = !blinkState;
        digitalWrite(LED_PIN, blinkState);


    }
}
```

7.7 A7 Published Papers

Barker, S., Fuente, L.A., Hayatleh, K., Fellows, N., Steil, J.J. and Crook, N.T., 2015, December. Design of a biologically inspired humanoid neck. In *2015 IEEE International Conference on Robotics and Biomimetics(ROBIO)*(pp.25-30).IEEE.
https://www.researchgate.net/publication/319529132_Natural_Head_Movement_for_HRI_with_a_Muscular-Skeletal_Head_and_Neck_Robot

Breton, L., Hughes, P., **Barker, S.,** Pilling, M., Fuente, L. and Crook, N.T., The Impact of Leader-Follower Robot Collaboration Strategies on Perceived Safety and Intelligence. In Volume 84 of the series Intelligent Systems, Control and Automation: Science and Engineering pp 145-158
https://www.researchgate.net/publication/280936093_The_Impact_of_Leader-Follower_Robot_Collaboration_Strategies_on_Perceived_Safety_and_Intelligence